Construction of Self-Charging Power System based on Flexible Triboelectric Nanogenerators and Supercapacitor

Hanfang Feng, BEng, MSc

Submitted to the University of Nottingham for

the degree of Doctor of Philosophy

21 Feb 2023

Abstract

With the development of internet of thighs (IoTs), there are growing demands to utilize sustainable, renewable, and environmental-friendly energy as the power supply. IoTs requires numerous sensors which require power supply with flexibility and light weight to achieve products with small size and multifunctionality. Furthermore, constructing self-charging power systems (SCPSs) with energy-harvest component and energy storage component is of great importance to meet the requirements mentioned above. Triboelectric nanogenerator (TENG), which can convert mechanical energy with low frequency such as human motions into electricity, has emerged as a promising technology because of its light weight, low cost, high efficiency, simple design and environmental friendliness. Among various energy storage devices, supercapacitor (SC) as a kind of electrochemical energy storage devices, has attracted much attention due to its excellent power density, easy maintenance, high coulombic efficiency and superb stability. All these advantages make them suitable for SCPS, so that mechanical energy from environment around can be simultaneously harvested and stored for further sustainable power supply. Considering the service life of TENG and SC, frequent recharging or replacement may cause inconvenience and high maintenance cost. To deal with this problem, the effective strategy is to enhance the outputs of the TENG and improve the energy density of SC.

To achieve high outputs of TENG, enormous studies have been carried out mainly form two aspects. The first one focuses on the increase of triboelectric charge density in the friction surface, which includes the optimized materials selection and chemical surface

modification. The other mainly concentrates on enlarging contact area through the construction of micro-nanostructures on the friction surface. To fabricate SC with high energy density, three effective methods are proposed. Firstly, selecting substrate with high conductivity rather than powders to avoid dead volume and facilite the transportation of ions. Secondly, developing electrochemical materials with high conductivity and reactivity. Thirdly, fabricating multimetal materials to regulate the metallic conductivity and surface reactivity. Based on these principles, three parts are carried out in this thesis:

Firstly, the maskless direct image lithography (DIL) method with high resolution and fast molding speed was used to fabricate the polyurethane (PU) layers with surface microcones to increase the contact electrification area. After chemically modified with trichloro (1H,1H,2H,2H-perfluorooctyl) silane (FOTS) vapor, the contact area further increases accompanying with the enlarged electron affinity difference because of the roughened morphology in micro-nanoscale and the introduction of fluorine on the surface. The TENG based on PU and fluorinated polyurethane (F-PU) layer with microcones can achieve a high current of 22 μA. Moreover, because of the customizability of DIL method and the prominent stability and favorable flexibility of friction layers, the TENG can be fabricated into different shapes to harvest mechanical energy from various human motions. Furthermore, the TENG can serve as the electric supply to improve the antibacterial and antifungal properties of cuprous oxide (Cu_2O) nanowire electrode.

Rational design of micro/nanostructure and synergistic effect of binary metal can

significantly boost the electrochemical properties of electroactive materials. Thus, the hydrothermal stirring method was firstly used to fabricate the free-standing tassels-like nickel cobalt phosphate electrodes composed of ultrathin nanosheets. The as-prepared $Ni_2Co(PO_4)_2$ electrode demonstrates a maximum specific capacity of 2518 mC cm^{-2} (1007 C g^{-1}) at 2 mA cm^{-2}, with 76.7% of the capacity retention at 50 mA cm^{-2}. According to the density functional theory (DFT) calculation results, bimetallic $Ni_2Co(PO_4)_2$ exhibits high conductivity and stronger adsorption capacity of OH^- compared with monometallic $Ni_3(PO_4)_2$, which is favorable for the electron transportation and fast redox reactions. Moreover, asymmetrical supercapacitor with $Ni_2Co(PO_4)_2$ as positive electrode and graphene hydrogel as negative electrode delivers a high energy density of 46.25 W h kg^{-1} and a high power density of 2905W kg^{-1}, which can lit LED lights for over 5 minutes. The ASSC device can also be used to provide power supply for sensor and energy-conversion station.

Finally, TENG and ASSC device were integrated together with a rectifier bridge. By continuous walking, the ASSC device can be charged to 0.8 V within a short time, indicating its potential application for self-charging system.

Key words: self-charging system; triboelectric nanogenerator; direct image lithography; nickel cobalt phosphate; hydrothermal stirring; supercapacitor

Acknowledgement

More than three years of my doctoral research career is coming to an end in the daily hustle and bustle. During my aggressive Ph.D. study, I have gained a lot from the ordinary and compact scientific research life every day. In the continuous exploration and research of the ocean of science, I have learned the most advanced knowledge and realized the splendor and hugeness of the science that has been continuously developed in the process of human beings and nature. In addition, I have a better understanding of the importance of serious attitude to science and to life. Looking back on the process of my step-by-step progress in the past several years, every step of my progress is inseparable from the care and help of the people around me. I would like to express my most sincere respect and gratitude to them!

First and for most, I would like to give my sincere gratitude to my respect supervisor, Prof. Guang Zhu, Prof Mengxia Xu, Prof. Xiaoling Liu and Prof. Bo Li for their guidance and inspiration in my experiments and paper writing . Under the guidance of Prof. Guang Zhu, my thinking and methods of solving problems have been greatly improved, and the method and level of analyzing problems have also been greatly improved. At the same time, his serious attitude towards problems has also deeply affected me. Also, I want to thank Prof. Jie Shang for his efforts on my viva and thesis revision.

Secondly, I would also like to thank Huayang Li, who is conscientious, diligent and approachable, which makes us feel cordial and grateful. He teaches me a lot about the fundamental knowledge of triboelectric nanogenerator. He is always patient to help me

about the measurement, the paper writing and revision. When I feel upset or overwhelming, he always comforts me and encourage me to face the difficulty and help me find the way to improve my research. I would like to thank Yiming Yin, he helps me a lot about the 3D printing, from the model design to the usage of printer. I also want to thank Jin Xu, who accompanies me most during the experiment process, he helps me on the culturing of bacterial, measuring of piezoresistive sensors. I also thanks to the accompany of Jinwei Cao and Xin Li. They are so considerate to relieve my anxiety and we really talked a lot about the research plan and applications. And I would like to thank Carey Tao. She helped me establish the firm laboratory safety awareness. I also thank my husband for his meticulous guidance on my thesis. He has given me pertinent advice every time I encounter difficulties, and he is always patient when I have questions. Finally, I would like to extend my appreciation to my parents and my grandma. They provide me selfless support when I feel helpless. Their constant encouragement enables me to face up to difficulties, face failure bravely, and keep improving.

Achievements

Published papers

[1] **Hanfang Feng**, Huayang Li*, Jin Xu, Yiming Yin, Jinwei Cao, Ruoxin Yu, Bingxue Wang, Runwei Li*, Guang Zhu*, Triboelectric nanogenerator based on direct image lithography and surface fluorination for biomechanical energy harvesting and self-powered sterilization, Nano energy, 2022, 98, 107279.

[2] Jin Xu, Huayang Li*, Yiming Yin, Xin Li, Jinwei Cao, **Hanfang Feng**, Wandi Bao, Hao Tan, Fanyuan Xiao, Guang Zhu*, High Sensitivity and Broad Linearity Range Pressure Sensor Based on Hierarchical In-Situ Filling Porous Structure, npj flexible electronics (Online).

[3] Yiming Yin, Huayang Li, Jin Xu, Chen Zhang, Fei Liang, Xin Li, Yang Jiang, Jinwei Cao, **Hanfang Feng**, Jianan Mao, Ling Qin, Yifan Kang, and Guang Zhu*. Facile Fabrication of Flexible Pressure Sensor with Programmable Lattice Structure[J]. ACS Applied Materials & Interfaces, 2021, 13(8), 10388-10396.

[4] Yiming Yin, Yalong Wang, Huayang Li*, Jin Xu, Chen Zhang, Xin Li, Jinwei Cao, **Hanfang Feng**, and Guang Zhu*. A flexible dual parameter sensor with hierarchical porous structure for fully decoupled pressure-temperature sensing[J]. Chemical Engineering Journal, 2022, 430, 133158.

[5] Jinwei Cao, Fei Liang, Huayang Li, Xin Li, Youjun Fan, Chao Hu, Jing Yu, Jin Xu, Yiming Yin, Fali Li, Dan Xu, **Hanfang Feng**, Huali Yang, Yiwei Liu, Xiaodong Chen, Guang Zhu, Run-Wei Li, Ultra-robust stretchable electrode for e-skin: In situ assembly using a nanofiber scaffold and liquid metal to mimic waterto-net interaction. InfoMat,

2022, 4(4), e12302.

Paper under preparation

Hanfang Feng, Huayang Li, Lehcen Wang, Jin Xu, Yiming Yin, Jinwei Cao, Guang Zhu, Mechanical Force-Driven Growth of Tassels-like Nickel Cobalt Phosphate on Nickel Foam for High-performance Supercapacitor.

Contents

Abbreviations

TENG	Triboelectric nanogenerator
LED	Light-emitting diodes
AC	Alternative current
DC	Direct current
SC	Supercapacitor
SCPS	Self-charging power system
PET	Polyethylene terephthalate
PTFE	Polytetrafluoroethylene
PVDF	Polyvinyldinefluoride
PDMS	Polydimethylsiloxane
ICP-OES	Inductively coupled plasma optical emission spectrometer
FOTS	Trichloro- (1H,1H,2H,2H-perfluorooctyl) silane
SAM	Self-assembled monolayer
FEP	Fluorinated ethylene propylene
ITO	Indium tin oxide
PS	Polystyrene
UV	Ultraviolet
EDLC	Electric double-layer capacitors
PC	Pseudocapacitors
CV	Cyclic voltammogram
GCD	Galvanostatic charge/discharge
E	Energy density
C	Specific capacity
ASSC	Asymmetric supercapacitors
CNT	Carbon nanotube
ABS	Acrylonitrile butadiene styrene
PA	Polyamide
PEG	Polyethylene glycol

PP	Polypropylene
PU	Polyurethane
F-PU	Fluorinated polyurethane
SEM	Scanning electron microscopy
FT-IR	Fourier transform infrared spectroscopy
XRD	X-ray diffraction
XPS	X-ray photoelectron spectroscopy
CFU	Colony-forming units
EDS	Energy dispersive spectrometer
NF	Nickel foam
DFT	Density functional theory
GH	Graphene hydrogel
TEM	Transmission electron microscope
SAED	Selected area electron diffraction
TPU	Thermoplastic urethanes

List of Figures

Chapter 1 Introduction

This chapter introduces the importance of study on the high-performance triboelectric nanogenerators and the construction of self-charging power system. Research aims and objectives as well as the structure of the thesis are also listed in this chapter.

1.1 Background

Nothing is of more significant importance than energy for it is the fundament for sustaining human life, prompting the development of technology, creating economic prosperity and combating the rapid climate change worldwide. Along with the great progress in science and technology as well as the exponential growth of global population, the energy and resource structure tend to undergo a dramatic shift to electricity acting as the main power source.[1, 2] Due to the accelerated consumption of traditional sources, including coal and oil, resource shortage progressively become a daunting challenge to sustain the development of technology and maintain the high-quality daily life. In addition, environmental problems, such as global warming, arising from the combustion of traditional sources has caused concerns. Conversely, there are growing demands for developing environmentally benign and renewable energy resources which are also cheap and abundant to alleviate the oncoming energy crisis.

Recently, solar energy, hydro energy, and geothermal energy have attracted much attention due to their abundant resources and ubiquitous existence in our environment.[3-5] Moreover, the development of high-tech also suggested much higher requirements for energy conversion, storage and delivery.[6] During the past few

decades, scores of electronic devices such as mobile communication equipment, smart wearable electronics, and other internet of things devices on the basis of a number of sensors have emerged and applied in every corner of our daily life. These electronic devices usually equip some power elements with small energy density of microwatt or even milliwatt level. However, the power elements such as battery always possess relatively large volume and rigid bulk shape to facilitate the frequent charging process. Therefore, it is of great importance to fabricate an integrated self-powered system comprising of energy harvest component and energy storage component, which can realize the recharge function through absorbing and conversing external fragmental energy. In addition, as the majority of electronic devices usually closely contact with human body, the prior consideration for energy-supply is from various human motions. As the up-and-coming candidate for self-power system, TENG devices based on the coupling effect of contact electrification and electrostatic induction have attract much attention benefiting from their wide-ranging material selection, extensive structures, light weight, low cost, and great energy harvest efficiency at low working frequencies.[7] TENG devices have applied to harvest various clean energy, ranging from nature energy such as wind,[8] droplet,[9] and ocean waves[10] to human motions including trivial movement,[11] heart beats,[12] and acoustic flow.[13] TENG devices can be applied to power some miniaturized electronic devices like LEDs, while the AC generated and somewhat low output are usually inadequate to power some common electronic devices requiring the constant energy supply.[14] Therefore, storing the

energy generated by TENG is important for further use. SC devices are considered as the most promising candidate among various energy storage devices for storing energy generated by TENG devices. SCs possess the advantages of high power density, long life cycle, safe operation and excellent environmental adaptability.[15] Furthermore, the integration of energy harvesting component (TENG) and energy storage component (SC) can produce the SCPS which is portable, stable and adaptable as shown in Fig.1.

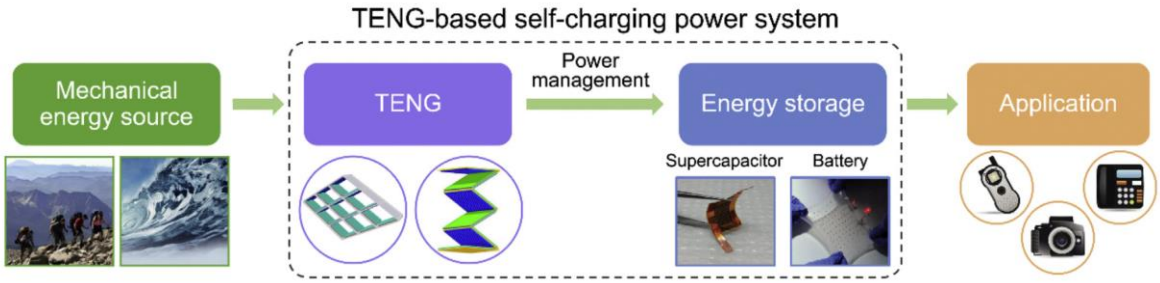

Fig. 1 Diagram of TENG based SCPS.

1.2 Aims and objectives

1.2.1 Aims

The present works mainly focus on the construction of self-powering system composed of energy converting device and energy storage device. Particularly, TENG device is chosen as the energy harvest device due to its various material selection, light weight, low cost, and great energy harvest efficiency at low working frequencies. And TENG device with high-performance and easy fabrication is studied. For energy storage device, supercapacitor is outstanding from various energy storage devices owing to its high power density, safe operation, flexibility, and excellent environmental adaptability. Supercapacitor with high capacity and flexibility is investigated. Finally, self-charging

system based on TENG and SC is studied.

1.2.2 Objectives

The main objective of this thesis includes the following parts.

1. Design and fabricate TENG device with microstructure on surface by direct image lithography method.

2. Optimize the electric outputs of TENG device by regulating chemical treatment process, dimension of device and the height and density of microstructure.

3. Enable the application of high-performance TENG device in harvesting energy from human motions and enhancing sterilization efficiency.

4. Develop supercapacitor electrode with high capacity.

5. Achieve flexible and high performance of asymmetric device.

6. Application of asymmetric supercapacitor device in powering small electronics and constructing self-charging system with TENG device.

1.3 Structure of the thesis

The whole thesis consists of seven chapters as follow:

Chapter one introduces the background, research aims and objectives, and structure of this thesis.

Chapter 2 is the literature review of TENG, including its origin, working mode and methods for boost electric outputs. Self-charging system based on TENG device and supercapacitor device is also introduced.

Chapter 3 focuses on the construction of high-performance TENG device by direct

image lithography method.

Chapter 4 investigates the origin of the enhanced electric outputs of TENG device and its application in energy harvesting from human motions and self-powered sterilization.

Chapter 5 presents the construction of supercapacitor electrode with high capacity and studies the origin of enhanced capacity through theoretical calculation.

Chapter 6 concentrates on the assembling of asymmetric device and its corresponding application in powering small electronics and constructing of self-charging system with TENG device.

Chapter 7 presents the general conclusion, the limitation of recent research and expectations for the future work.

Chapter 2 Literature review

This chapter introduces the basic knowledge and the progress of TENG and SC. The related research of TENG-SC integrated SCPS is also introduced.

2.1 Triboelectric nanogenerator

The first TENG device was invented by ZhongLin Wang and his group in 2012.[16] The device is comprised of PET film and Kapton film as the friction layers and Au electrodes are coated on the back of the layers as shown in Fig. 2.1. The contact-separation design is still applied in current research.

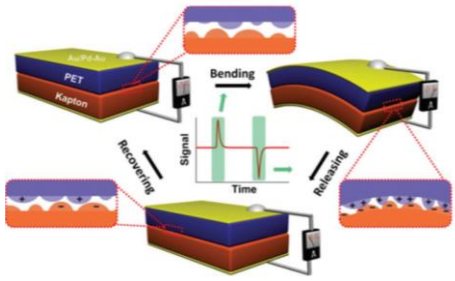

Fig. 2.1 The invention of TENG device and its working mechanism.[16]

The TENG device mentioned above could generate AC output as the contact status between the two friction layers changed, such as cyclic pressing or bending the TENG device. At the beginning of the investigation of TENG, the origin mechanism was explained at a qualitative manner. When the two friction layers are brought into contact with each other under compressing or bending state, triboelectric charges with opposite polarity induce on the surfaces. When the external force is removed, the two friction layers separate, and electric potential difference builds up between the two Au electrodes. The current flows between the two electrodes to screen out the formed

electric field when the TENG connected with external load. As the two friction layers contact again under external stimuli, the current flows back due to the change of the potential difference. Thus, continuous AC outputs generated accompanying with periodic external mechanical motions. Overall, the TENG devices works on the coupling effect of electrification and electrostatic induction. The former one produces the polarized charges on the surfaces and the latter one drives the conversion of mechanical movements to electrical signal. This qualitative explanation delivers a straightforward insight of TENGs based on contact separation mode.

2.1.1 Mechanism origin of TENG

The fundamental physics model was established in 2017, which can be traced back to Maxwell's displacement current as described follows:[17, 18]

$$J_D = \frac{\partial D}{\partial t} = \varepsilon \frac{\partial E}{\partial t} + \frac{\partial P_S}{\partial t} \qquad (2.1)$$

Where J represents the displacement current, D means the displacement field, ε is the permittivity of the medium, E represents the electric field, and P_S is the polarization arising from the surface charges due to the triboelectric effect. The former term describes a time-varying electric field which is the basis of electromagnetic waves, while the latter term represents the contribution of surface polarization which is related to the origin of nanogenerators. More specifically, in triboelectric nanogenerators, the surface polarization attributed to the electrostatic charges induced from triboelectrification. The surface polarization is time-varying when the two friction layers contact-separation periodically under mechanically agitated displacement.

The fundamental model for the TENG device based on contact-separation-mode is demonstrated as in Fig. 2.2a. It consists of two friction layers for contact electrification and two back electrodes connected with external load. Surface charges with opposite polarity generate attributed to the contact electrification. The charge density marks as $\pm\sigma_{tribo}$, which is individual with the gap distance z. It is saturated after the fully contact. When the two layers separate, free electrons flow through external load and transfer to the two electrodes driven by the electrostatic field build on the triboelectric charges. The number of transferred charges marked as $\pm\sigma_{tr}$, is a function of z. Thus, the mechanical movements induce the change of z and can convert into the electrical signal. The displacement current can be estimated as,

$$J_D = \frac{\partial D_z}{\partial t} = \frac{\partial \sigma_{tr}(z,t)}{\partial t} \qquad (2.2)$$

The displacement current is based on the capacitive conduction and the corresponding output current of TENG through electromagnetic waves and induction, rather than the current in resistor arising from the flow of free charges across the electrodes.

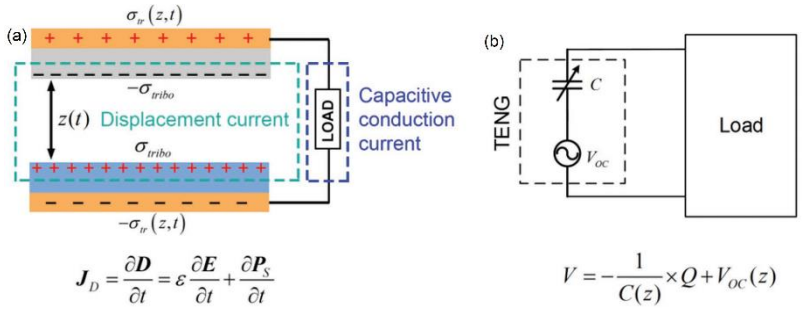

Fig. 2.2 Mechanism origin of TENG. (a) The displacement current model of TENG device based on contact-separation mode ; (b) The equivalent electrical circuit model of TENG.[7]

Meanwhile, charged surfaces with opposite polarity with a time-varying distance can be regarded as a capacitor with time-changing capacitance. This perception offers an

intuitive portrayal of the TENG with the capacitor model as shown in Fig. 2.2b. The current is calculated as,

$$I = \frac{dQ}{\mathrm{d}t} = A\frac{d\sigma_{tr}}{dt} \qquad (2.3)$$

The result is equivalent to Eq. 2.2 and confirms the foundation of the capacitive model is also based on the Maxwell's displacement current. The corresponding voltage output of TENG can be described as:

$$V = -\frac{1}{C(z)} \times Q + V_{oc}(z) \qquad (2.4)$$

Accompanied with Ohm's law, the capacitive model as a theoretical tool can provides the direction for study, design, and optimization the performance of TENG[19-21].

More recently, with the deepening of the theoretical research of TENG, an electron-cloud-potential-well model was proposed to explain the electron-transfer-dominant mechanism of contact electrification as shown in Fig. 2.3.[22]

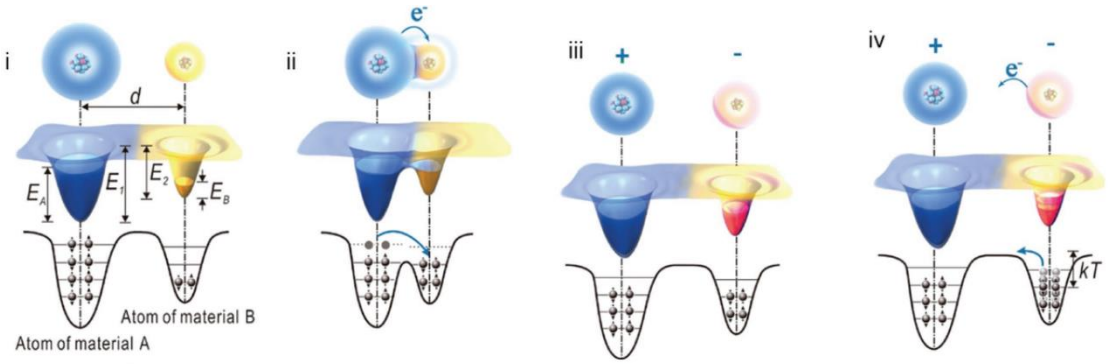

Fig. 2.3 Proposed electron-cloud-potential well model for the electron-transfer-dominant mechanism of contact-electrification.[22]

At the initial state (i), two friction materials A and B are separated with a gap distance. The two materials have different highest occupied energy levels, and the electrons are trapped in their potential wells, respectively. Their electron clouds are fully separated

with a distance of d. When the two materials are in contact, their electron clouds overlap and electron flow from A with higher energy states to B with lower energy states (ii). Most of the transferred electrons remain in B even after they separate, leading to the A with positive charges and B with negative charges (iii). When the temperature increases, the transferred electrons in B are thermionically emitted and hop out of the potential well, resulting in the reverse flow of electrons (iv). This explanation provides a new perspective for the mechanism of TENG, also offering invaluable insights for the TENG working under high-temperature.

2.1.2 Working models of TENG

Since the first report of TENG in 2012, there are four working modes have been proposed according to the device configuration and the direction of the movements as shown in Fig. 2.4.[23] They are vertical contact-separation mode, lateral-sliding mode, single-electrode mode, and freestanding mode, respectively.

The vertical contact-separation mode utilizes two friction layers with a gap distance. The electricity generates based on the periodic switching of the contact and separation states in the perpendicular direction. To achieve the vertical movements, different structures are designed such as arch-shaped,[24] zig-zag,[25] cantilever based,[26] and spring-supported[27] TENG device. TENG devices based on this mode outshine in repeated motions, alternating impact or shock. It is wildly used because of its simple structure, easy fabrication, great robustness and high instantaneous power density. This mode has been widely applied to harvest mechanical energy from human walking,[28,

29] finger typing,[30] and some biomedical microsystem.[31] Also, it can be applied in various self-powered sensor systems such as pressure sensor,[32] and acoustic sensors.[33] While the indispensable gap distance between two layers is a cavity along with changeable volume, hindering the package for the TENG.

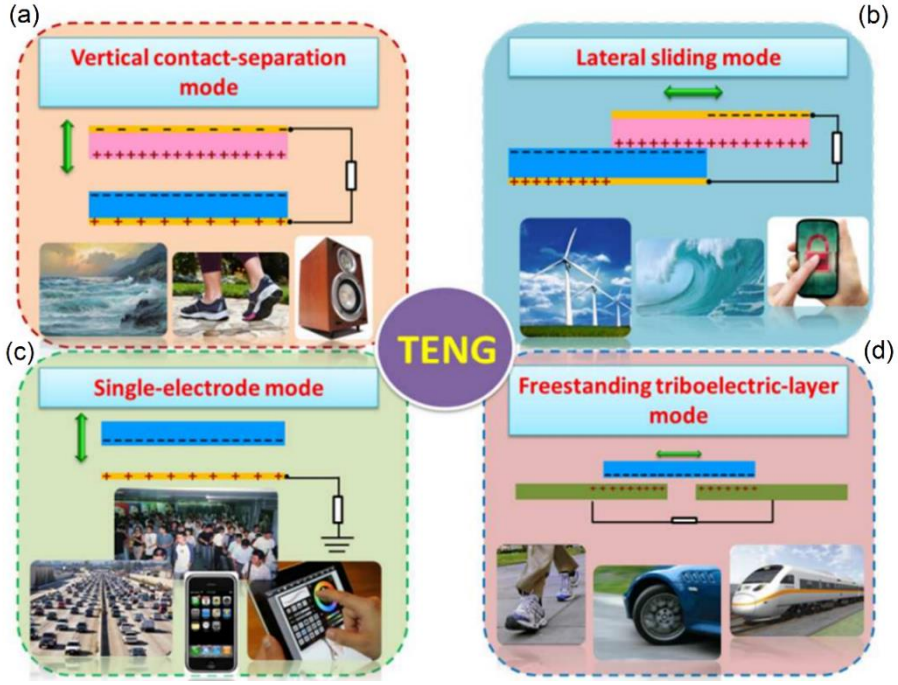

Fig. 2.4 Working modes of TENG. (a) Contact-separation mode; (b) Lateral-sliding mode; (c) Single-electrode mode;(d) Freestanding mode.[23]

The lateral-sliding mode employs two friction layers contact closely and the electric generates due to the relative displacement in the direction paralleling to the contact surfaces under external force. There are several advantages for this mode. The generated charges arising from the relative sliding in the contact surfaces is more effective, thus can improving the outputs of TENG device.[34] Furthermore, the structure design based on this mode is more diversiform. For example, it can implement in a compact package by the rotation sliding. Numerous researchers fabricated high-performance TENG device based on lateral sliding mode by introducing a grating

structure.[35-37] With improved sliding velocity and finer grating spaces, substantial enhancements of electric outputs can be achieved both in magnitude and frequency. The lateral sliding mode has been demonstrated to harvest energy from wind[38], hydropower,[39] and so on. For the above-mentioned modes, moving objects are bonded with electrodes and wires, impeding their application in harvesting energy from freely moving object.

Single electrode mode was created to solve this problem.[40] For this mode, ground was considered as one of the electrodes and it is adaptable for harvesting energy from moving object without the introduction of extra wires. For TENG based on single electrode mode, induced electrons transfer through electrodes, so it is not effective owing to the electrostatic screening effect.[41] However, because one triboelectric layer can move freely with no constraint, this mode has been employed to harvest energy from turning the book pages,[42] rain drop,[43] rotating tire,[44] and even air flow.[45] It can also apply in various self-powered sensors, such as displacement vector sensor[40] and angle measurement sensor.[46]

The freestanding triboelectric-layer mode is established based on single electrode mode but with a pair of symmetric electrodes rather than ground as the reference electrode. The electric outputs derive from the asymmetric distribution of charges in the two fixed electrode as the freely moving friction layer changes its position. For freestanding mode, without the screening, the electrostatic charges can reach the same number of triboelectric charges generated on the freely moving layer. In this mode, the two

electrodes are not in contact with each other, and it is efficient to scavenge energy from mechanical movements without any attached electrode.[47] Moreover, there is no material abrasion and heat generation even undergo long-term continuous working.[48] This feature makes it superior in robustness as well as energy conversion efficiency. This freestanding mode TENG has been used to harvest energy from computer mouse operation,[49] vibration,[50] air flow,[51] walking human or a moving automobile.[52, 53] It can also be applied in self-powered active micro-actuators.[54]

The four working modes all has their own advantages and defects. For practical application, the configuration of TENG is not restricted with only one single mode but relies on combination or hybridization of different modes to exploit their full advantages.

2.2 High performance triboelectric nanogenerator

As the first report of TENGs in 2012, the electrical performance of TENG has been significantly improved. From the origin mechanism of TENG, we can know the voltage and current are proportional to transferred charge density generated on contact surfaces, and the corresponding power density exhibits quadratic dependence on transferred charge density.[19] Meanwhile, the contact area, separated distances, and contact-separating frequencies also have significant influences on the output of TENG.[6] Enormous efforts have been devoted to boost the electric output of TENG through the optimized materials selection and construction of micro-nanostructures. To some extent, the development of high performance TENG motivates scientists to explore the basic

science and practical applications.

2.2.1 Materials selection

Triboelectrification is a type of surface effect, thus the friction materials and their surface morphologies can effectively influence the electric outputs of TENG devices. Typically, during electricity generation process, the charges generated on the surface of friction layer of TENG work as the source of electrostatic induction charges. As a result, to improve the electric outputs of TENG, increasing triboelectric charges through selecting friction materials and surface engineering are effective ways.

As known to all, almost all materials possess triboelectric effects, from natural wood to synthetic polymers, to metals and silk. These materials are all feasible to act as friction layers of TENG, that means, the possible combinations of friction materials seem innumerable. However, not every pair of materials can produce high output. From materials aspects, high electric outputs are strongly dependent on the polarity difference of friction materials. In the material aspect, high output is strongly dependent on the polarity difference of material pairs. Providentially, the triboelectric series on static charges was established by John Carl Wilcke in 1757, revealing the polarity sequence of different materials. A part of the series is shown in Fig. 2.5.

At the bottom of the sequence, the materials are prone to obtain electrons and negatively charged. Moreover, the materials close to the top of the sequence usually lose electrons and positively charged. The triboelectric series provides a guidance for selecting optimal triboelectric material pairs to achieve high outputs for practical application field.

The farer the two friction materials are in the triboelectric series, the higher outputs of the TENG.

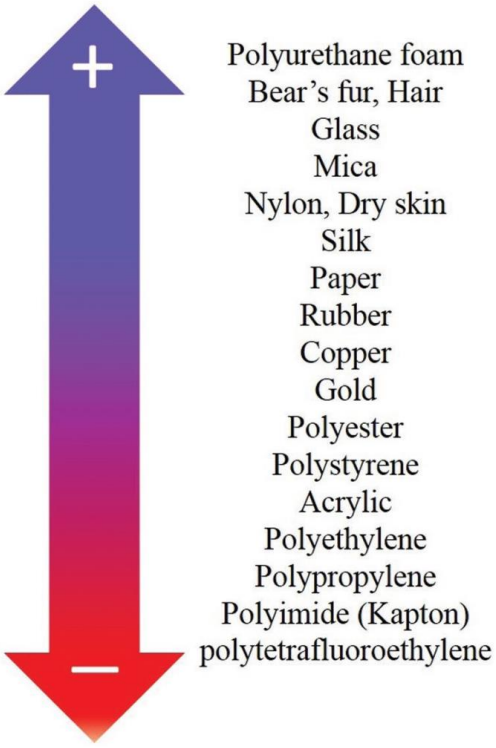

Fig. 2.5 Triboelectric materials in sequence following the ability of losing electrons (+) and to gaining electrons (-).[6]

For example, materials with fluorine containing functional groups can attract large amounts of electrons from their counterparts. Yoon et al. reviewed the research about TENG devices based on some fluorine containing materials such as PTFE, and PVDF, revealing high outputs.[55] Moreover, the design of TENG devices for some special purposes can also take advantage of this list. For example, in order to meet the requirements of environmentally friendliness, silk and paper, which are easy to loss electrons, are always used to fabricated biodegradable TENG.[56, 57]

2.2.2 Molecular surface modification

As mentioned above, the selection of friction materials to achieve high outputs of

TENG is significant according to the detailed function and the application situation. However, for some special application situation, such as some harsh environments, Kapton with good mechanical property is considered as the most suitable candidate. However, it cannot be easily charged by triboelectrification.[58] Thus, chemical modification is a wonderful strategy to combine two and more virtues in a single material. Introducing appropriate functional groups on the friction layers and charge injection are two main effective surface modification technique.[59-61]

Zhang et al[62] first reported the C_4F_8 plasma treated PDMS via an ICP system. After the treatment, PDMS surface was covered by a layer of C_4F_8 molecules and became rougher as shown in Fig. 2.6a. After a simple one-cycle treatment, the electric outputs of TENG dramatically enhanced from 124 to 193 V. And further improvement can be achieved by repeating the treatment cycles. Furthermore, first-principles calculations were employed to estimate the vertical ionization energy of PDMS before (8.98 eV) and after (12.31 eV) C_4F_8 plasma treatment as shown in Fig. 2.6b, indicating enhanced electron binding energy, which means the easier electron obtain of the PDMS surface.

Shin et al[63] proposed another effective method to modulate the polarity of PET film by introducing $-CF_3$ groups (negatively charged) coming from FOTS vapor and $-NH_3$ (positively charged) group coming from poly-l-lysine solution. The modification process is shown in Fig. 2.6c. After chemical modification, the electron affinities and hydrophilicity of PET surface change a lot. The electric outputs increase for many times due to the enlargement of the triboelectric polarities, suggesting the exceptional

effectiveness for the introduction of amino and fluorine groups as shown in Fig. 2.6d. The functionalized PET also exhibits excellent cycling stability owing to the stable chemical bonds formed on the surface as displayed in Fig. 2.6e.

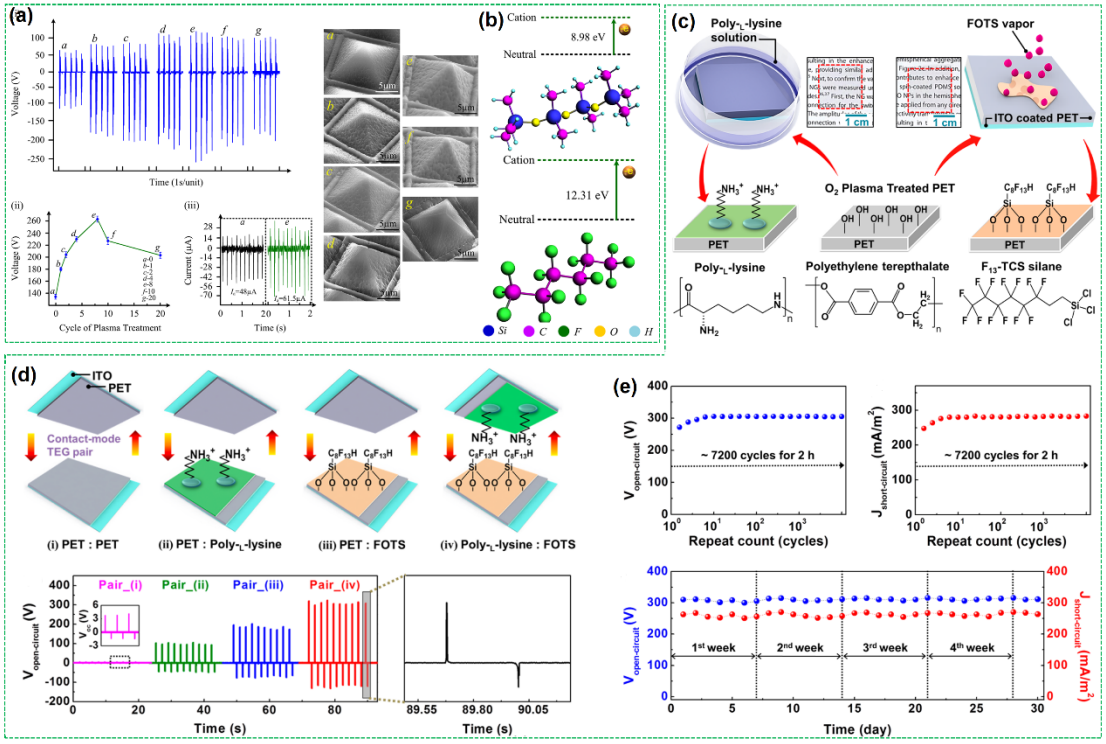

Fig. 2.6 (a) Chemical modification of the PDMS surface by C_4F_8 plasma; (b) the vertical ionization energy of PDMS before and after plasma treatment.[62] (c) Surface modification process of PET; (d) Electric outputs of TENG with various friction pairs; (e)cycling stability within one month.[63]

Another important and easy operating method to modify different surfaces is SAM method. Through this method, a well-ordered molecular layer of can be formed on the surface by the chemical adsorption of active surfactants. Wang et al[64] utilized SAM as an effective method under room temperature chemical to boost the performance of TENG. This method can not only be used for metal substrate, but also for the insulated substrate. A layer of Au was deposited on the surface of Kapton and then a SAM layer was formed on the deposited surface as shown in Fig. 2.7a. After the treatment in thiols

containing solutions, various functional groups can be formed on the Au surface, including hydroxyl, ester, amine, and chloro. The functionalized Au substrate and FEP layer were assembled as friction layers to measure the performance after modification as shown in Fig. 2.7b. The output shows significant enhancement in device of functionalization with amine groups. However, the friction layer with chloro group cause a weak decrease in electric output of the TENG.

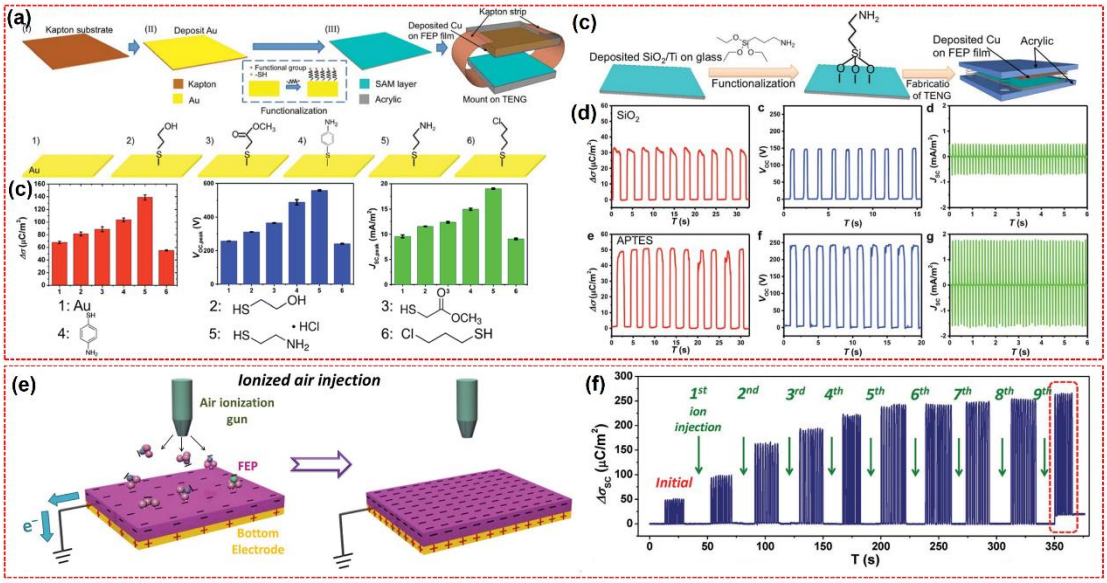

Fig. 2.7 (a) Fabrication procedure of Kapton film modified with SAM layer; (b) The electric outputs comparison TENG with various SAM layer. (c) Fabrication process of SiO_2 film with SAM layer; (d) Electric outputs comparison of the TENG based on SiO_2 friction layer before and after SAM functionalization.[64] (e) Main procedure of the ion injection based on FEP film; (f) Elevation of the $\Delta\delta_{SC}$ of TENG composed of FEP film with different ion injection time.[61]

Moreover, insulating friction surfaces such as SiO_2 was also modified by this approach as shown in Fig. 2.7c. After the modification with (3-aminopropyl) triethoxysilane, the electric outputs show obvious improvement as displayed in Fig. 2.7d.

Ion injection is also a new chemical modification approach for introducing surface

charges. It can be realized with the assistance of air-ionization guns. Ions with opposite polarities can be produced through initiating the air discharge inside the gun and these ions can be implanted onto the friction surfaces subsequently. This approach was recently reported by Wang et al[61] for the first time to efficiently improve the output of TENG. A basic viewpoint of the ion injection process is shown in Fig. 2.7e. Negative ions such as CO^{3-}, O^{2-}, O^{3-}, NO^{2-}, and NO^{3-} can be gradually injected into the top surface of FEP through an air-ionization gun. Meanwhile, positive charges will be induced on the electrode and then flow through ground electrode to reduce the electric field generated. Consequently, both the FEP friction surface and the electrode can be full of charges with the same density but opposite polarity. Fig. 2.7f reveals the enhancement of charge density of the TENG under short-circuit state for different injection times.

In addition to the chemical modification, nanomaterials doping into the bulk of friction materials is also an effective way to modulate their dielectric property. Various materials such as monolayer molybdenum disulfide,[65] titania monolayers,[66] reduced graphene oxide,[67] and graphene oxide[68] were all suitable for the electron-trapping sites in the bulk materials to enhance the outputs of TENG. Also, genetical engineering can be used to direct produce biomaterials with various polarities.[69]

2.2.3 Construction of micro-nano structure

Construction of micro-nano structures is also the effective way to boost the performance of TENG devices. The micro-nano structure on the friction surface can obviously enlarge the effective triboelectric contact area and increase the effective

dielectric constant.

Photolithography method is a common way to fabricate micro-nano structures with various shapes and dimensions. Fan et al[26] firstly introduced different micropatterns onto the friction surfaces and opened up the research on high performance TENG devices via enlarging the friction area through chemical or physical methods. In their work, patterned Si wafers constructed by photolithography method act as the mold to produce PDMS friction layer with various features including pyramids, cubes, and lines, as shown in Fig. 2.8a. The Si molds were coated with trimethylchlorosilane firstly to avoid the sticking of PDMS and the mold. Then, PDMS liquids were spin-coated onto the surface of the molds and heated for solidification. After cooling down, patterned PDMS layers were peeled off with designed surface morphologies. Finally, the PDMS layers were stuck to PET substrate and coated with ITO electrodes. Fig. 2.8b compares the electric outputs of TENG devices with various surface morphologies of PDMS. PDMS with pyramid-patterned based TENG device reveals the maximum output current and voltage, which are nearly 300% higher than smooth film-based TENG device.

ICP is also a common way to fabricate micro-nano structures. Zhu et al[58] utilized the ICP method to introduce aligned nanowires with large aspect ratios to the surface of Kapton film. The length and density of the nanowires can be modulated by adjusting the processing time of ICP and the thickness of the pre-deposited Au layer. The Kapton films are ion-milled with oxygen (O_2), carbon tetrafluoride (CF_4), and argon (Ar) as the

etching gases. The surface morphologies for various etching times and their electric outputs are exhibited in Fig. 2.8c and 2.8d. Only nanowires with suitable length benefit electric outputs as their elastic property and morphology can be well-retained after frequent separations and contacts, as shown in Fig. 2.8e. The ultralong nanowires fabricated with excessive etching time are prone to deforms, which damages the surface morphology and limit the enhancement of electric outputs.

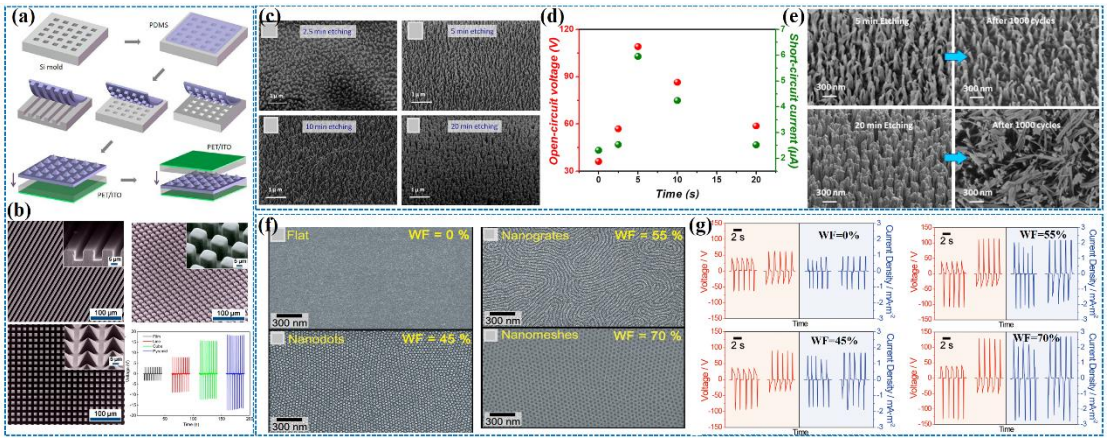

Fig. 2.8 (a) Fabrication procedure of PDMS friction surface with various features; (b) SEM images with different surface morphologies and their corresponding electric outputs of TENG.[26] (c) The morphologies of nanowires under various etching time; (d) related voltage and current outputs; (e) SEM images of the nanowires before and after contact-separation operation for 1000 s.[58] (f) SEM images of different surface morphologies generated through block copolymer technology; (g) the corresponding electrical output of TENG.[70]

Lee and co-workers utilized block copolymer method to construct micro-nano structures, which produce phase separation of polymers and overcome additional realize the formation of nano patterns with high spatial resolution such as rings, holes, dots, and lines, as shown in Fig. 2.8f.[70] The TENG devices based on the patterned polymer with nanogrates, nanodots, and nanomeshes the can achieved the output current density of 2.3 mA m^{-2}, 1.8 mA m^{-2}, and 2.8 mA m^{-2}, respectively, which is higher

than that of TENG with flat-surface(1.1 mA m^{-2}).

Spongy or porous structures can also promote the electric output of TENG due to their high capability. Lee et al[71] employed PS microspheres as the template to manufacture PDMS sponges with the pore sizes ranging from 0.5 to 10 μm, as displayed in Fig. 2.9a. For the fabrication process, a layer of PS microspheres is grown on the surface of SiO_2/Si substrate and then PDMS liquids are poured to encapsulate them. After solidification, microspheres are carefully removed by etching and the sponge friction layer was fabricated after adherence of the Al electrode. The electric outputs of TENG with sponge structure can achieve 0.10 mA cm^{-2} and 130 V, respectively, which are much higher than these of flat TENG device (0.02 mA cm^{-2} and 50 V) with the same measurement conditions as shown in Fig. 2.9b. The improved electric outputs can be attributed to the shrinkage of pores, which can dramatically enlarge the contact area. Inspired by this research, Chun et al[72] reported an effective and scalable method to fabricate the porous PDMS films through water assistance as the soft template. Water evaporated during the solidification process and left numerous pores. Then Au nanoparticles were incorporated into the porous PDMS film as effective dielectrics to promote the electric outputs of TENG devices, as elucidated in Fig. 2.9c. This approach provides a favorable way to build up mass-producible and largescale self-powered electronic devices based on TENGs due to its quite simple fabrication process. The as-obtained TENG device with porous structure shows a maximum power of 13 mW, demonstrating a more than fivefold improvement compared to that of TENG with flat

film owing to the aligned dipoles arising from the inner contact between PDMS and Au nanoparticles. The proposed structures are insensitive to the change of environmental humidity, suggesting its application in critical environments with high humidity, such as in water.

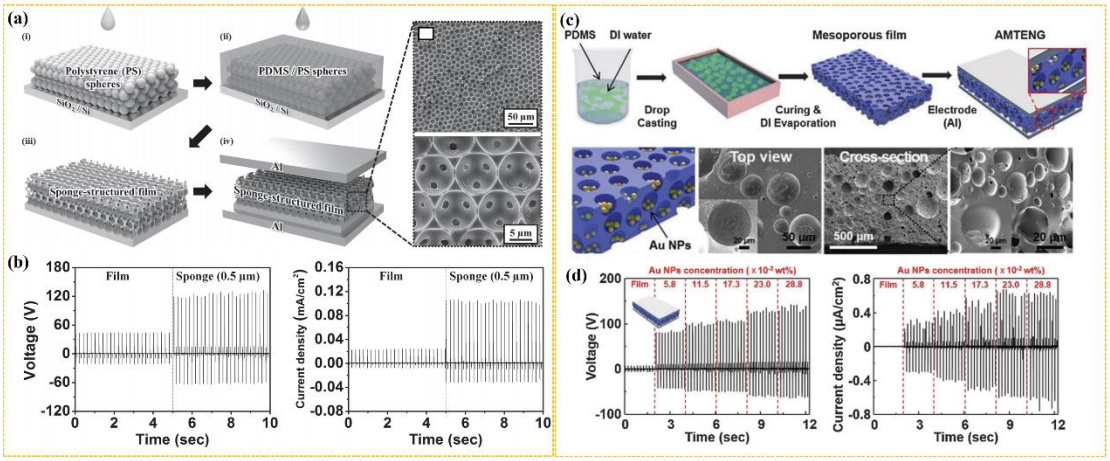

Fig. 2.9 (a) The fabrication process of hydrophobic TENG with sponge structure; (b) Electric outputs of sponge TENG.[71] (c) Fabrication procedures of TENG with porous structure embedded with Au nanoparticles; (d) Electric outputs of TENG with porous structure.[72]

Moreover, there also exist some facile templates for constructing micro-nano structures, including anodic aluminum oxide template,[73] zinc oxide nanorods fabricated with low-temperature hydrothermal process,[74] and natural templates.[75] In addition to modification approaches for only one side, researchers also focus on the construction of micro-nanopatterns on both friction layers to further boost the electric output performance.[31]

Triboelectric materials not only include polymers, some metals, metal oxides, silk and woods can also be used for triboelectric materials. Zhu et al[76] originally introduced an layer of nanoparticles on the Au surface through a chemically synthesized method.

Similarly, another effective way to modify the metal surface was presented by Park et al[77] by water-assisted oxidation process. This approach only requires hot water instead of complex treatments or expensive equipment. High densely packed micro-nano structures can be obtained on various metal surfaces such as zinc, aluminum, and copper.

3D printing, also named as additive manufacturing or rapid prototyping, illustrates the process where printable materials solidified layer by layer to finally form 3D objects. 3D printing process usually starts with computer-assisted 3D modeling, and then the 3D model is sliced to 2D images with certain thickness which are sent to 3D printing devices for printing. It provides an effective and eco-friendly way to construction microstructure without the introduce of any templates. Chen et al[78] employed the direct ink writing method to fabricate the friction layers of TENG device. The TENG devices are designed and fabricated through a single integrated procedure without further assembling steps as shown in Fig. 2.10a. In the TENG device, biodegradable poly(glycerol sebacate) serves as one of the friction materials, and carbon nanotubes act as the other friction material and electrodes simultaneously. The 3D printing TENG with hierarchical porous structure exhibits higher output efficiency compared with microporous TENG fabricated with traditional method as displayed in Fig. 2.10b. Huang et al[79] proposed a femtosecond laser direct writing method to construct micro-nano structures on the friction surfaces. With the laser scanning ablation method, the stripes and cones structures with micro-nano scale are fabricated on the surfaces of Cu

film. And with single pulse irradiation, micro-bowls structure with various sizes are fabricated on the surface of PDMS as shown in Fig. 2.10c. TENG device composed of Cu and PDMS layers with microstructure can achieves about 21 times enhancement in power density compared with flat one as shown in Fig. 2.10d.

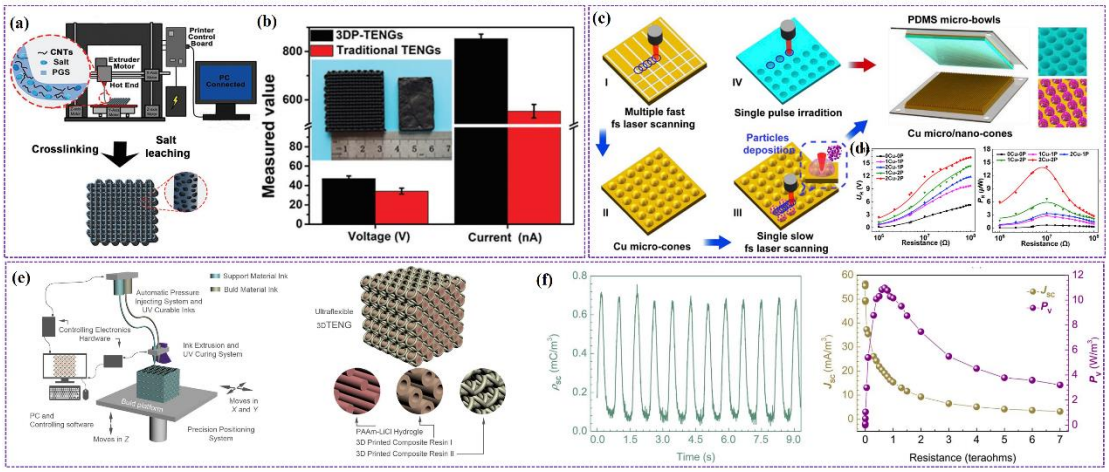

Fig. 2.10 (a) Schematic diagram of the fabrication process of the TENG based on direct ink writing method and the porous structure; (b)The comparison of electric outputs of the porous 3D printing TENG and TNEGs fabricated with traditional molding method.[78] (c) Femtosecond laser direct writing processes for constructing micro-nanostructures on the surfaces of Cu and PDMS films; (d) Enhanced electric outputs of TENG with micro-nano structures.[79] (e) Schematic of the hybrid 3D printing system used to fabricate flexible TENG; (f) Electric outputs of the fabricated TENG device.[80]

Chen et al[80] reported a unique additive manufacturing technology-UV 3D printing hybrid technology as shown in Fig. 2.10e. The TENG is made up of printed composite resin parts and ionic hydrogel as the electrification layer and electrode. A sustainable and decent output of 10.98 W/m^3 and 0.65 mC/m^3 are produced.

2.3 Self-charging system based on triboelectric nanogenerator

TENG devices possess numerous advantages including various structure designs for harvesting various mechanical energies from environment, broad materials selection to

realize the fabrication of flexible and wearable electronics, and high outputs for harvesting mechanical energies at low frequency (compared with electromagnetic generators), especially at frequency <5 Hz. These outstanding features make TENG device become the most competitive candidate for harvesting irregular and low frequency mechanical energies. However, the TENG has the pulsed alternative outputs, and the mechanical energy input is usually unstable. Consequently, storing the generated electrical energy from TENG in energy storage devices is indispensable to provide stable and continuous power supply for some wearable electronics. Recently, TENG devices as the energy harvesting component have been combined with various energy storage component including batteries,[81] supercapacitors,[82] dye-sensitized solar cells[83] to construct SCPS.

2.3.1 Brief introduction of supercapacitors

With the growing demand for portable and wearable power supplies in electric vehicles, mobile electronics, and the Internet of Things, energy storage devices, especially electrochemical energy storage devices which can reversibly storage and release electricity, have attracted much attention. Ideally, electrochemical energy storage devices should meet the requirements for storing enormous amounts of energy (high energy density), and they also should be charged and discharged in a short time (high power density).

There exist four main electrochemical energy storage devices, which is fuel cells, batteries, supercapacitors, and capacitors. Fig. 2.11 compares the energy density and

power density of these electrochemical energy storage devices. Fuel cells have ultrahigh energy density but burdened with low power density arising from the slow kinetics. Also, they need expensive metal catalysts. For traditional capacitors, they possess high power density but limited by their ultralow energy density. Therefore, batteries and supercapacitors have gradually become the main electrochemical energy storage devices in nowadays market. Batteries present high energy density with moderate power density, while supercapacitors exhibit ultrahigh power density with inferior energy density.

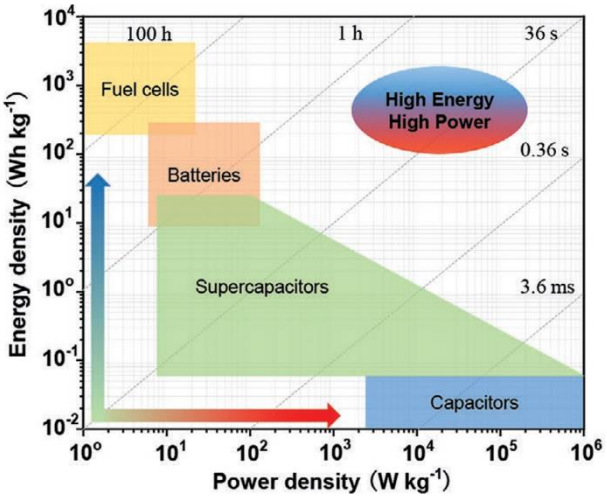

Fig. 2.11 Ragone plots of various electrochemical energy storage devices.[2]

The difference between batteries and supercapacitors can be attributed to the difference of energy storage mechanisms. For battery materials, they store energy (~200 Wh kg^{-1}) mainly by diffusion-controlled redox reactions, causing slow charging process with low power density (≤1 kW kg^{-1}). Conversely, capacitive materials store lower energy density (~5 Wh kg^{-1}) with fast charging process and high power density (~10 kW kg^{-1}) by the electrical double layers mechanism.[2] In this thesis, we mainly introduce the

SCPS composed of TENG devices and supercapacitors owing to their ultrahigh power density, ultralong cycle life, and fast charge/discharge rate comparing with fuel cells and batteries.

The fundamental configuration of a supercapacitor is composed of four parts, including current collector, electroactive materials, separators and electrolyte as displayed in Fig. 2.12. The current collector with highly conductive can provide pathway for the rapid transportation of electrons to external circuit. Electrolyte offers ions to freely delivered to the surface of electrode. Separator is used to separate the anode and cathode to avoid short circuit.

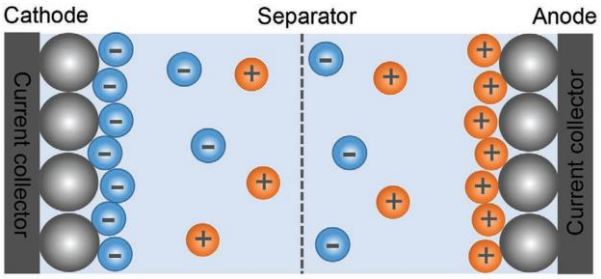

Fig. 2.12 The basic configuration of a supercapacitor.[2]

In theory, there exist two energy storage mechanisms for SC devices. The first one is EDLC, where the capacity mainly arise from the adsorption and desorption of the electrolyte ions with opposite polarity on the surface of electrodes. The fundamental model is Stern model as depicted in Fig. 2.13a. The typical electroactive materials based on EDLC mechanism are carbon materials and their derivatives, including onion carbon, graphene, active carbon and so on.[84] The other one is PC, which is based on the rapid and reversible redox reactions at the surface between electroactive materials and

electrolyte ions as shown in Fig. 2.13b.[85] RuO_2, MnO_2 and conducting polymer (PANi, PPy, Pth) are typical PC materials.[86]

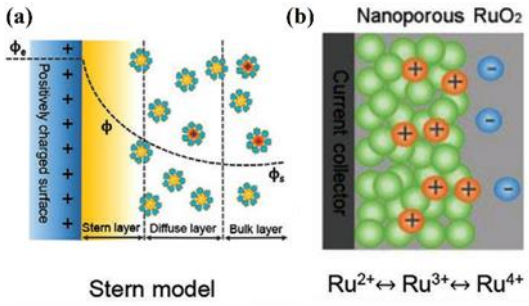

Fig. 2.13 Storage mechanism of supercapacitors. (a) Electric double-layer capacitor; (b) pseudocapacitors.[2]

Recently, according to the different charge storage mechanism, there are more elaborated classifications as shown in Fig. 2.14. The primary electrochemical feature which can distinguishes SCs from batteries is that the voltage is constantly shows linear relationship with current in typical SC electrodes.[87] Particularly, through the entire charge/discharge processes, the CV curves for typical SC should maintain the rectangular shape, and the current always keep constant which is independent to the magnitude of voltage and changes with the change of voltage polarity.[88] While the battery reveals separated and strong peaks along with obvious Faradaic reactions as displayed in Fig. 2.14a.[89] Moreover, the GCD curve of the SC exhibits almost symmetric triangle shape composed of smooth oblique line with constant slopes. However, the battery shows obvious charge/discharge plateau at certain voltage stage as shown in Fig. 2.14b. There are also different kinds of energy storage materials in SCs systems based on various energy-storage mechanisms. According to the various electrochemical features from CV and GCD curves, electroactive materials can be

divided into EDLC materials, pseudocapacitive materials (intercalation and surface redox) and Faradaic materials (Faradaic dominated and battery-like).[90] For EDLC materials, CV curves show rectangular shapes (Fig. 2.14c) and GCD curves exhibit triangular shapes (Fig. 2.14d).[91]

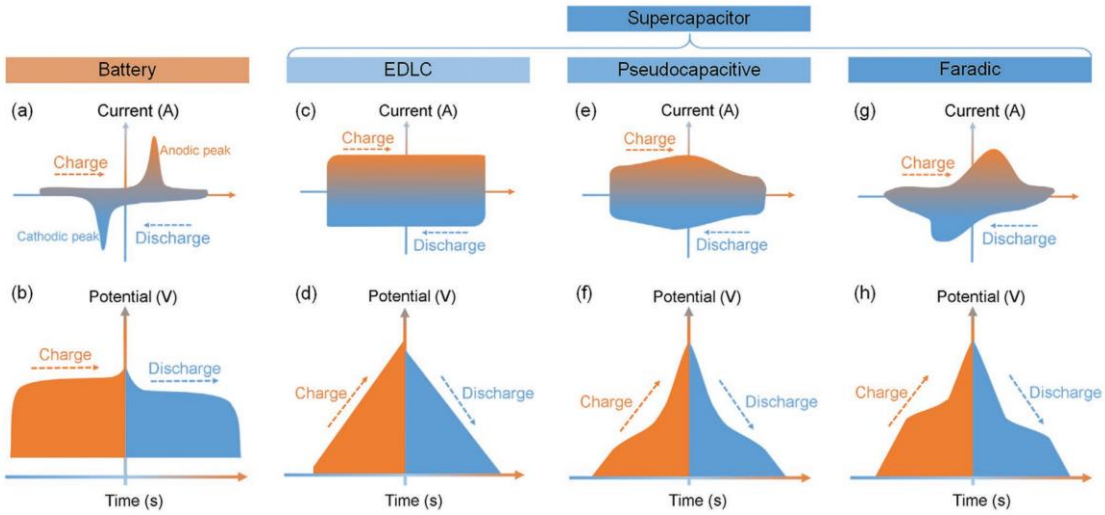

Fig. 2.14 Comparison of the electrochemical behavior for a typical battery and supercapacitor. Typical CV and GCD curves of (a, b) battery and supercapacitor: (c, d) EDLC materials; (e, f) Pseudocapacitive materials (surface redox, intercalation, and partial redox-intercalation); (g, h) Faradic materials (Faradic dominated and battery-like).[2]

Pseudocapacitive electroactive materials such as RuO_2 and MnO_2 store charge in two ways: (i) Faradaic electron transfer during the redox of metal atoms.[92] (ii) Non-Faradaic charge storage in the electric double layer occurs at the interfaces between electroactive materials and electrolyte.[93] Their CV curves seem similar with EDLC materials with pseudo-rectangular shapes (Fig. 2.14e). And the GCD curves are analogous triangular shapes (Fig. 2.14f).

For some typical electroactive materials like nickel/cobalt oxides, hydroxides or phosphate, their CV curves always feature prominent and widely separated peaks as

shown in Fig. 2.14g. And their GCD curves show relatively flat charge/discharge plateau (Fig. 2.14h). Therefore, the nickel/cobalt based composites usually represent battery-type Faradaic materials and should not be considered as the pseudocapacitive materials.[94-96] Above all, pseudocapacitive materials usually store charges through Faradaic mechanism while with characteristic whose capacitive signature in electrochemical measurements. The stored charges show linear relationship with potential. However, some typical nickel-based composites do not show obvious capacitive feature and cannot be regarded as pseudocapacitive materials owing to the phase transitions and Faradaic mechanism. To properly define the energy storage characteristics for the battery-type materials, mAh g^{-1} or C g^{-1} should be employed to quantify the capacitive performance.

As mentioned above, any electroactive material showing intense, obviously separated redox peaks in CV curves or clear plateaus in GCD curves should be categorized as the battery-type electrode. The capacitor types electroactive materials possess rectangular CV curves and triangle shaped curves for the charge/discharge process under constant current density.

For all types of SC devices, the energy storage happens at the interface between the electrode and electrolyte ions, thus SC can provide the excellent power density with the fast charge/discharge behavior. Nowadays SC devices have exhibited huge application in hybrid platforms for buses, light rail, and load-leveling systems for intermittent renewable energy sources for their maintenance-free, and high power density. However,

the SC devices still maintain relatively low energy density owing to the limitation of the total amount of charges stored on the electrode surfaces, which severely hindering the broad application of SC devices. Thus, there are intense research efforts to realize high energy density of SC devices, to approach or even exceed batteries, without deteriorating their outstanding power density and cycling stability.

According to the equation $E = 1/2\ CV^2$, the energy density (E) of SC devices is in proportion to their specific capacitance (C) and the square of the operating potential windows (V). There are two directions to boost the energy density of SC devices: broadening the potential window and expanding the specific capacitance of electroactive materials.[97] Theoretically, reasonably assembling ASSCs delivers a prospect to effectively widen the working voltage windows by combining cathode and anode materials with opposite operating voltage windows, which can result in improved energy density to realize the potential applications. During the charging-discharging processes, ASSC devices can take the advantage of positive and negative electrodes with separated potential windows to expand the operating voltage range of the device as shown in Fig. 2.15a and 15b. With the wide voltage window, ASSC devices exhibits much higher energy density than symmetric SC devices. For example, the operating voltage window of the aqueous symmetric SC devices are usually limited to ~1.2 V because the thermodynamic breakdown of water molecules would induce the generation of hydrogen and oxygen gases. While for the ASSC devices, the working voltage range can expand beyond 2.0 V for the voltage assigned to each electrode is

less than 1.2 V.[98] Therefore, constructing ASSC devices with wide working voltage is a favorable technology to closely reach the purpose of high energy density.

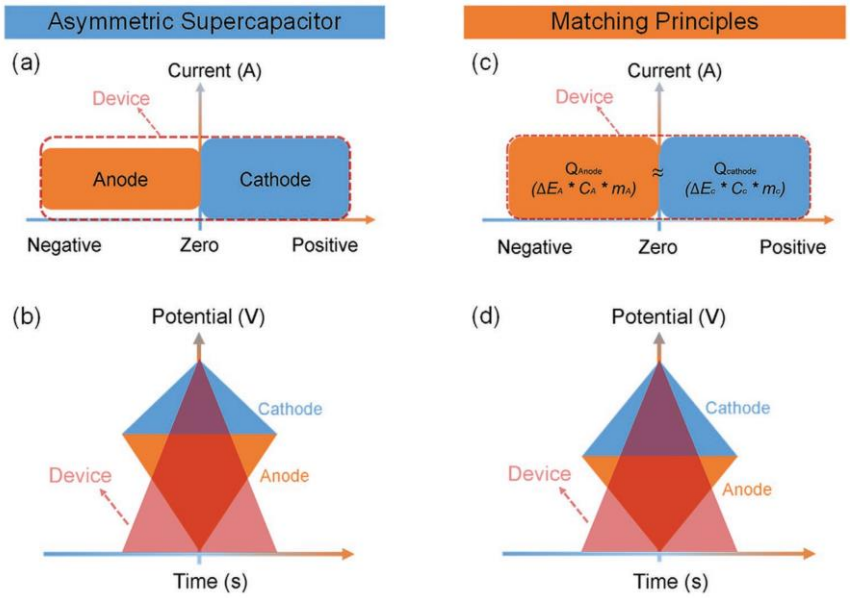

Fig. 2.15 Graphic illustration of the characteristic CV curves (a) and GCD curves (b) of ASSC device. (c) Schematic illustration of the matching principles in ASSC devices and (d) their typical GCD curves.[2]

The usage of organic electrolytes or ionic liquids is also efficient methods to extend the operating voltage. However, the lower ionic conductivity, higher viscosity, high volatility, flammability, and strict assembly environment lead to higher internal resistances and lower specific capacitance, which hinders their broad application.[93] Thus, fabricating aqueous ASSC devices with broad operating voltage windows is of great importance.

To achieve the optimal performance of a ASSC device, charge balance between cathode and anode should be considered as shown in Fig. 2.15 c and 15d. The total charge stored in the electrode is calculated based on $Q = C \times m \times \Delta E$. To realize the charge balance ($Q_+ = Q_-$), the mass loading of cathode and anode should be calculated according to:

$$\frac{m_+}{m_-} = \frac{C_- \Delta E_-}{C_+ \Delta E_+} \qquad (2.5)$$

Where m represents the mass loading of electroactive materials; *C* is the specific capacity of electroactive materials; and *E* reveals the working potential windows of electroactive materials.

Before measuring the electrochemical performance of the ASSC device, CV and GCD should be measured firstly using a three-electrode cell to determine the most stable working voltage windows and specific capacitances for both cathode and anode. Moreover, the mass loading of both cathode and anode should be precisely evaluated to achieve the theoretical maximum energy density.

Another direction for improving the energy density focuses on the improving of specific capacitance for both anode and cathode. From the electrodes' perspective, the perfect materials should contain the following disadvantages including large specific surface area, excellent conductivity, favorable mechanical and electrochemical stability, and low cost.[99]

The critical issue for ASSC devices to boost the energy density is to increase the specific capacitance, that means to increase the number of charges stored in the electrode. For EDLC, the capacitance is directly proportional to the accessible surface area. It is critical to increase the specific surface area of electrode. For instance, Li et al[100] fabricated the carbon nanofibers with mesopores presented a high specific surface area of 1725 $m^2 g^{-1}$, yielding a significant specific capacitance of 280 F g^{-1}, which is higher than 202 F g^{-1} for commercial activated carbons as shown in Fig. 2.16a. Besides,

specific surface area also plays an important role for PC devices. For example, porous MnO_2 spheres with hierarchical structure possesses a high specific surface area of 215 $m^2\ g^{-1}$ and delivers a high specific capacitance of 147 F g^{-1}, which is much higher than MnO_2 nanoneedles with much smaller specific surface area of 36 $m^2\ g^{-1}$.[101] In the meantime, the porous microstructure can also provide sufficient diffusion channels for ions, leading to the improvement of capacitance. Also, the porous structure can also effectively alleviate the stress under fast charge/discharge, resulting in the excellent stability. Therefore, it is essential to modulate the morphology and microstructure of electroactive materials. However, electrochemical materials with nanostructures always suffer from poor conductivity due to the large contact interfaces. Integration them with materials with high conductivity, including graphene, CNTs, and metallic media have been proven an effective way to improve the capacitive properties.[2] Though various powder form electroactive materials with micro-nano structures have been discovered and developed for realizing high capacitance, the addition of binder hinder the further boost of capacitive performance severely owing to the sluggish electron and ion transport. Therefore, it is important to construct self-supporting electrode where electroactive materials directly grow on the conductive substrates to reduce the contact resistance and enhance the electrochemical performance.

Kong et al[102] fabricated a self-supporting electrode with carbon textile as the substrate to grow $NiCo_2O_4$ nanowires coated with PPy to enhance the capacitive performance as shown in Fig. 2.16b. The as-obtained electrode delivers a high specific

capacitance of 2244 F g^{-1}, accompanying with an outstanding rate capability, and excellent cycling stability.

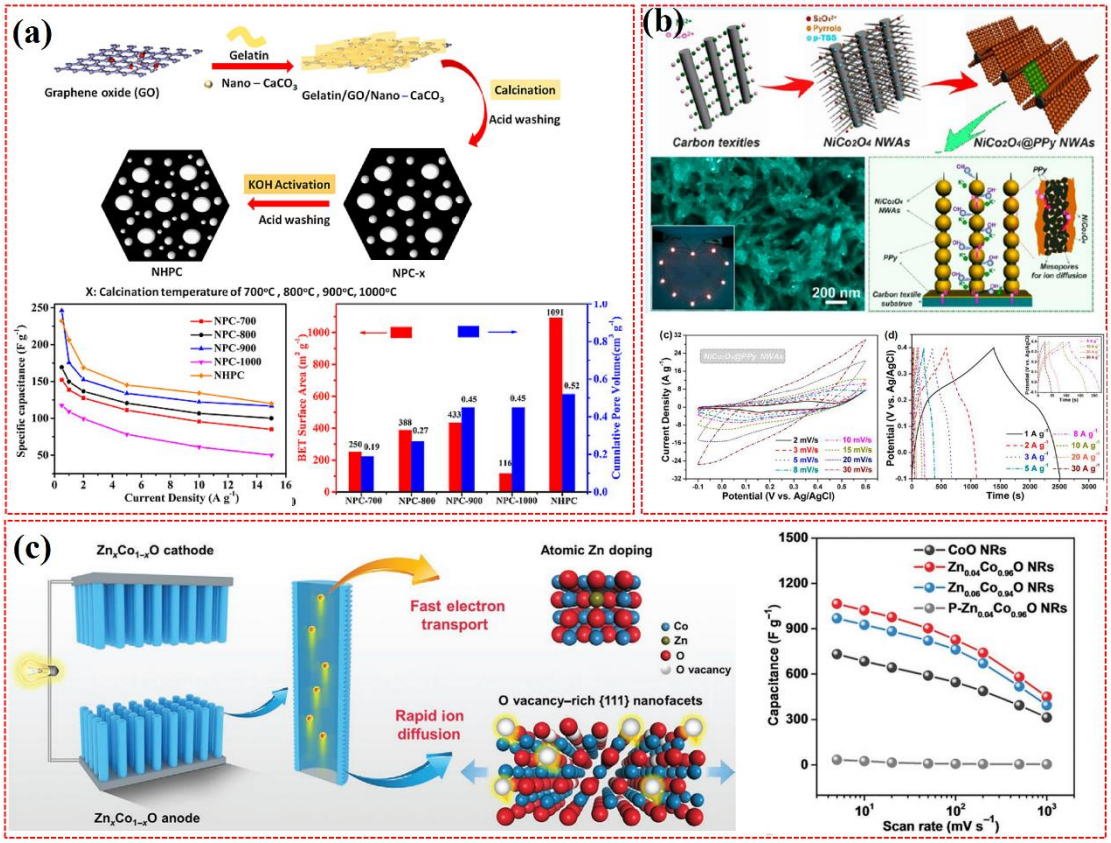

Fig. 2.16 (a) Fabrication of nitrogen-doped hierarchical porous carbon and its capacitive performance.[100] (b) Construction of hierarchical $NiCo_2O_4$@PPy nanowires on carbon textiles and corresponding capacitive performance.[102] (c) Fabrication of $Zn_xCo_{1-x}O$ electrode with atomic-level engineering and its specific capacity.[103]

To increase the electrochemical active sites, doping is a common method. Various dopants, such as metal, nonmetal and multi-elements are utilized to realize the target. For example, Ling et al[103] proposed the Zn-doped CoO electrode through atomic-level structure modulating to adjust the capacitive behaviors as shown in Fig. 2.16c. The conductivity $Zn_xCo_{1-x}O$ electrodes show obvious enhancement after the introduction of Zn atoms accompanying with the presence of oxygen vacancy.

Consequently, the electrode demonstrated a superior capacitance and outstanding rate capability.

2.3.2 Construction of self-charging system

TENG devices can harvest abundant mechanical energy in the surrounding environment. Supercapacitor devices are the most promising energy storage candidate to offer long cycle life, favorable flexibility, excellent portability, and reliable safety. In consideration of the advantages mentioned above, integrating TENG device with SC can develop a sustainable self-charging power system by harvesting mechanical energy in our daily lives.

Wang et al[82] first proposed a fiber SCPS, which is composed of a fiber-shaped TENG and fiber-shaped SC. The fiber SC is fabricated with carbon fiber as the substrate. Electroactive materials were synthesized by vapor-phase hydrothermal method. Meanwhile, TENG device was assembled with cotton cloth and parylene coated polyester. TENG and SC devices are connected through a rectifier to convert the AC output from TENG to DC output to charge SC. The three yarn SC devices connected in series can be charged by the TENG to 2.1 V. The charged SC device later can discharge at 1 μA for 811 s, confirming the authenticity of the self-charging power textile as shown in Fig. 2.17a. Luo et al[104] fabricated a transparent and flexible thin-film based SCPS, as displayed in Fig. 2.17b. The ITO film with grid was used as the electrode of TENG device. SC device with Au@MnO_2 interdigitated electrodes were constructed on the back of TENG. The SCPS can harvest various mechanical motions and can store

the generated electricity to power small electronics. The above SCPS combined TENG device and SC device together with the separated rectifying circuit as the medium. Yi et al. reported fully packaged SCPS which is also stretchable and waterproof to harvest mechanical energy from various deformation as shown in Fig. 2.17c.[105]

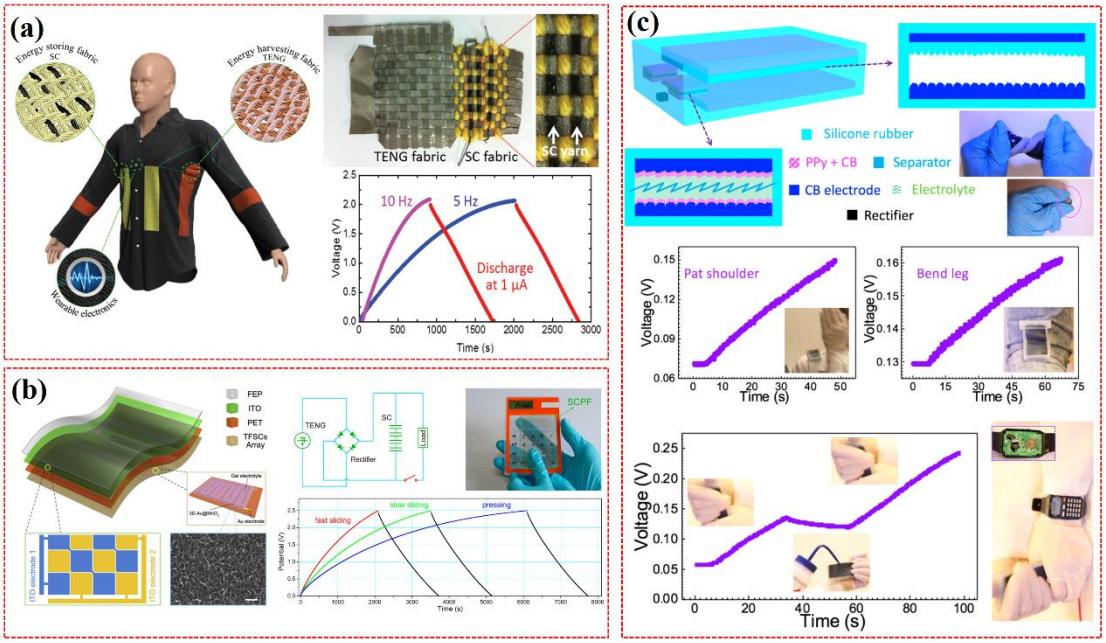

Fig. 2.17 SCPS based on TENG and SC. (a) All fiber shaped SCPS.[82] (b) Film-based SCPS.[104] (c) Package structure based SCPS.[105]

The TENG, SC, and rectifying circuit were all encapsule in the silicone rubber to form a package. For the fabrication of electrode for the stretchable TENG, a layer of carbon black covered on the silicone rubber. A layer of PPy and carbon black mixture was served as the electroactive materials of SC device. The mechanical energies from stretching, twisting, bending, and pressing can be harvested and stored in the SC device. Furthermore, the stored energy can be used to power a watch.

2.4 Summary

In this chapter, we review the mechanism, working models of TENG. The main

consideration for fabrication of high performance TENG is also introduced. The configuration, mechanism, materials and method for high performance SC are introduced in detail. Finally, SCPS based on TENG and SC with diverse types are reviewed.

The mechanism of TENG can be attributed to the Maxwell's displacement current. To meet the various requirement for practical application, four working models are proposed including contact-separation model, lateral-sliding model, single-electrode model and free-standing model. Based on the mechanism of TENG, the electric outputs are in proportional to the triboelectric charge density generated on interface between two friction layers, and consequently, the output power reveals a quadratic dependence on the charge density. Meanwhile, the contact area, separated distances, and contact-separating frequencies also have considerable influence on the outputs of TENG. To improve the triboelectric charge density, there are two main strategies. The former one is to select friction materials apart from each other in the series sequence. The latter one is to modify the friction surface through physical doping, chemical modifying and even biogenetic engineering. Moreover, constructing micro-nano structures on friction surface is another direction to boost the electric outputs of TENG because it can enhance the effective contact area. Various methods can be employed to construct micro-nano structures such as photolithography, hard template, biological template and 3D printing.

SC devices can store energy, so the energy density and power density are two critical

parameters for practical application. Electroactive materials for SC device usually possess high power density, thus improving energy density is the main exploration direction. Enlarging the operating voltage windows and improving the specific capacitance can effectively improve the energy density. To realize the broad working potential range, anode and cathode materials with separate working potential windows should be selected for the assemble of ASSC device. To improve the specific capacitance, fabricating nanomaterials, constructing self-supporting electrode and doping are all effective approaches.

The construction of SCPS based on TENG and SC can harvest mechanical energy from surrounding environment and stored the energy in SC device for further application. There are three types SCPS that is fiber-shaped, film-shaped and all package structure. For all SCPS, the mechanical energy can be harvested by TENG device and stored in SC to further power some small electronics. However, the SCPS also suffers from poor long-time stability due to the slow charge process caused by the low outputs of TENG and frequent charge-discharge due to the low capacity of SC. Therefore, it is important to fabricate SCPS composed of TENG with high outputs and SC with high capacity to achieve its long lifetime.

Chapter 3 High-performance Triboelectric nanogenerator based on direct image lithography and surface fluorination

3.1 Introduction

Through coupling of interfacial triboelectric effect and electrostatic induction, TENG has emerged as a milestone energy harvest technology.[7] The TENG can convert various mechanical movements such as human motions,[11] ocean waves,[10] wind,[8] droplets,[9] even acoustic flow,[13] and heart beats[12] into electricity. As a promising alternative portable power sources, the TENG exhibits great potential to act as energy supply system for the wearable electronics due to its light weight, convenient fabrication, low cost, abundant materials selection, and high efficiency under low frequency mechanical movement, etc.[7] Based on the well-established Maxwell's displacement current model of TENG, the electric output of TENG shows a proportional dependence on the surface charge density.[7] Meanwhile, the contact area,[41] separated distances,[106] and contact-separating frequencies[107] also have significant influences on the output of TENG.

Enormous efforts have been devoted to boost the electric output of TENG for its commercialization and practical application.[41] On one hand, numerous studies are channeled to increase the triboelectric charge density and prevent charges loss in the triboelectric materials from surface to bulk, which includes the optimized materials selection referred to the electron affinity, chemical surface modification (such as PtBA-grafting,[108] CF_4 etching,[109] self-assembled monolayer method[110]) and physical

doping (such as carbon nanotubes[111] and metal particles[72] embedded in polymer matrix). On the other hand, enlarging contact area by constructing micro-nanostructures on the surface of triboelectric layers is another effective way to enhance the electric output. Substantial methods have been used to manipulate the micro-nanostructures, such as Si template,[112] anodic aluminum oxide template,[113] photolithography,[114] and biological template (flower petals[115] and leaves[116]), etc. Although these methods have made commendable contribution to increase the outputs of TENG, they still suffer from several drawbacks including expensive and complicated instruments, sophisticated fabrication procedures, limited increase of contact electrification area and requiring large amounts of templates, etc. Above all, when the micro-nanostructure changes, the templates also need to be totally replaced, which consumes a lot of time and materials during the preparation process. Hence, a new method of fabricating micro-nanostructures in TENG without any templates is greatly needed.

3D printing, also known as additive manufacturing, provides a convenient and versatile method for template-free fabrication of micro-nano structures because of its low cost, high speed, and simple operation.[117] Various 3D printing technologies have been used to fabricate TENG devices, including femtosecond laser direct writing,[79] direct ink writing,[78] and fused deposition modeling.[118] However, the previous reports mainly focus on the two-dimensional structure with finite height, straight tubular cylinders, or polymer tubes with unclear bounds because of the low fabrication precision for casting or forging method. Direct image lithography depends on the spatial

and temporal control of illumination sources to selectively photopolymerize the liquid pre-polymer to form solid objects layer by layer without the utilization of molding terrace[119]. It is considered as an efficient and commercially attractive technique for constructing with microstructures due to its high resolution, large molding area and ultrafast molding speed.

In this chapter, a PU layer with surface microcones structure was firstly fabricated by DIL technology within 3 minutes without any templates. By changing the printing models and exposure time during the printing process, PU layer with microcones structure of different microcones density and heights can be obtained. By setting the printing parameters, PU layer with different dimensions can be fabricated. F-PU layer was then fabricated through oxygen plasma followed with fluorination with FOTS vapor treatment. The influence of each treatment process is studied. And the details of FOTS treatment, including treatment temperature, time, and the amount, are investigated. The TENG device composed of the PU and F-PU layer with microstructures exhibits a distinct enhancement in the output compared with the TENG with flat structure. The TENG device can achieve a maximum current output of 22 μA with the transferred charges of 192 nC. The device can obtain a maximum output power density of 1.5 W/m^2 with excellent cycling stability.

3.2 Materials and equipment

3.2.1 Materials

The commercial elastic PU resin is purchased from LuxCreo Co.Ltd. The

trichloro(1H,1H,2H,2H-perfluorooctyl) silane and commercial 3 M FC-3283 perfluorocarbon liquid were purchased from Sigma-Aladdin.

3.2.2 Equipment

The equipment used in this chapter was listed in the table below.

Table 3.1 The equipment for the preparation and characterization of TENG device.

Equipment	Model	Producers
DLP 3D printer	TP-02	LuxCreo co.
Plasma cleaner	TS-PL10	Tonson Hi-Tech co.
Mixing and defoaming machine	ARE-310	Shenzhen cias industrial equipment co.
Acrylic glove box	AGB-002B	MBITIOUS co.
Scanning electron microscope	Sigma VP	Zeiss
Fourier transform infrared spectrometer	Nicolet iS50R	Thermofisher Scientific
Optical microscopy	VHX-7000N	Keyence
Surface profiler	VR-5200	Keyence
Electrometer	6514	Keithley
Force gauge	Series 7 M7-100	Mark-10
Linear motor	K05-W/C-4	LinMot

3.3 Methodology

3.3.1 Fabrication of TENG device

Firstly, 3D models with different density of microcones were obtained by 3d Max software. A commercial elastic PU resin with photocurable component and thermosetting component and the corresponding curing reagent were purchased from Luxcreo company. The modeling material composed of PU and curing reagent were fully mixed by the mixing and defoaming machine under 2000 rpm for 5 min. The model is composed of two parts, that is the bottom part (50 mm × 50mm × 10 mm) and microcones part with the diameters of 300 μm. The density of the microcones can be controlled by adjusting the distance between the two adjacent microcones. The 3D

model was then sliced with certain thickness of 100 μm to form a series of 2D photos for further modeling. The direct image lithography process was performed on a commercial 3D printer. The 3D printer possesses a bottom-up projecting system with a digital mirror device with a UV light of 405 nm. At the light intensity of 1.6 mW/cm^2, the exposure time for bottom is 200 ms each layer (10 layers totally), and 400-800 ms for microcones (100 layers totally) to obtain the microstructures with different heights. The overall modeling process only takes 2-3 min, which shortens the fabrication time dramatically. Subsequently, isopropanol was used to remove uncured resin and then the PU layer was further cured under 120 ºC for 8 h to improve the mechanical property. After cooling down naturally, the PU layer with microcones was obtained.

F-PU layer was obtained by treating the PU layer with FOTS vapor. The detailed process was described as follows: the PU layer was firstly blown with N_2 to remove the dust and subsequently exposed to O_2 plasma for 3 min at 300 W with a flow rate of 30 sccm. In a glovebox filled with N_2, the PU layer with plasma treated (O-PU) was adhered on the cover of weighing bottle and 100 μL FOTS (4 μL·cm $^{-2}$) was added into it. And the FOTS layer formed on the surface of O-PU layer by heating up to 150°C for 2 h.

The TENG device was obtained by assembling the PU layer and F-PU layer as triboelectric layers. The clean PET plates (50 mm × 50 mm × 2 mm) were used as the supporting substrates. Then, the PU and F-PU layers were attached on the substrates with conductive Ni fabric as the electrodes. Cu wires were used as the wires for electric measurements. For the immersed F-PU layer, the same O_2 plasma process was taken

and then the sample was immersed in a commercial 3 M FC-3283 perflurocarbon liquid for 12 h.

3.3.2 Electrical measurement

The short-circuit current and transferred charges were measured using a low-noise voltage preamplifier. Before the electric measurement, two rectangle acrylic plates with the dimension of 80 mm × 80 mm were fixed on the end of the force gauge and the linear motor, respectively. The TENG device was stuck onto the acrylic plate on the force gauge by a double-side adhesive tape. For the electric measurement, the linear motor was set to impact the TENG device at the rate of 10 mm s^{-1}. Through adjusting the location of linear motor, the applied forces can be regulated. The configuration of electric measurement is shown in Fig. 3.1.

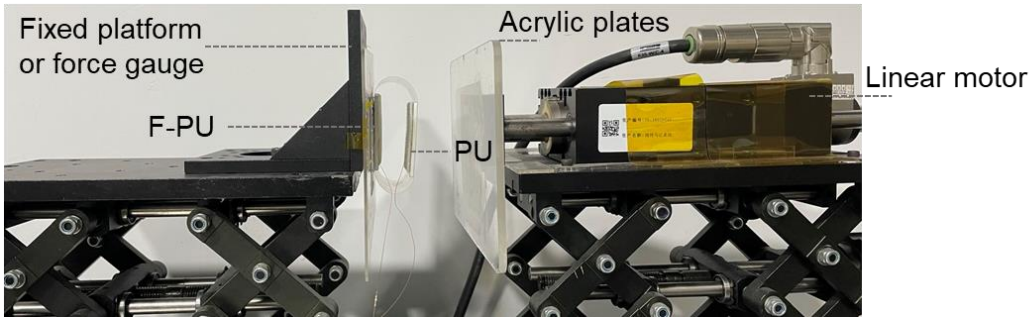

Fig. 3.1 Electric measurement configuration.

The 3D visualization photograph of the PU layer was scanned by a surface profiler. For the characterization of PU and F-PU layers, various measurements are carried out. The surface morphological of samples were recorded by SEM. FT-IR analysis was measured to evaluate the presence of some functional groups, which was tested in the region from 500 to 4000 cm^{-1} at a resolution of 1 cm^{-1}.

3.4 Characterization of TENG device

The fabrication process of the TENG composed of PU and F-PU layers with microcones on both surfaces is illustrated in Fig. 3.2. First, the PU layer was fabricated by a commercial 3D printer with an UV light wavelength of 405 nm based on the digital mirror device arrays[120] within several minutes. Second, the oxygen plasma treatment was utilized to introduce the -OH groups on the surface of PU layer and then the O-PU layer was prepared. Third, after the moist FOTS vapor covalently bonded with the -OH groups, the O-PU layer turned into the F-PU layer. Finally, the conductive fabric was pasted on both back surfaces of the PU and F-PU layer, respectively. Each side was fixed on PET substrate and then a complete TENG was fabricated, as shown in the schematic diagram.

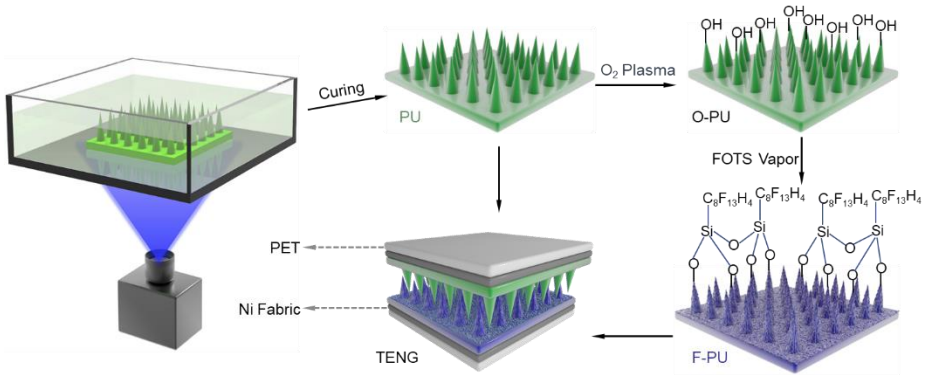

Fig. 3.2 The fabrication procedure of the TENG device composed of PU and F-PU layer.

The photos of the PU and F-PU layer can be found in Fig. 3.3. The PU layer is flexible and nearly transparent. Numerous microcones distribute on the PU surface uniformly. After fluorination, the F-PU layer turns pale yellow, but it possesses the same excellent flexibility as the PU layer, which can be seen from the photographs in Fig. 3.3b. Also, the microcones on the surface still keep the original state without obvious distortion.

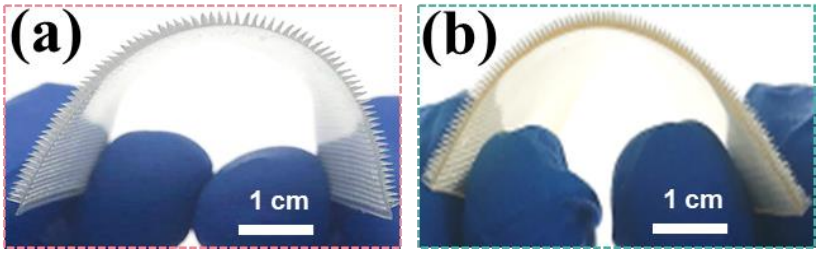

Fig. 3.3 Optical photos of (a) PU layer and (b) F-PU layer.

To further observe the microstructures of the PU surface, SEM was carried out from different view and the images were displayed in Fig. 3.4. It is clear that the microcone arrays are uniformly distributed on the surface of the PU layer. The boundary of every microcone is clear without any adhesion, implying the high printing precision. The diameter of the microcone is nearly close to 300 μm, which is consistent with the designed diameter.

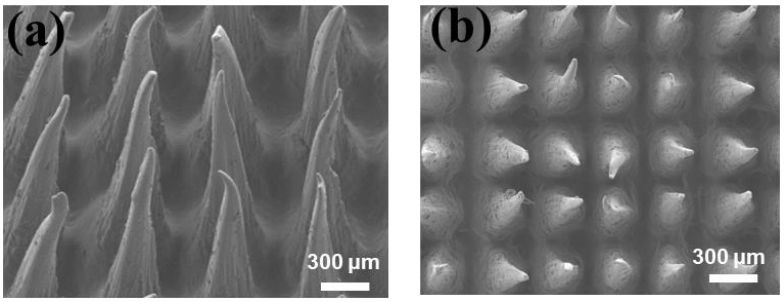

Fig. 3.4 SEM images of PU layer from (a) tilt and (b) top view.

Moreover, the 3D visualization photograph and height profile were scanned as shown in Fig. 3.5.

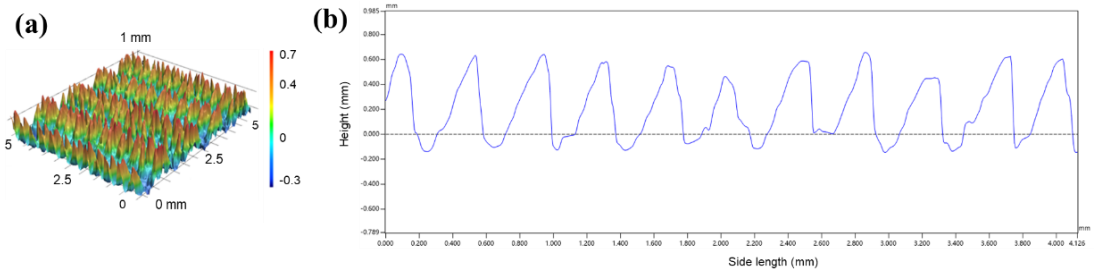

Fig. 3.5 (a) 3D visualization photograph and (b) height profile of the PU layer.

The microcones have the same height of 800 μm. The diameters and heights between microcones exhibit high consistency. The distance between the two peaks according to the height profile is about 400 μm, indicating the space between the microcones is about 100 μm. These results are also consistent with the SEM images.

To study the functional groups of PU and F-PU layers, FT-IR were measured as shown in Fig. 3.6. For original PU layer, the adsorption peaks at 1712 cm^{-1} and 1103 cm^{-1} can be attributed to the C=O and C-N[121]. After FOTS treatment, we can see that more complicated peaks appear at 700~1200 cm^{-1} except for the C=O and C-N in PU. The small peaks at 1065 cm^{-1} and 802 cm^{-1} are assigned to ν_{as} and ν_{s} Si-O-Si stretching.[122] While the peak at 1179 cm^{-1} and 898 cm^{-1} are associated with the ν_{s} and ν_{as} C-F stretching.[123] Thus, these results indicate that the fluorine was introduced on the surface of the PU layer successfully.

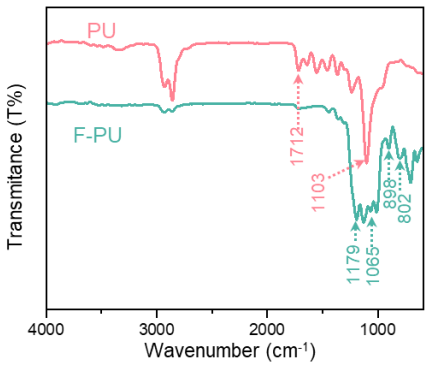

Fig. 3.6 FT-IR spectra comparison of PU and F-PU.

When the two triboelectric layers (the PU and F-PU layer) fully contact, the microcones of both layers are closely interspersed with each other to enhance the contact electrification area, which is illustrated in the enlarged SEM image in Fig. 3.7a. The two friction layers can separate easily due to their favorable elasticity when the external

forces are removed as shown in Fig. 3.7b. And The height of the microcones is ~800 μm according to the SEM images and the distance between microcones is ~100 μm, which is consistent with the height of the designed model.

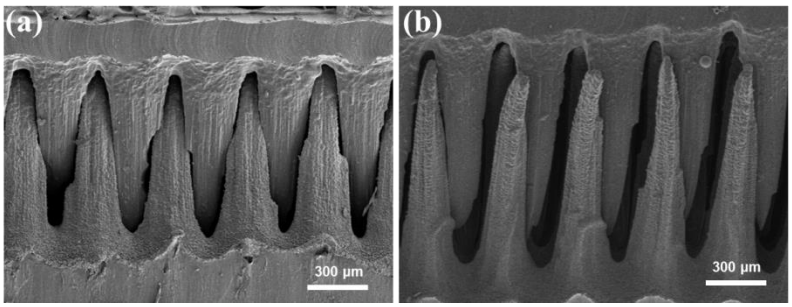

Fig. 3.7 PU and F-PU under (a) contact and (b)separate state.

3.5 Electric outputs of TENG

The working principle of the TENG composed of two dielectric layers under contact-separation mode can be explained with surface state model.[6] As illustrated in Fig. 3.8, the two triboelectric layers are fully contacted at the initial state (stage I). Considering the differences of valance band and conduction band structures of the two layers, the energy of occupied surface states in F-PU is lower than that of PU. Thus, the electrons transfer from the PU layer to F-PU layer and then the equivalent positive and negative charges generate on two surfaces of PU and F-PU layers, respectively. At this stage, the TENG is in electrostatic equilibrium state and no electron flows through the external circuit. Once the two layers physically separate, the electrons driven by the potential difference flow from the bottom electrode to the top electrode (stage II). The electrons keep flowing until the two layers separate the maximum distance (stage III). Next, when the distance between the two layers decreases, the electrons flow back to reestablish the electrostatic balance (stage IV). In a reciprocating motion cycle, electrons flow back

and forth between the two electrodes and a pair of alternating current peak appears.

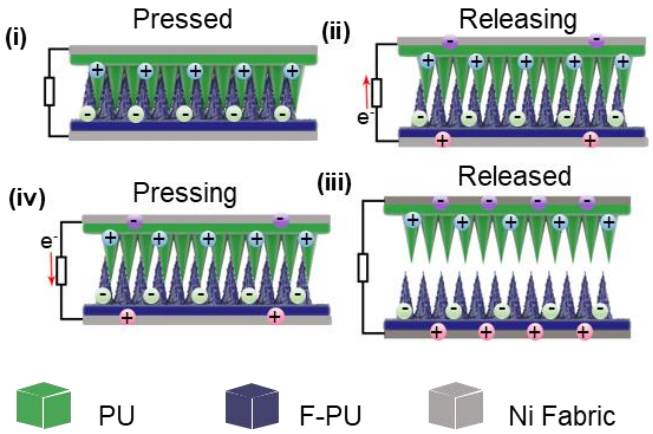

Fig. 3.8 The working mechanism of TENG composed of PU and F-PU layer under contact-separation mode.

During the electric output measurement of the TENG, the influence of the external force was evaluated, which is exhibited in Fig. 3.9. The dimension of the TENG is 50 mm × 50 mm, with the microcones of density of 125, height of 1000 μm. The density means the numbers of microcones along with the length of side. For example, density of 125 represents there are 125 × 125 microcones on the TENG device of 50 mm × 50 mm (25 microcones per millimeter). TENG with these parameters are used in the following measurement except for special mention.

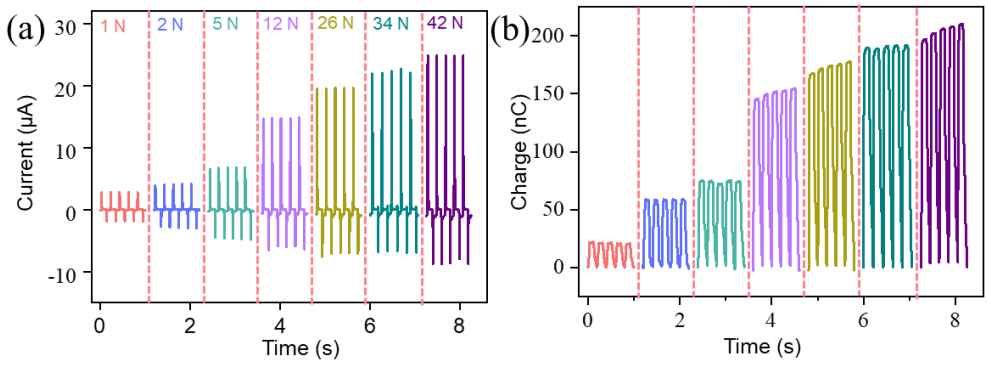

Fig. 3.9 Electric outputs of TENG under different external forces. (a) Short-circuit current outputs; (b) Transferred charges.

The force dependent current outputs increase from 3.1 μA to 25.2 μA with the applied

force changes from 1 N to 42 N and transferred charges increase from 24 nC to 211 nC. The output only shows marginal enhancement after the certain applied force (34 N) due to the effective contact area reaches to a plateau. Thus, the applied force was fixed at 34 N all through the following electric output measurement except for special mention to reduce the mechanical damage of the friction layers.

To investigate the influence of microcones fabricated by DIL technology on the TENG's electric output, the TENG comprised of the flat PU and F-PU layers without microcones was also fabricated by the same method but with the 3D model of rectangle shape without microstructure. And the comparison of the short-circuit current and transferred charges are presented in Fig. 3.10. It can be obviously seen that the current output for TENG device with microstructure can achieve 22.4 μA, which is 5 times larger than the one with flat layers (3.4 μA only). And the transferred charges are 192 nC and 36 nC for TENG with and without microcones, respectively.

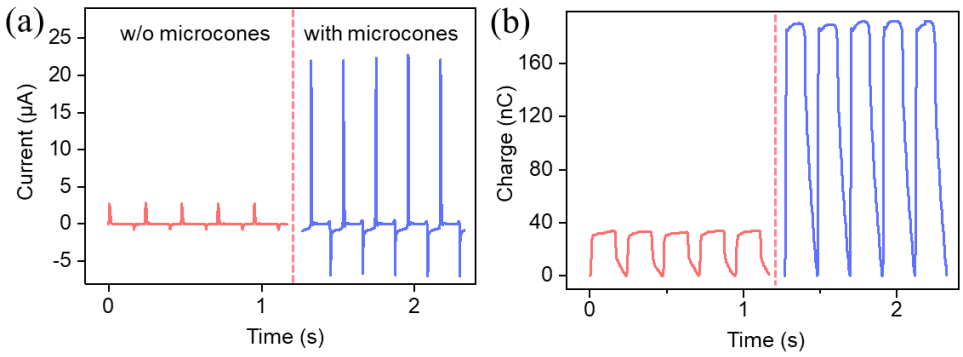

Fig. 3.10 Electric outputs comparison of TENG with/without microcones structure. (a)The short-circuit current; (b) The transferred charge.

Here, in order to optimize the electric output of the TENG, four major parameters including surface treatment method, TENG dimensions, and the density and height of

microcones were respectively investigated. It is noted that when one variable changes, the other three are fixed.

First, three types of TENGs with microcones suffering different surface treatments were fabricated. In addition to the device comprised of the PU and F-PU layers, the other two devices were made from two same PU layers, and PU/O-PU layers, respectively. The electric outputs comparison of the three devices shown in Fig. 3.11. The current outputs of original TENG, TENG with oxygen plasma treatment and TENG with FOTS treatment are 0.6 μA, 2.7 μA and 22.4 μA, revealing 4 times and 10 times improvement for each step. The corresponding transferred charges are 4.6 nC, 39.7 nC and 192 nC, suggesting the significant influence of FOTS modification on the improvement of electric outputs. The origins of the enhancement after fluorination will be discussed in detail below.

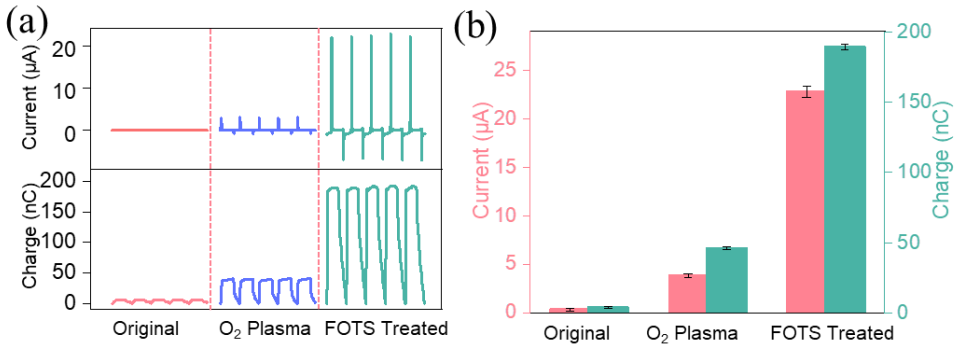

Fig. 3.11 Electric outputs curves (a) and Electric output comparison (b) of TENG with different surface treatment process.

As the FOTS vapor treatment plays a prominent role in the improvement of electric outputs, the detailed processing parameters including the temperature, time, and the amount of FOTS were investigated to verify the optimized treatment condition. In Fig.

3. 12a and 12b, the processing time was fixed at 120 min along with 100 µL FOTS for all the samples. The current outputs escalate from 4.2 µA to 22 µA when the processing temperature increases from 90◦C to 150◦C, and the transferred charges increase from 38 nC to 192 nC. That may be attributed to the full evaporation of FOTS. Then the electric outputs deteriorate dramatically when the temperatures continue to rise to 180°C. The PU layers become sticky after treatment under 180°C attributed to the structural damage of PU, resulting in the decrease of electric outputs.

Similarly, as shown in Fig. 3.12c and 12d, the electric outputs increase when the processing time changes from 30 min to 120 min and then decrease dramatically due to the excessive treatment. Superfluous FOTS can also lead to the crispy of the microcones and the decrease of the corresponding electric outputs as shown in Fig. 3.12e and 12f. In summary, the optimized processing condition for FOTS vapor treatment is at 150◦C for 120 min with 100 µL FOTS.

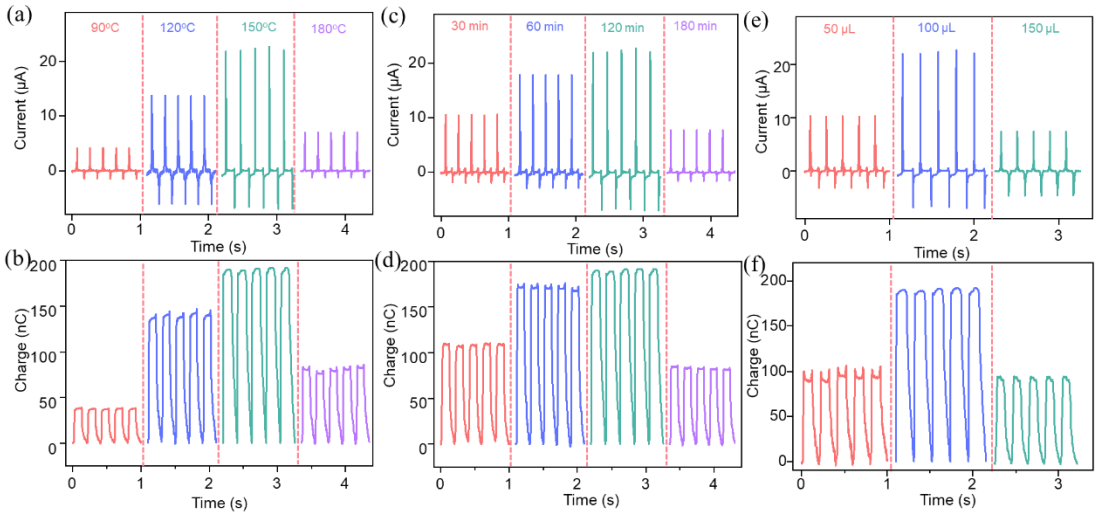

Fig. 3.12 Electric output comparison of TENG with FOTS treatment for (a, b) different treatment temperature; (c, d) different treatment time and (e, f) different amounts of FOTS.

Then, the influence of dimensions on the electric outputs of TENG device was carried out and the corresponding electric outputs can be found in Fig. 3.13a and electric output comparison are displayed in Fig. 3.13b. The parameters of the TENG used in this measurement are with dimension of 20 mm × 20 mm, 30 mm × 30 mm, 40 mm × 40 mm and 50 mm × 50 mm, respectively. The microcones on the surfaces possess the height of 1000 μm and the density is 20 microcones per millimeter. The short-circuit current and transferred charge of TENG with 4 cm^2 are 4 μA, and 48 nC, respectively. When the working area increases to 25 cm^2, the short-circuit current and transferred charge increase to 18.6 μA, and 178 nC, respectively. This is because that the contact area increases with the dimension of the device.

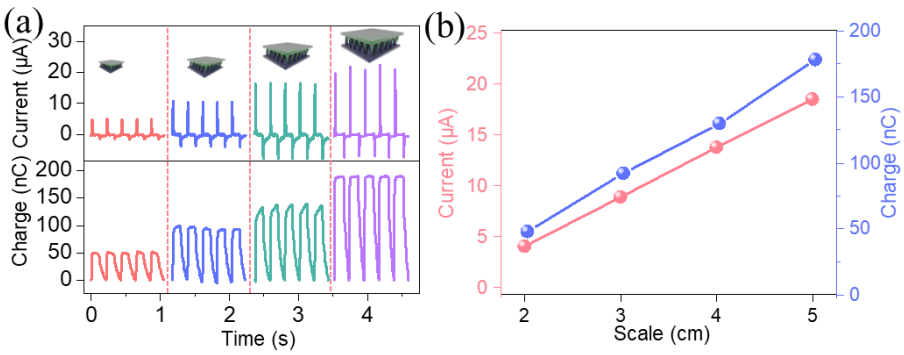

Fig. 3.13 Electric output curves (a) and comparison (b) of TENG with different dimensions including short-circuit current and transferred charges.

Noticeably, the electrical outputs show nearly linear relationship with the length of side as illustrated in Fig. 3.13b, which is associated with the increased contact surface are, indicating larger outputs can be achieved by enlarging the dimension of TENG devices. Finally, the density and height of the microcones also have great effect on the electric output of the TENG. As shown in the optical microscope images displayed in Fig. 3.14,

9 different devices with the same dimension of 5 × 5 cm^2 were fabricated.

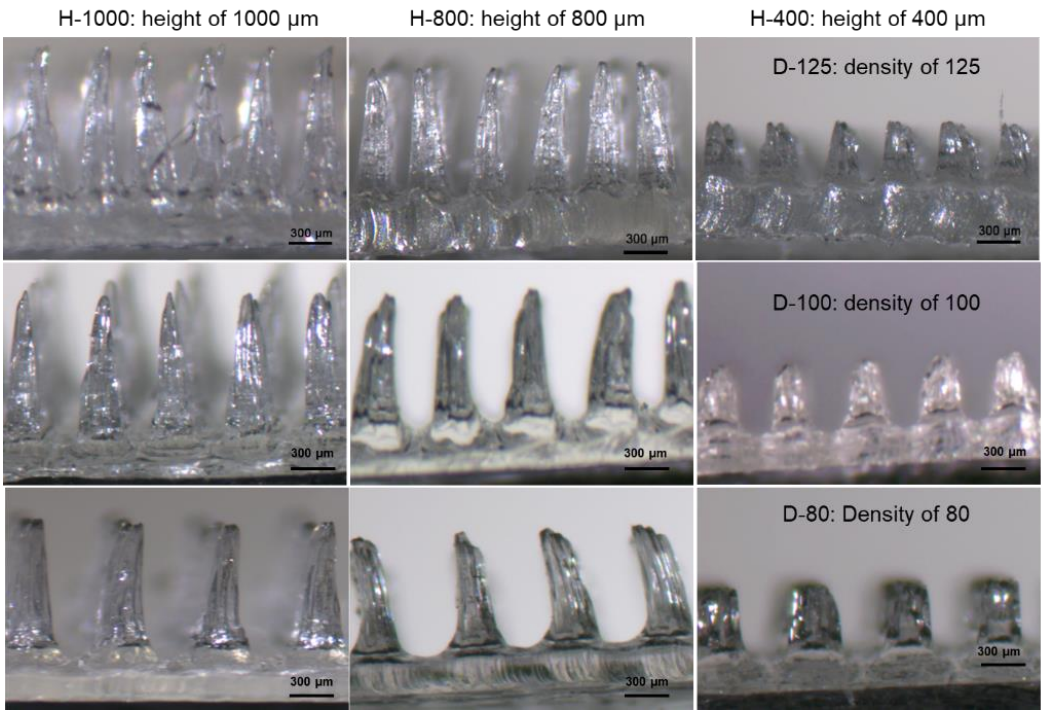

Fig. 3.14 Microscope images of the microcones with different height and density.

Various density of 125, 100 and 80 were fabricated through changing the printing models. Different heights of 1000 μm, 800 μm and 400 μm were obtained by regulating the exposure time.

And the corresponding electric output comparisons are presented in Fig. 3.15. It can be obtained that when the density fixed at 80, the current and transferred charge increase from 4.5 μA, 57 nC to 15.6 μA, 144 nC with the height of microcones increasing from 400 μm to 1000 μm.

Next, with the certain height of 1000 μm, the electric outputs can even reach to 22 μA and 190 nC when the density is 125. The electric outputs show positive correlation with the height and density of microcones owing to the increase of effective contact area.

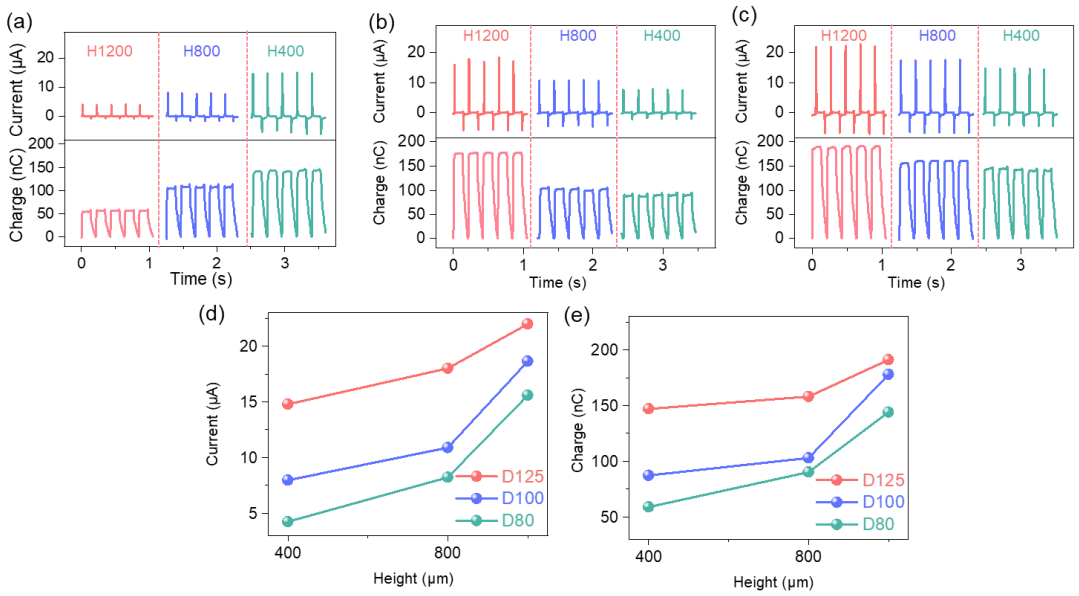

Fig. 3.15 Short-circuit current and transferred charge of the TENG: (a) D-80 with different heights; (b) D-100 with different height; (c) D-125 with different height. Influence of height and density on the electric output of TENG: (d) short current. (e) transferred charge.

However, when the height of the microcones exceeds 1000 μm, the top of microcones will tilt and stick together during the thermal curing process as shown in Fig. 3.16a. And this will reduce the contact area and then result in the decrease of electric output. The electric outputs of the TENG with ultralong microcones (5 × 5 cm^2 in size, density of 125) only reveal a current of 7.2 μA with the transferred charge of 80 nC, which are displayed in Fig. 3.16b.

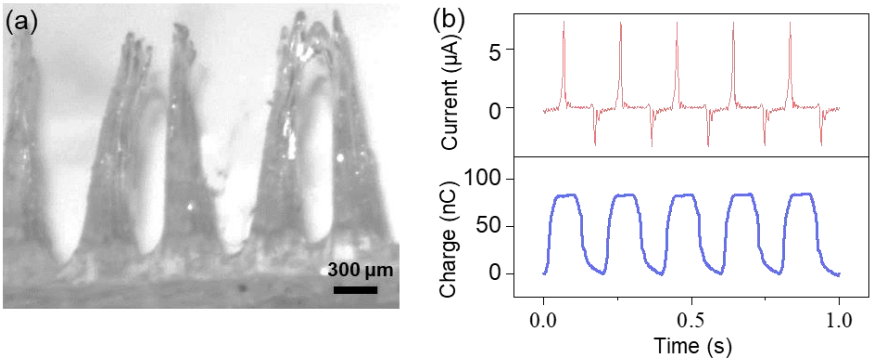

Fig. 3.16 (a) Microscopy image of the ultralong microcones and (b) corresponding electric outputs.

It is of great importance to investigate the electric output of TENG with different external loads for powering small electronics in daily life. Different resistors were connected in series with the TENG to measure the effective power density, which is calculated based on the load resistance and the current.

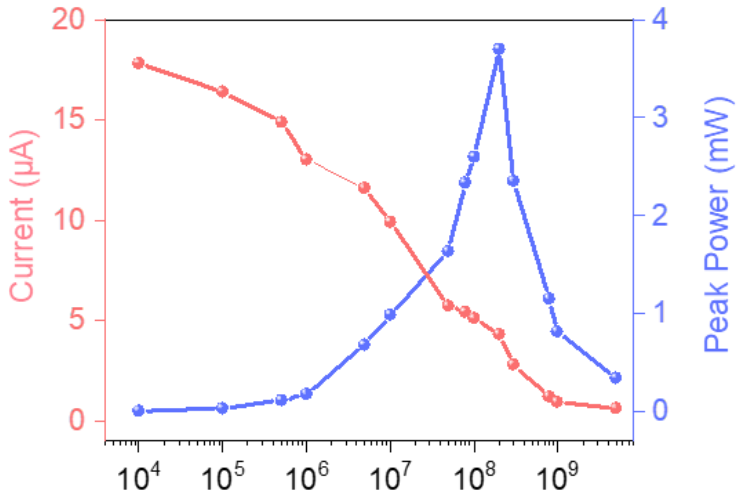

Fig. 3.17 Load resistance matching test of the TENG.

As shown in Fig. 3.17, with the increase of external resistance, the current decreases and the maximum power density can reach to 1.5 W/m^2 at the external load of 200 MΩ, which is equivalent with the internal resistance of the TENG. Thus, the TENG device can be regarded as a current source with large enough internal resistance when connected with the external resistance significantly smaller than its internal resistance. Furthermore, the long-term stability of TENG (5 × 5 cm^2 in size, density of 125, height of 1000 μm) was also measured to verify the possibility for practical application. During the 10,000 experimental cycles at 1 Hz, the current keeps stable, and the durability also can be confirmed by the similar outputs of the first and the last cycles as shown in the inset of Fig. 3.18.

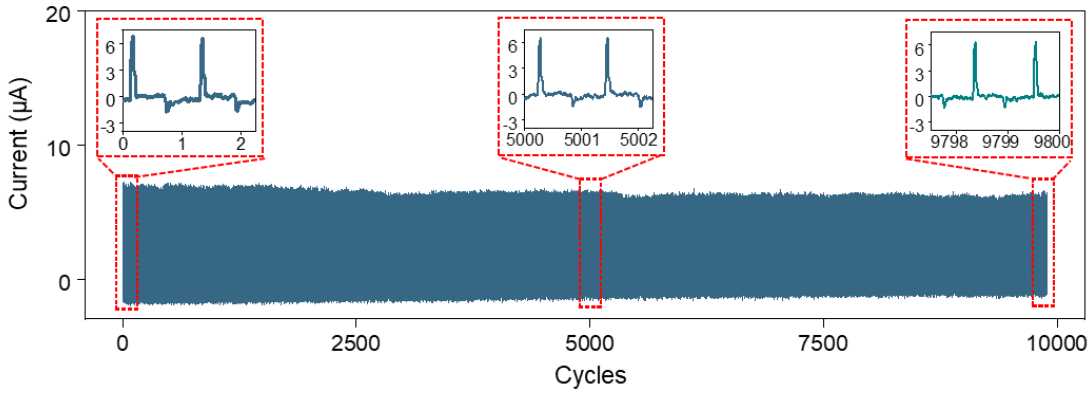

Fig. 3.18 Cycling stability of the TENG at the frequency of 1 Hz with the applied force of 5 N.

Above all, the TENG with surface microstructures was successfully fabricated by DIL technology. Subsequent FOTS vapor treatment plays a prominent role in the enhance electric outputs. The detailed parameters for FOTS vapor treatment such as temperature, time and amount are studied systemically to determine the optimal treatment condition. The influence of dimension of TENG device, height and density of microcones on the electric outputs are also investigated.

The electric output characteristics of the other TENGs with microstructure fabricated through various methods were compared as displayed in Table 3.2. The TENG fabricated by DIL method has the microcones structure with large length and small diameters, thus TENG in this work exhibits comparative short-circuit current related to the surface charge density and effective contact area, commendable power density, and excellent cycling stability. Moreover, DIL method can print products with different sizes and shapes by just changing the printing models, so the TENG in this work shows excellent flexibility and customization. The efficient manufacturing process, ultrafast molding speed and low cost enable its potential application for portable self-powered electronic devices in future.

Table 3.2. Comparison of TENG performance with microstructures fabricated through various method.

Method	Triboelectric materials	Microstructure	Model	Electrode Area(cm^2)	Current (μA)	Power Density (W/m^2)	Durable Test (cycles)	Ref
Fused deposition modeling	Poly(glycerol sebacate) and CNTs	Porous	SE	3*3	7.69	0.056	2000	[78]
Photolithography	PDMS and nylon fabric	Oblique rod arrays	CS	4*4	51.8	2.12	12000	[124]
Vacuum filtration	Bacterial cellulose-$BaTiO_3$ and PDMS	Embossed structure	CS	3.6*3.6	21	4.8	3000	[125]
Femtosecond laser direct writing	PDMS and Cu	Micro/nano cone	CS	0.8*0.8	2.6	0.21	28000	[79]
Direct ink writing	Silicone rubber and Al	Ridges and dents	CS	3*3	18.7	0.61	200	[126]
Salt template	PDMS and Cu	Porous	CS	3.7*3.7	2.26	0.89	10000	[127]
Digital light processing	ABS and PTFE	Biomimetic villus structure	CS	Cylinder diameter: 4.2 cm height: 3.8	0.4	0.0014	10000	[128]
Fused deposition modeling	PA/PEG and PE/PDMS	Sponge like	CS	12*10	--	0.07	--	[129]
AAO template	Fluorinated PP and Cu	Nanowires	CS	4*4	3.04	--	37000	[113]
Direct image lithography	Fluorinated PU and PU	Microcones	CS	5*5	22	1.3	10000	this work

3.6 Conclusion

In summary, the PU layers with surface microcones have been fabricated by an efficient DIL method for its high precision and fast molding speed (within 3 minutes). F-PU layer was obtained by chemically modified of FOTS vapor on the PU layer. The TENG based on the PU and F-PU layer with microcones structures show 400% enhancement on electric outputs compared with TENG with flat surface. By comparing the electric outputs of TENG under various treatment processes, we can conclude that the FOTS vapor treatment play the prominent role in the improvement of electric outputs. The temperature, time and amount of FOTS treatment are studied symmetrically to determine the optimal processing condition. The dimension of devices, the height and density of microcones also have influence on the electric outputs. The optimal TENG device can achieve a current of 22 μA with the transferred charges of 192 nC. The device can obtain a maximum output power density of 1.5 W/m^2 at an external resistance of 200 MΩ. The device also shows brilliant cycling stability for over 10000 cycles. The advanced manufacturing technology and excellent electric performance indicate its potential application for portable self-powered electronic devices in future.

Chapter 4 Origin and application of the high-performance TENG device

4.1 Introduction

In this chapter, we will first investigate the origin of the enhanced electric outputs of the TENG based on DIL technology by the surface morphologies observation and elemental analysis. Due to the wide area preparation capabilities and the customizability of DIL technology, the TENG can be rapid fabricated into different shapes to harvest various biomechanical energy. Finally, the TENG used as an advanced energy supply was used to provide electricity for self-powered sterilization.

4.2 Materials and equipment

4.2.1 Materials

Cu foam (purity ≥ 99.9%, thickness of 1 mm) was bought from Suzhou Taili metal foam factory. Hydrochloric acid (HCl), Sodium hydroxide (NaOH), and Ammonium persulfate ($(NH_4)_2S_2O_8$) were purchased from Aladdin-Sigma. Escherichia coli (E. coli), Staphylococcus aureus (S. aureus), Candida albicans (C. albicans), sterile tryptone soybean broth (TSB) medium, and phosphate buffer saline (PBS) were purchase from Beijing Biology co.

4.2.2 Equipment

Table 4.1 The equipment for application of TENG device

Equipment	Model	Producers
X-ray diffraction	SmartLab 3KW	Rigaku co.
Vacuum oven	DZF-6-5-	Yiheng, China
ICP-OES	ICPE-9820	Shimadzu
X-ray photoelectron spectroscopy	ESCALAB 250	Thermofisher Scientific

4.3 Methodology

4.3.1 Fabrication of TENG devices with various shapes

TENG devices with rectangle shape and insole shape were fabricated with the same method as described in the device fabrication part in chapter 3. For the fabrication of insole-shape TENG, PDMS was firstly used to obtain an insole-shaped template with the thickness of 5mm by using acrylic plate with the thickness of 5 mm as the template. Then PU was poured into rectangle tank with the PDMS template in it. After curing, the PU shell was obtained. The PU and F-PU layer were sticked on the bottom of PU shell with conductive tapes on it and then encapsulated them together. The space between the two friction layers is about 5 mm.

4.3.2. Fabrication of Cu_2O Nanowires Electrode

The Cu_2O nanowires electrode was fabricated based on a copper foam with the mesh size of 200 μm due to its excellent electrical conductivity, satisfactory surface area and relative low cost. Copper foams (1 cm ×1 cm) were immersed in HCl (1.0 M) for 5 min to remove the surface oxide layer and ultrasonically washed with acetone, ethanol and deionized water successionally. Cu_2O nanowires were grown on copper foams through in-situ chemical oxidation. 4.8 g NaOH solved in 12 mL deionized water was mixed with the solution of $(NH_4)_2S_2O_8$ (1.368 g) solved in 6 mL deionized water. After another 27 mL deionized water added into the solution, Cu foam was immersed in it for 40 min and then annealed in vacuum at 180 °C for 3 h. The as-obtained Cu_2O was characterized with SEM and XRD.

4.3.3. Antibacterial/Antifungal performance of Cu_2O electrode with TENG system

E. coli of Gram-negative, S. aureus of Gram-positive bacteria and C. albicans were cultured to measure the antibacterial/antifungal properties of Cu_2O electrode with TENG system. The fresh bacterial/fungal suspension was acquired through culturing E. coli, S. aureus and C. albicans in sterile TSB medium at 37 °C for 12 h, where the bacterial/fungal were in the stationary state. Subsequently, the concentration of bacterial/fungal suspension was measured using counter method under the microscope. The blood cell counter was used for counting. The bacteria suspension was placed in the counting chamber of the blood cell counter (with a certain volume of 0.1 mm^3). By counting the number of bacteria in the chamber, the concentration of the bacteria suspension can be calculated. Then the bacteria suspension was diluted using sterilizing PBS to get an initial culture concentration of ~10^6 CFU/mL. Thereafter, 1 mL E. coli/S. aureus/C. albicans solution was pipetted from the suspension incubated overnight into a petri dish containing 9 mL fresh TSB (blank sample), 9 mL TSB and Cu_2O electrode for contrast, 9 mL TSB and Cu_2O electrode connected with TENG through a rectifier bridge. The mixture was then cultured at 37 °C for another 6 h, 9 h and 12 h to measure the long-term antibacterial/antifungal property. The concentration of E. coli/S. aureus/ C. albicans was obtained by spread plate method. And the antibacterial/antifungal efficiency is calculated by:

$$Sterilization\ Efficiency = \frac{CFU_0 - CFU}{CFU_0} \qquad (4.1)$$

Where CFU_0 is concentration of blank sample, CFU is the concentration of contrast sample and experimental sample.

4.4 Origin of the enhanced electric outputs

Based on the above obtained experimental results and the fundamental mechanism of contact triboelectrification, the enhanced output mainly origins from the improved charge density (charge per unit apparent surface area) on triboelectric layer, which is

associated with the surface morphology and chemical composition.[109] In addition to the increased surface charge density based on the microcones fabricated by DIL, the following FOTS treatment can also change the physical morphology in micro-nanoscale as well as the chemical composition on the microcones. Thus, a possible explanation of the output enhancement is proposed as below.

First, the surface morphologies of the PU, O-PU and F-PU layers were obtained using SEM, respectively, as shown in Fig. 4.1. The original PU surface is smooth and flat, while the surface appears a mild rough with some striola after treated with O_2 plasma. While after the O-PU layer reacted with the FOTS vapor, large amounts of bumps and scratches with average size of dozens of micrometers formed on the surface of the microcones, which is favorable for the improvement of TENG's electric outputs. Thus, we can conclude that the surface microcones and the roughened surface morphology in micro-nanoscale on the microcones after FOTS treatment leads to the partly enhanced electric outputs.

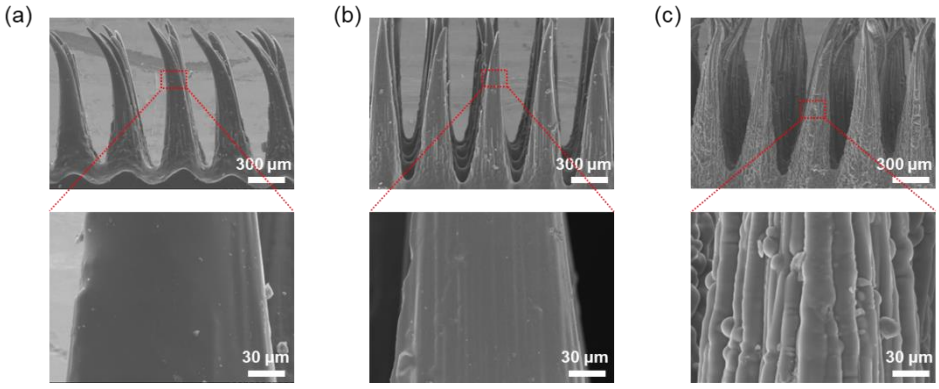

Fig. 4.1 SEM images of (a) PU;(b) O-Pu and (c) F-PU.

Second, the surface chemical composition and valence states were analyzed by XPS with Al Kα (1486.6 eV) as the X-ray source. In fact, the element mapping images from

EDS in Fig. 4.2 have already shown the existence of fluorine on the surface of the F-PU layer after the FOTS modification.

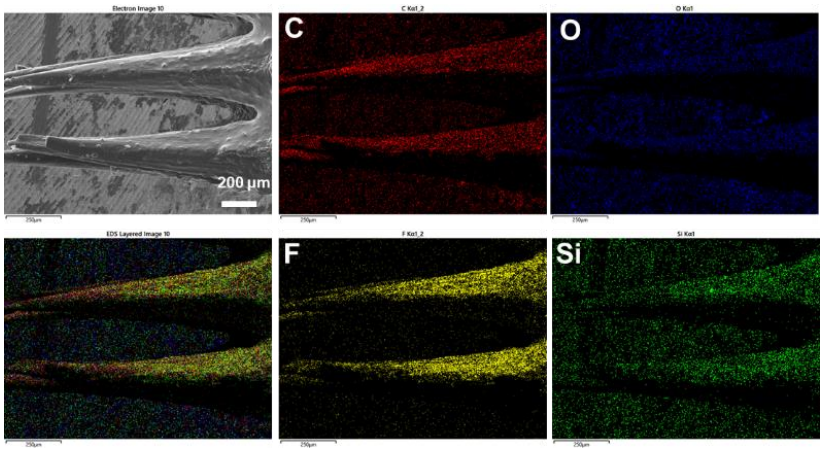

Fig. 4.2 Surface element mapping of the F-PU layer.

The survey spectrum of PU layer shown in Fig. 4.3a demonstrates the existence of C, O elements (with atom contents of 69.43% and 29.07%, as listed in Table 4.2), also with trace N element (1.50%). The high-resolution spectrum of representative C 1s exhibits four deconvoluted peaks, which can be attributed to the C-C (285.3 eV), C-OH (286.5 eV), and C=O-O (288.6 eV) species in PU, respectively (Fig. 4.3b).[130]

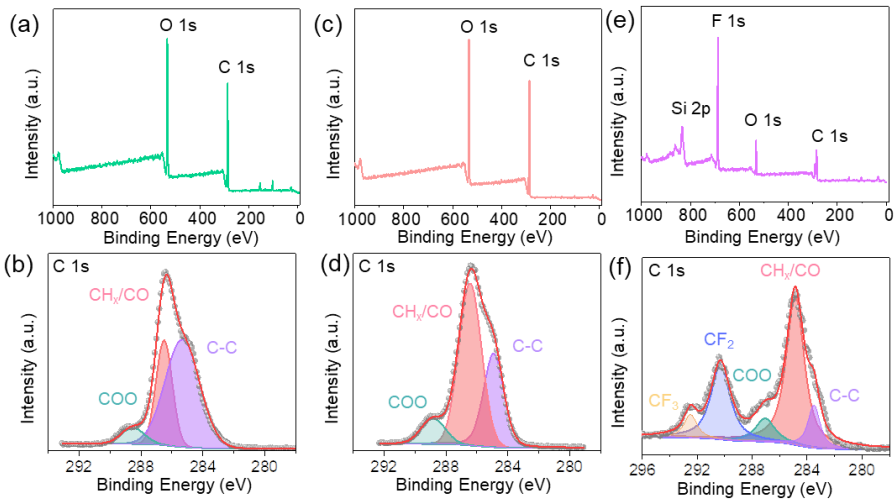

Fig. 4.3 XPS survey spectra and high-resolution C 1s spectra of (a, b) PU; (c, d) O-PU and (e, f) F-PU.

As shown in Fig. 4.3c, through the oxygen plasma treatment, C and O elements with trace N elements appear in the survey spectrum and detailed element contents can also be found in Table 4.2. The peak at 286.5 eV in high-resolution C 1s spectrum increased dramatically, revealing the formation of C-OH functional groups on the surface of PU (Fig. 4.3d).[131] And the -OH groups on the surface providing the covalent bonding sites with FOTS molecules.

Table 4.2 Elements contents of PU, O-PU and F-PU layers

Samples / Elements	PU	O-PU	F-PU
C 1s	69.43	67.46	45
N 1s	1.50	0.84	1.46
O 1s	29.07	31.7	14.17
F 1s	--	--	**34.7**
Si 2p	--	--	4.67

After the FOTS modification, large amounts of F and Si elements appear as shown in Fig. 4.3e. The C 1s spectrum shows much complicated peaks and can be decomposed into two kinds of peaks, which is presented in Fig. 4.3f. Three peaks locate before 290.0 eV, which are identical with O-PU. The new peaks appeared at 290.3 and 292.5 eV can be assigned with $-CF_2$ and $-CF_3$, respectively. The ratio of $-CF_2$ and $-CF_3$ calculated based on the fitted peak areas is ~4.78, which is nearly close to the theoretical stoichiometric $-CF_2/-CF_3$ ratio of 5 in the molecular structure of FOTS[132, 133].

Except for the peak at 532.5 eV, the O1s spectrum in Fig. 4.4a of F-PU can also be

decomposed a peak at 533.8 eV, indicating the existence of Si-O. The appearance of Si-O bonds suggests the -OH groups on the surface react with the $SiCl_3$ groups in FOTS molecules, resulting in the formation of Si-O covalent bonds.[61] In addition, the peak at 687.6 eV in F 1s spectrum (Fig. 4.4b) is associated with C-F. Based on the above analysis of the EDS and XPS results, the fluorination reaction took place on the PU layer during the FOTS vapor treatment process.

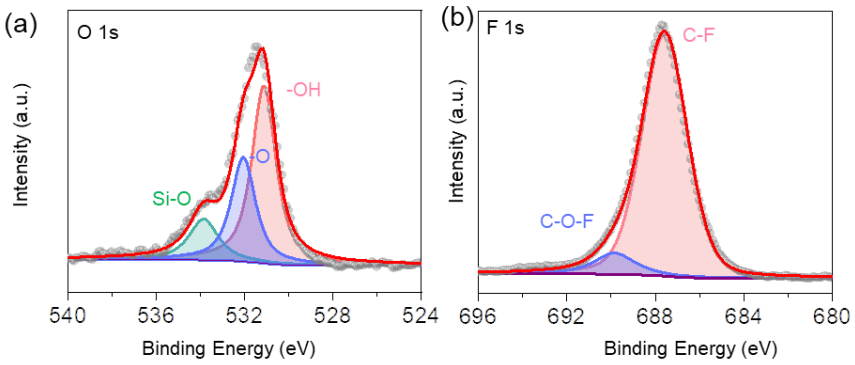

Fig. 4.4 High resolution XPS spectra of the F-PU layer. (a) O 1s; (b) F 1s.

From the surface morphology observation and chemical composition analysis, the enhanced electric output originates from the synergistic effect of microcones fabricated by DIL technology, fluorination and roughened surface morphology caused by the FOTS treatment. While in the previous literature, the enhancement of the electric performance after surface fluoridation was only contributed to the increase of the fluorine. Therefore, in order to further verify this synergistic effect, a control experiment using the commercial perfluorocarbon liquid (3M FC-3283) as the fluorinated reagent was also designed. The SEM images of the immerse-PU layer are shown in Fig. 4.5a and 4.5b. The surface still seems smooth and flat without microstructure after immersed in fluorine-containing liquids. The element mapping of

immersed F-PU shows the uniform dispersion of C, O, F as shown in Fig. 4.5c. And the introduction of F element can also be evidence by the XPS analysis as shown in Fig. 4.5d. Fig. 4.5e shows the element contents based on the XPS survey. After the PU layer immersed in the perfluorocarbon liquid, large amount of F elements (36.04%) distributes on the surface of immersed F-PU layer, which is comparable with the F-PU layer fabricated with FOTS vapor.

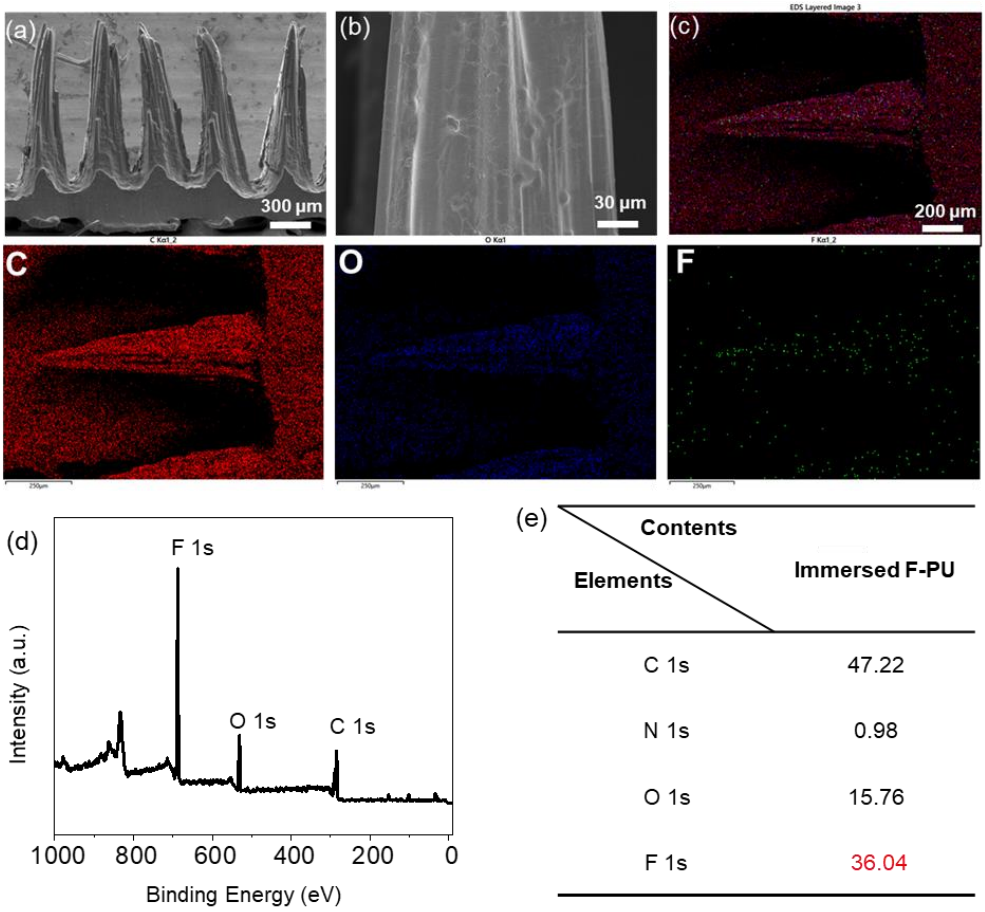

Fig. 4.5 (a, b) SEM images under different magnification; (c) Element mapping; (d) XPS spectrum and (e) Element contents of immersed F-PU.

While the TENG assembled with the immersed F-PU layer and PU layer only gets a current of 7 μA under the same test condition (Fig. 4.6a). Thus, even though the immersed layer almost has the same amount of fluorine on the surface as the FOTS

modified PU layer, the electric output is much lower than it. Thus, the surface microstructures as well as the fluorination plays a joint role in increasing the electric output of the TENG. It is also notably that the TENG with FOTS modification are more stable, and durable compared with the one with the immersed perfluorocarbon liquid treatment (Fig. 4.6b) due to the strong covalent bonds between PU and FOTS molecules.

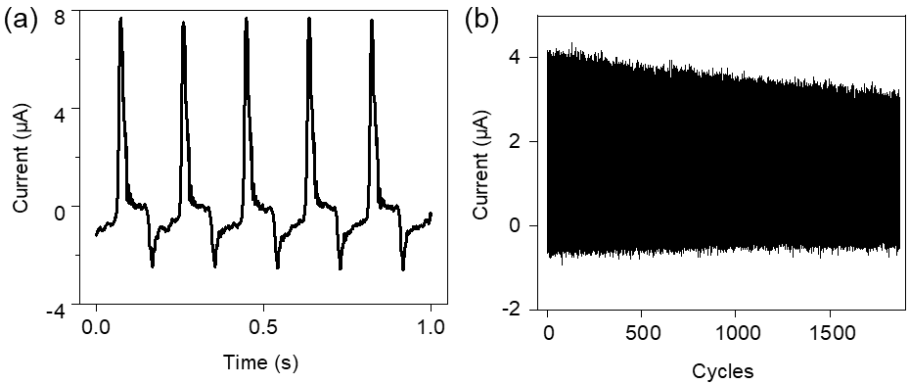

Fig. 4.6 (a) Short-circuit current and (b) cycling stability under 1 Hz of the TENG composed of the immersed F-PU layer and the PU layer.

4.5 Application of the high performance TENG

Based on the customizability of DIL method, the TENG can be fabricated into different shapes to harvest various kinds of mechanical energy. We fabricated a rectangle shape TENG device with the dimension of 3 × 8 cm^2 with the microcones density of 100.

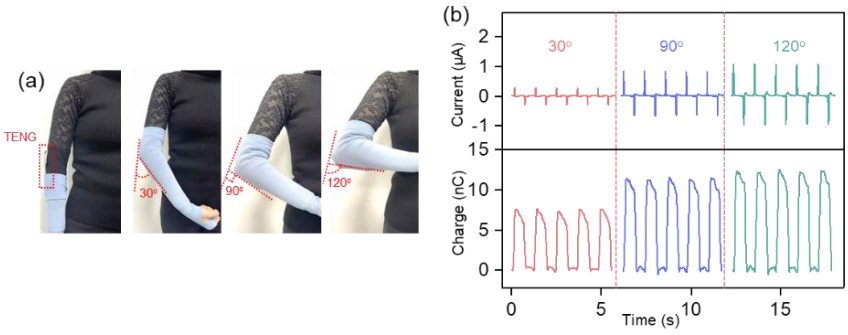

Fig. 4.7 (a) Photographs of the TENG embedded into sleeve. (b) Short-circuit current and transferred charge of the TENG under various bending angles.

Due to the excellent flexibility of PU, the TENG can be attached on the elbow within the clothes as shown in the photographs in Fig. 4.7a. When the arm was repeatedly bent,

the obtained electric output was recorded, as illustrated in Fig. 4.7b. The TENG device can generate obvious current outputs for various bending angles. Moreover, the electric output of TENG becomes larger as the bending angle increases from ~60^{o} to ~120^{o}, and the corresponding optical photos are shown in the insets in Fig. 4.7a. When the bending angle is ~120^{o}, the current output can reach to ~ 1 μA.

Because of the high modeling speed and low cost for large-scale fabrication of DIL technique, the insole shaped PU layers with the length of 20 cm can be obtained easily as shown in Fig. 4.8a and it can be twisted effortlessly (as shown in Fig. 4.8b). After FOTS treatment and encapsulation by the PU shell, an insole shaped TENG with excellent flexibility and conformability was fabricated as shown in Fig. 4.8c and the photos of the real device from different view are shown in Fig. 4.8d and 4.8e. It can be directly used as an insole in our shoes to harvest the biomechanical energy when we are moving.

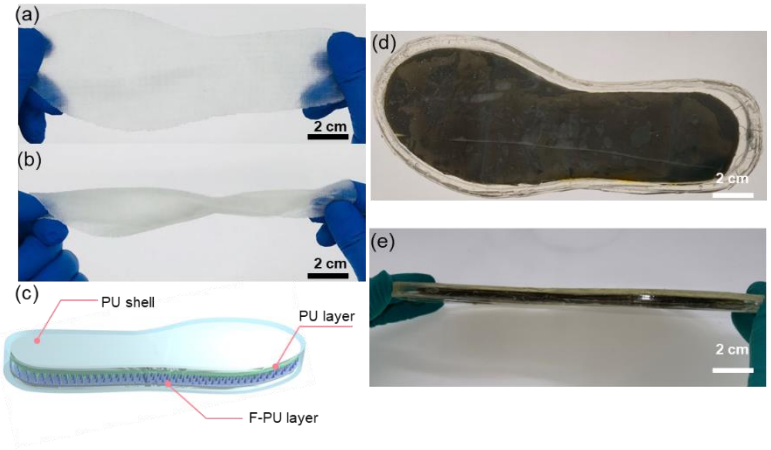

Fig. 4.8 Photographs of an insole shaped PU layer under (a) normal state and (b) twisting state. (c) Schematic diagram of an encapsulated insole shaped TENG; Photographs of the insole shaped TENG device from (d) top view and (e) lateral view.

Fig. 4.9 shows the corresponding currents under various motions of a human (~60 kg), including walking, marching, running, and jumping, when the insole shaped TENG placed within the shoes. It can be obviously seen that all motions can generate the

currents over 2 μA, and the current can even reach 8 μA when we are jumping, indicating its practical application for harvesting mechanical energy from our daily movements.

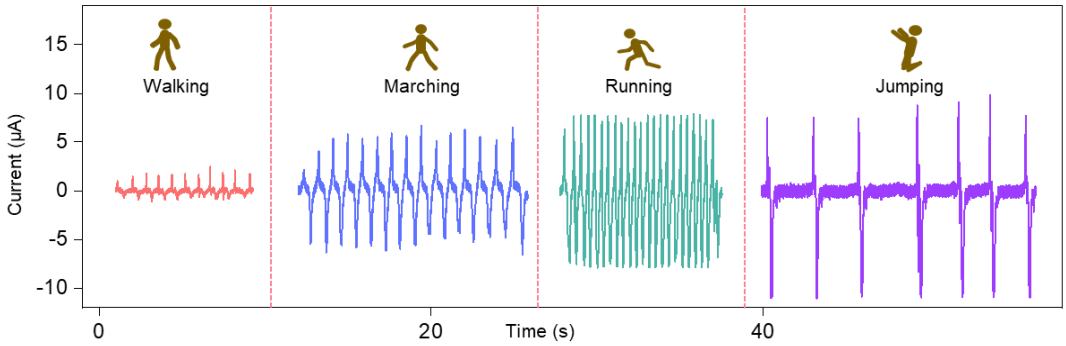

Fig. 4.9 Electric outputs of the insole shaped TENG when the wearer performs different motions

The generated electricity when we are walking can be used to charge capacitors for later use through an equivalent circuit as shown in Fig. 4.10a. TENG device can harvest mechanical energy from human motions and then transform them into AC electric outputs. The AC outputs can transform to DC outputs through the rectifier bridge and the DC outputs can be stored in the commercial capacitors directly. The charging curves for different capacitors are also represented in Fig. 4.10b. For a capacitor of 3.3 μF, the voltage can reach up to 10 V within 10 s, and a 47 μF capacitor can be charged to 10 V less than ~800 s.

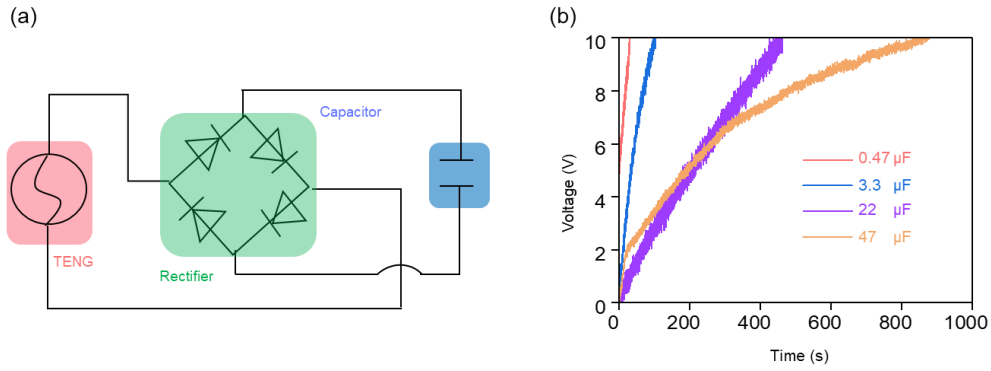

Fig. 4.10 (a) Circuit diagram of the TENG based the self-charging system. (b) The measured voltage of capacitors with different capacitance charged by the insole shaped TENG when walking.

Thus, this insole shaped TENG placed in the shoes shows great potential for powering the wearable electronics when we are walking. However, due to the commercial capacitor is rigid and with low capacity, it is inappropriate for the application of flexible electronics. Also, the low capacity make it need for frequent charging, which will dramatically shorten its lifetime.

Bacteria and fungi are ubiquitous and sometimes may cause infections and dissemination on skin or nails.[134] Recently, electrical antibacterial under direct current and alternating current have been proven efficient and convenient, in which the TENG has been regarded as the promising candidates for providing electricity.[135] The TENG based on the DIL technology exhibits compelling merits for devices with customizable shapes, scalable production, and excellent reproducibility of high electric output. So, in this study, we propose the strategy for antibacterial/antifungal application by using our TENG as the electricity supply. Furthermore, previous research shows that one-dimensional conductive nanowires with unique electric property can significantly enhance the electrical filed even by three to four orders of magnitude.[136]

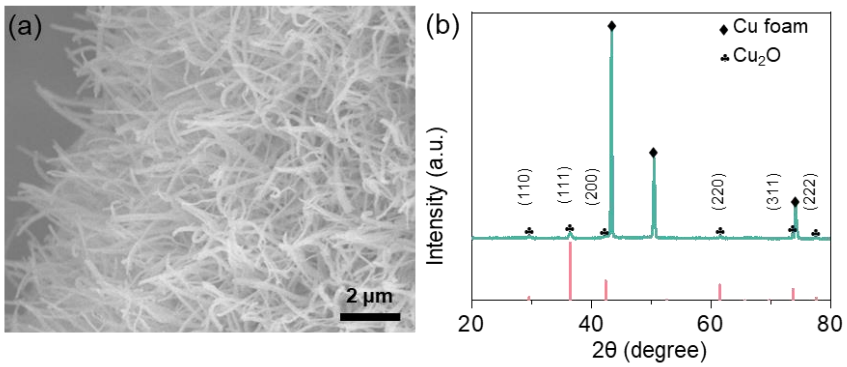

Fig. 4.11 (a) SEM image of Cu_2O nanowires. (b) XRD spectra of the as-prepared Cu_2O electrode

Cuprous oxide (Cu_2O) nanowires with the advantages of nontoxicity and low-cost shows excellent antibacterial properties and was prepared through in-situ chemical oxidation method based on the copper foam substrate.[137] As the SEM image

exhibited in Fig. 4.11a, the Cu_2O nanowires vertically grow on the skeleton of the Cu foam, with the diameter of about 200 nm and the length of dozens of micrometers. And the crystallinity structure of the Cu_2O is measured by XRD (in Fig. 4.11b). Except for three strong background peaks at 43.47°, 50.43° and 74.10° originating from the Cu foam, six well-defined diffraction peaks present at 29.56°, 36.42°, 42.30°, 61.34°, 73.53° and 77.32° index to the (110), (111), (200), (220), (311) and (222) crystalline planes of cuprite Cu_2O (JCPDS#77-0199).[138]

The as-prepared Cu_2O nanowires electrode was connected to the TENG with a dimension of 5 × 5 cm^2 directly for continuous alternating current supply as depicted in Fig. 4.12.

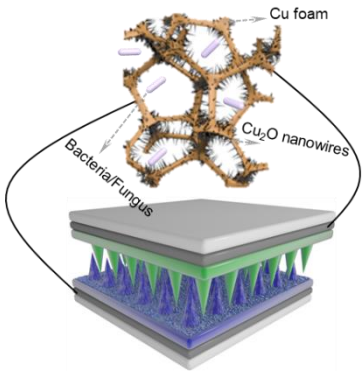

Fig. 4.12 Schematic diagram of sterilization system composed of TENG device and Cu_2O electrode.

Cu_2O nanowires electrode is used as the sterilization part to amplify the input current. TENG device is directly connected with the Cu_2O nanowires electrode without the assistance of rectify bridge. The Cu_2O nanowires electrode is immersed with the culture solution. Bacterial and fungal are around the Cu_2O nanowires during the experimental process. With the continuous electricity supply provided by TENG device, the growth and multiplication of bacterial and fungal are suppressed.

The antibacterial property of Cu_2O nanowires electrode with TENG against Gram-negative E. coli and Gram-positive S. aureus species bacteria were evaluated by

spreading the diluted bacterial suspension cultured with TSB. To verify the sterilization effect, two control experiments were also carried out using the Cu_2O nanowires without TENG and blank sample, respectively. The sterilization efficiency of both bacteria at different culture time in TSB for 6 h, 9 h and 12 h were obtained by three repeated experiments, which is shown in Fig. 4.13a and 4.13b.

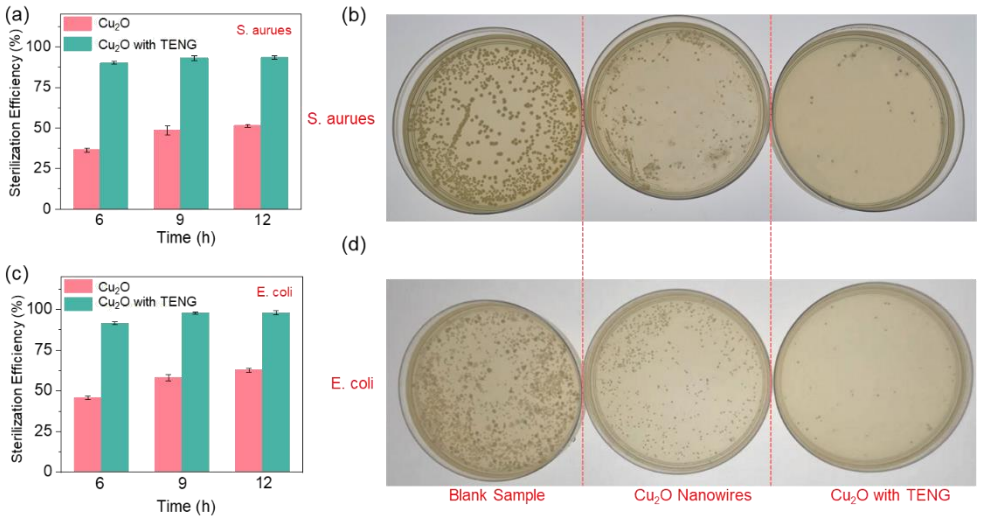

Fig. 4.13 Sterilization efficiency comparison of Cu_2O and Cu_2O with TENG systems of S.aureus (a) and E.coli (b). Corresponding photographs of colonies after culturing for 12 h, S.aureus (c) and E.coli (d).

It was found that the antibacterial efficiency under Cu_2O nanowires electrode with TENG is nearly 2 times higher than that of system with Cu_2O nanowires electrode only, implying significant enhancement through continuous electrical supply. For S. aureus, the sterilization efficiency can reach to 93.5% after culturing for 12 h, and for E. Coli, the value can reach to 98%. The higher sterilization efficiency for E. Coli can be attributed to the thicker peptidoglycan protection layer in Gram-positive bacteria cytoderm. The peptidoglycan layer exhibits intrinsic resistance to external stimuli. Therefore, the Gram-positive S. aureus species are more impregnable than Gram-negative E. Coli species even under electricity.[139]

The photographs of three cultured bacteria colony on solid agar plates are shown in Fig. 4.13c and 4.13d. And the colonies for both E. coli and S. aureus under Cu_2O nanowires electrode connected with TENG are much less than the blank sample and the system with Cu_2O nanowires without TENG. The distinctive difference of colony numbers can

also be confirmed by SEM images of Cu_2O nanowire electrodes with/without TENG, as shown in Fig. 4.14.

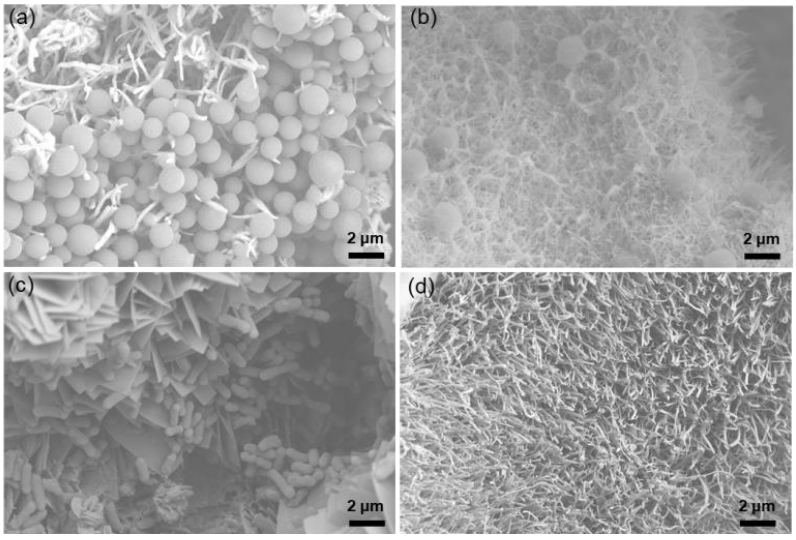

Fig. 4.14 SEM images of S. aurues on the Cu_2O electrode (a) without TENG; (b) with TENG SEM images of E. coli on Cu_2O electrode (c) without TENG; (d) with TENG.

To investigate the mechanism of the enhanced antibacterial property, the ICP-OES was utilized to measure the concentrations of Cu^{2+} with different culture time. As shown in Table 4.3, the concentrations of Cu^{2+} increase with the prolong of culture time for both Cu_2O nanowire electrode and Cu_2O nanowire electrode connected with TENG. The Cu^{2+} of the electrode connected with TENG is slightly higher due to the electrochemical release under electric field. And the antibacterial property of Cu^{2+} can attributed to the direct oxidation of microbial cells in contact with the positive ions.[140] However, the extra Cu^{2+} of Cu_2O electrode connected with TENG cannot achieve the ~2-fold sterilization efficiency compared with Cu_2O electrode.[141] Thus, the electricity may play the prominent role in the enhanced antibacterial property. During electric field treatment, the bacterial cells transport to the vicinity of the electrode driven by the electric field force, where the electric field strength is high enough to cause electroporation.[142] Above all, electroporation works in synergy with metal ions to

improve the sterilization efficiency, as transient pores and increased membrane permeability may enhance the delivery of microbiocidal Cu^{2+} ions into cells.

Table 4.3 Concentration of Cu^{2+} (mg/L) for various culture time

Culture time / Systems	6 h	9 h	12 h
Without TENG	163	379	752
With TENG	188	433	839

To further study the enhanced antifungal property of the system with the TENG against Candida albicans, two samples also with Cu_2O nanowires electrode with/without TENG are fabricated and the sterilization efficiency is shown in Fig. 4.15a.

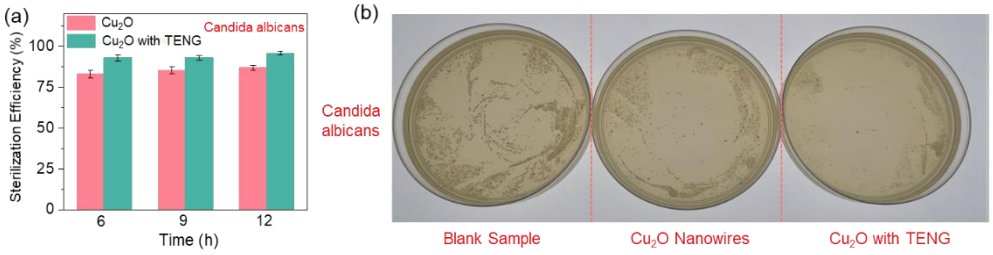

Fig. 4.15 Sterilization efficiency comparison of Cu_2O and Cu_2O with TENG systems of Candida albicans (a) and (b) the corresponding photograph of Candida albicans colonies after culturing for 12 h.

After culturing for 12 h, the sterilization efficiency of system only with Cu_2O nanowires electrode is 86.7%, while the value can reach to 95.8% coupling with the TENG, identifying the enhanced sterilization effect through electricity supply. The cultured colony is also shown in Fig. 4.15b. So, the antibacterial and antifungal efficiency all shows obvious improvement with the TENG acting as electric supply, implying the potential for self-sterilization application.

4.6 Conclusion

In summary, based on the surface morphology observation and chemical composition analysis, the improved electric output mainly originates from the synergistic effect of microcones fabricated by DIL technology, fluorination and roughened surface morphology caused by the FOTS treatment. Moreover, due to the programmability and customizability of the DIL technology, TENG devices with different shapes can be fabricated rapidly. And the fabricated TENG can be used as wearable energy-harvest devices to mechanical energy under various human motion. Finally, the TENG device can serve as the energy supply for the self-powered sterilization application when connecting with the Cu_2O nanowire electrode. The system with TENG show tremendously improved antibacterial/antifungal property compared with the one without TENG. This work demonstrates that the high-performance TENG based on DIL method and surface fluorination is a great candidate for the applications where decentralized electricity is needed and can also be extended to applications in other customized wearable electronic devices.

Chapter 5 Mechanical force-driven growth of tassels-like nickel cobalt phosphate on Nickel Foam

5.1 Introduction

Due to the rapid advances in science and technology, the primary power source is shifting towards electricity sharply.[143, 144] Meanwhile, increasing demand of portable power supplies accompanying with the advent of the Internet of Things has encouraged outpouring research efforts in electrochemical energy storage devices that can store and release electricity reversibly.[145-147] Supercapacitors have gained enormous attention among miscellaneous electrochemical energy storage systems because of its high power density, excellent cyclability and easy maintenance, etc.[148-150] However, the relative low energy density cannot match the requirements of portable electrical appliances, which hinders their practical application severely.[151] According to the equation $E = 1/2\ CV^2$, the energy density is proportionate to the specific capacitance and the square of the working potential windows. There exist two main directions to boost the energy density: broadening the operating potential window and improving the specific capacitance.[97] Combining positive and negative electroactive materials with opposite operating voltage windows,[98] using organic electrolytes, ionic liquids,[2] or charge balance have been considered as effective ways to achieve a wide potential window. To elevate the energy storage capacity, three effective methods for fabricating advanced SC electrodes have been identified by theoretical and experimental explorations: (i) developing electroactive materials with high conductivity and electrochemical activity;[152] (ii) introducing other transition

metal atom into monometallic material to regulate the metallic conductivity and surface reactivity;[153, 154] (iii) selecting conductive substrates with abundant active sites for the growth of active materials to reduce the “dead volume” and facilitate the transportation of ions.[155]

Recently, as a promising material, transition metal phosphate shows great potential for various electrochemical application such as rechargeable batteries,[156] electrocatalytic water splitting,[157] and supercapacitors[154] because of their excellent conductivity, high electrochemical activity, superb theoretical capacity, abundant active sites, open structural channels, and highly stable structure.[158] Taking advantage of their earth abundancy and extraordinary redox performance, various methods have been utilized to fabricate nickel cobalt phosphate electrodes, including hydrothermal,[159, 160] electrodeposition,[161, 162] silicone oil bath method,[163] chemical bath deposition,[164] and sonochemical.[165, 166] However, those nickel cobalt phosphate electrodes still suffer from relative low capacity and poor rate performance due to the underutilized surface area related to the stacked layers of nickel cobalt phosphate and/or the usage of binders. Therefore, it is important to fabricate the self-freestanding nickel cobalt phosphate electrode with favorable micro/nanostructures. Specially, there is still a vacancy for the theoretical understanding for the electronic characteristics of nickel cobalt phosphate.

Mechanical stirring has been proven an effective method to modulate the surface morphography, size, and even dimension of materials.[167-169] In this work, a facile

hydrothermal stirring method was used to directly grow nickel cobalt phosphate on nickel foam substrate for the first time. By regulating the Ni/Co ratios, a tassels-like structure was obtained for $Ni_2Co(PO_4)_2$ (NCP-2). The NCP-2 tassels are composed of well-aligned ultrathin nanosheets only with a thickness of 20 nm, which is beneficial for the effortless ion penetration and fast redox reaction. The NCP-2 electrode reveals a high specific capacity of 2518 mC cm^{-2} (1007 C g^{-1}) at 2 mA cm^{-2} with 76.7% retention at 50 mA cm^{-2}, indicating its high capacity and favorable rate performance. The charge storage mechanism and DFT calculations were performed as well to further understand the electrochemical property of nickel cobalt phosphate. In addition, an asymmetrical supercapacitor assembled with NCP-2 as positive electrode and graphene hydrogel (GH) as negative electrode exhibits a maximum energy density of 46.25 W h kg^{-1} and a highest power density of 7745 W kg^{-1}, which can light LED lights for over 5 minutes, indicating its potential applications in flexible portable electronic devices.

5.2 Materials and equipment

5.2.1 Materials

Ni foam (with purity of 98%, thickness of 1 mm, mass density of 25.5 mg cm^{-2}) was bought from Suzhou Taili Metal Foam Factory (Suzhou, China). Cobalt chloride hexahydrate ($CoCl_2·6H_2O$, 99.9%, metals basis), nickel chloride hexahydrate ($NiCl_2·6H_2O$, 99.9%, metals basis), and dipotassium hydrogen phosphate trihydrate ($K_2HPO_4·3H_2O$, 99.9%, metals basis), Potassium hydroxide (KOH, 99.99% metals basis) were bought from Sigma-Aladdin. All chemicals were obtained for directly use

without purification.

5.2.2 Equipment

The equipment used in this chapter was listed in the table below.

Table 5.1 The equipment for the preparation and characterization of NCP electrodes.

Equipment	Model	Producers
Magnetic stirring apparatus	HJ-4A	Xinrui.co
Oil bath pot	DF-101S	Lichen, Shanghai
Steel reactor	25 mL	Xian Hongchen.co
Air dry oven	DHG-9070A	Yiheng China
Ag/AgCl electrode	218	Leici, Shanghai
Pt electrode	10 × 10 × 0.3 mm	Yueci, Shanghai
Thermal gravimetric analyzer	STA 449F3	Netzsch, German
Micropore analyzer	ASAP2010M	Micrometritics
Transmission electron microscope	JEM 2010 EX	JEOL
Electrochemical station	CHI660E	Chenhua, Shanghai

5.3 Methodology

5.3.1 Fabrication of $Ni_xCo_{3-x}(PO_4)_2$/Ni Foam electrodes

Hydrothermal synthesis is a common method to fabricate nano/micromaterials due to its convenient operation, simple synthesis process, and controllable particle size. The hydrothermal method is a type of soft chemical synthesis method developed by simulating the formation process of some ores in nature. It can be used to grow a variety of single crystals to prepare ultrafine agglomerated or less agglomerated crystallized ceramic powders to complete certain organic reactions, treat some organic waste materials that endanger the human living environment, or sinter some ceramic materials at a relatively low temperature. The nickel cobalt phosphate fabricated through hydrothermal method always possesses large thickness in microscale due to the unavoidable stacking, and mechanical stirring is considered an effective to modulate

the size and dimension of micro/nanomaterials as mentioned above. In this chapter, $Ni_xCo_{3-x}(PO_4)_2$/Ni Foam electrodes are fabricated through a simple hydrothermal stirring process. Details are as follows: Ni foam (10 mm × 10 mm × 1 mm) was ultrasonically cleaned with acetone, ethanol, and deionized (DI) water for 15 min, respectively. Herein, to prepare nickel cobalt phosphate with different nickel and cobalt content, the molar ratio of nickel and cobalt (Ni/Co) varied as 0:3, 1:2, 1.5:1.5, 2:1, and 3:0, and denoted as CP, NCP-0.5, NCP-1, NCP-2, and CP, respectively. For the fabrication of NCP-2/NF composite, 1.2 mmol $NiCl_2·6H_2O$, 0.6 mmol $CoCl_2·6H_2O$ were dissolved in 15 mL DI water firstly. Then 1.2 mmol $K_2HPO_4·3H_2O$ (in 5 mL DI water) was added into the above-mentioned solution dropwise under magnetic stirring and stirred vigorously for another 30 min to obtain a homogenous solution. Afterwards, the mixed solution (10 mL) was transferred into a 25 mL Teflon-lined autoclave with a piece of NF soaked in it. After 12 h reaction at 150°C in oil bath with the stirring rate of 500 rpm, the obtained NCP-2/NF was taken from the autoclave. After washing with DI water to remove residues, the NCP-2/NF was remained in water for further use. The mass loading of electroactive materials was obtained by measuring the mass of NF before and after hydrothermal process. The mass loading of $Ni_xCo_{3-x}(PO_4)_2$ was determined to be ~2.5 mg.

5.3.2 Electrochemical Measurements

All the electrochemical properties were measured on electrochemical workstation with three-electrode system or solid two-electrode system at ambient temperature. For the

three-electrode system, the as-prepared samples were used as working electrode, Pt and Ag/AgCl as the counter and reference electrode, respectively. CV, and GCD were all carried out in 1 M KOH electrolyte. The surface specific capacity (C_s, C cm^{-2}) and mass specific capacity (C_m, C g^{-1}) were calculated based on the GCD results according to the equations (5.1) and (5.2)

$$C_s = I\Delta t/S \qquad (5.1)$$

$$C_m = C_s/m \qquad (5.2)$$

Where I is the discharge current, Δt is the discharging time, S is the area of electrode immersed in electrolyte (1 cm^2), ΔV is the potential window, and m is the mass loading of electroactive materials. Electrochemical impedance spectroscopy (EIS) was also performed within the frequency of 10^5 - 0.01 Hz at 5 mV amplitude.

5.3.3 Charge storage mechanism

Based on the CV curves under various scan rates, the charge storage mechanism can be identified. From a theoretical perspective, the peak current i depends on the scan rate ν which follows the Power's law expressed as below:

$$i(V) = a\nu^b \qquad (5.3)$$

Where a has a constant value and b is determined by the slope of $log\ i$ vs. $log\ \nu$. In this study, the anodic current peaks i were collected to investigate the charge storage mechanism. For the diffusion-controlled redox process such as battery, b = 0.5, this is to say, i shows proportional relationship with the square root of ν. For the surface-confined capacitive process, b =1, that means i shows linear relation with ν. Thus,

according to the *b* values calculated with experimental data, the kinetics of the charge storage mechanism can be investigated qualitatively.

For the electrode combined with diffusion-controlled redox process and surface-defined capacitive processes, the detailed contribution ratios of to the total capacity under various scan rates can be resolved via Dunn's method according to the following equation:

$$i(V) = k_1 v + k_2 v^{1/2} \qquad (5.4)$$

Where $i(V)$ represents the current at the specific potential V, v is the scan rate, $k_1 v$ and $k_2 v^{1/2}$ represent the surface and diffusion controlled current, respectively. This equation can be further transformed through divided it with $v^{1/2}$:

$$i(V)/v^{1/2} = k_1 v^{1/2} + k_2 \qquad (5.5)$$

The detailed values of k_1 and k_2 can be obtained from the slope and intercept of the $v^{1/2}$ vs. $i(V)/v^{1/2}$ plot. These values illustrate the contribution components of capacitive and diffusive behaviors to the total stored charge at a specific scan rate and given potential.

5.3.4 DFT calculation

Vienna Ab Initio Package (VASP) was employed to perform all the density functional theory (DFT) calculations within the generalized gradient approximation (GGA) using the Perdew-Burke-Ernzerhof (PBE) formulation. We have chosen the projected augmented wave (PAW) potentials to describe the ionic cores and take valence electrons into account using a plane wave basis set with a kinetic energy cutoff of 450 eV. Partial occupancies of the Kohn-Sham orbitals were allowed using the Gaussian smearing method and a width of 0.05 eV. The on-site corrections (DFT+U) have been applied to the 3d electron of Ni atoms (U_{eff}=6.2 eV) by the approach from Dudarev et al.[173] The

electronic energy was considered self-consistent when the energy change was smaller than 10^{-5} eV. A geometry optimization was considered convergent when the force change was smaller than 0.02 eV/Å.

The equilibrium lattice constants of monoclinic $Ni_3(PO_4)_2$ unit cell were optimized, when using a 6×4×3 Monkhorst-Pack k-point grid for Brillouin zone sampling, to be a=5.898 Å, b=4.632 Å and c=9.877 Å, α=90°, β=92.7°, γ=90°. This unit cell and a unit cell doped with two Co atoms were used calculate band structure and density of states (DOS).

The pristine $Ni_3(PO_4)_2$ (100) surface model has a p(1x1) periodicity in the x and y directions and two stoichiometric layers in the z direction by vacuum depth of 15 Å to separate the surface slab from its periodic duplicates. The Co-doped $Ni_3(PO_4)_2$ (100) surface model was built by replacing 4 Ni atoms with Co atoms in the $Ni_3(PO_4)_2$. During structural optimizations, a 5 × 2 × 1 in the Brillouin zone was used for k-point sampling, and the bottom stoichiometric layer was fixed while the rest were allowed to fully relax. The adsorption energy of OH^- (E_{ads}) was determined as the following equation:

$$E_{ads} = E_{sub/base} - E_{sub} - E_{base} \qquad (5.6)$$

where $E_{sub/base}$, E_{sub}, and E_{base} are the total energy of the substrate with adsorbed OH^-, pure substrate, and the free OH^-.[170]

5.4 Characterization of $Ni_xCo_{3-x}(PO_4)_2$ electrode

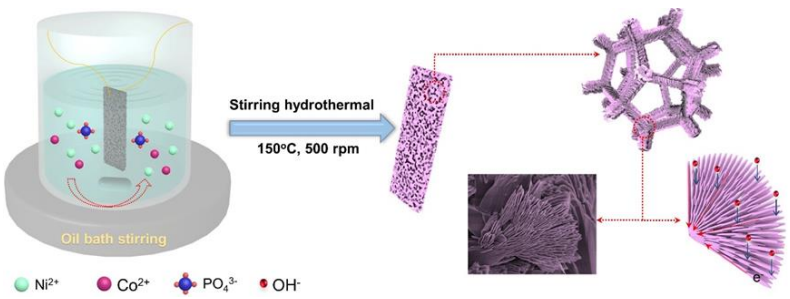

Fig. 5.1 Schematic illustration of the fabrication strategy for $Ni_xCo_{3-x}(PO_4)_2$/NF composite.

The fabrication procedure of the binder-free nickel cobalt phosphate (NCP) electrodes is schematically demonstrated in Fig. 5.1. The tassels-like NCP composed of ultrathin nickel cobalt phosphate nanosheets aligned on the skeleton of NF through an effective hydrothermal stirring process at 150 ^{o}C for 12 h. During this process, phosphate precursor decomposes into PO_4^{3-} and then reacts with Ni^{2+} and Co^{2+}. The reaction mechanism for the formation of nickel cobalt phosphate with different Ni/Co ratio is described in equation (5.7):

$$(3\text{-}x)Ni^{2+} + xCo^{2+} + 2HPO_4^{2-} + nH_2O \rightarrow Ni_{3-x}Co_x(PO_4)_2 \cdot nH_2O + 2H^+ \quad (5.7)$$

In this work, Ni foam serves as the current collector to avoid the addition of binders and shorten the electron transport pathway. Its high conductivity and large surface area can provide abundant active sites for the growth of nickel cobalt phosphate during the hydrothermal stirring process. The mechanical force exhibits important functionalities during the fabrication process. Firstly, the mechanical stirring breaks the balance of dissolution-recrystallization of NCP growth in static hydrothermal condition, generating more dissolution regions on NCP surfaces, preventing the stacking of NCP nanosheets. Secondly, intensive mechanical disturbance can accelerate the mass transport, which enables the uniform growth of NCP. Lastly, the constant stirring prevents the sedimentation of NCP, driving more species attach on the substrate. Thus, the as-prepared nickel cobalt phosphate reveals ultrathin nanosheets with open structure, which can provide unimpeded channel for ion penetration.

The optical photographs of the fabricated $Ni_xCo_{3-x}(PO_4)_2$/NF samples were exhibited

in Fig. 5.2a. The CP sample shows the obvious bright purple, while the NCP-0.5 is dark purple. The NCP-1 seems like light purple, and NCP-2 shows typical light pink. For the NP sample, it is light green.

To verify the chemical composition, FT-IR spectra of the fabricated nickel cobalt phosphate electrodes were performed in the region of 400 ~ 4000 cm^{-1} as exhibited in Fig. 5.2b. The peaks in the range of 520 ~ 580 cm^{-1} attribute to M-O bonding. The peak of Ni-O (γ_1) locates at 540 cm^{-1} in NP,[171] and peak at 564 cm^{-1} in CP reveals the Co-O bonding in the prepared samples.[172] The absorption peaks (γ_2) in the range of 695 ~ 720 cm^{-1} are ascribed to the symmetric stretching of P-O-P bonding.[164] The peaks represent for the stretching vibration of P-O in PO_4^{3-} anions locate in 840 ~ 980 cm^{-1} (γ_3, γ_4).[161] The peaks observed around 1600 cm^{-1} (γ_5) are assigned to the bending mode of water in crystallization (H-O-H).[164] In addition, the peaks over 2800 cm^{-1} (γ_6, γ_7) represent the adsorbed water (O-H bonding) in the surface of the fabricated material.[173] The FT-IR analysis demonstrates the presence of phosphate and crystal water in the fabricated samples, confirming the formation of hydrous nickel cobalt phosphate during the hydrothermal process.

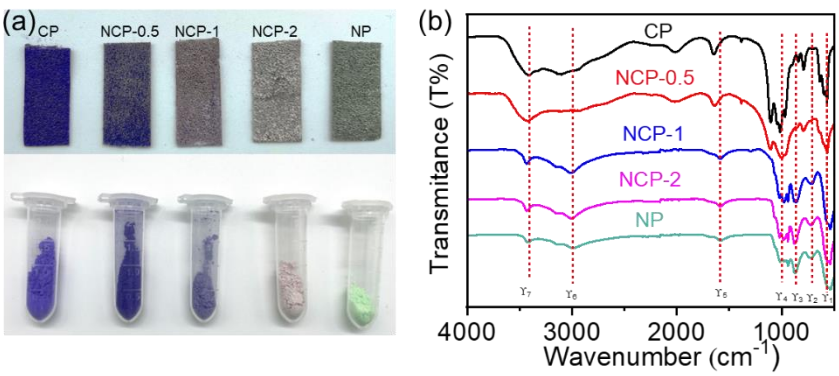

Fig. 5.2 (a) Optical photos and (b) corresponding FT-IR spectra of $Ni_xCo_{3-x}(PO_4)_2$ samples.

The XRD patterns of the $Ni_xCo_{3-x}(PO_4)_2$/NF composites with different Ni/Co ratios are displayed in Fig. 5.3. Three well-defined strong peaks at 44.7°, 52.0° and 76.6° are accounted for the NF substrate for all samples. For the electrode without the addition of nickel source (CP, violet), the diffraction peaks at 10.6°, 26.2°, 30.5°, 33.7° and 35.5° can be indexed to (-111), (200), (021), (-121), and (121) lattice plane of monoclinic $Co_3(PO_4)_2 \cdot 4H_2O$ crystalline phase (JCPDS#34-0844), respectively. The sample without cobalt source (NP, bright green) exhibits peaks at 11.3°, 13.4°, 18.5°, 22.3°, 23.5°, 28.4°, 36.4°, and 37.9°, corresponding to the (110), (020), (200), (130), (101), (031), (141), and (301) plane of monoclinic $Ni_3(PO_4)_2 \cdot 8H_2O$ crystalline phase (JCPDS#33-0591), respectively.

As observed from Fig. 5.3, the diffraction patterns of samples change from $Co_3(PO_4)_2 \cdot 4H_2O$ to $Ni_3(PO_4)_2 \cdot 8H_2O$ gradually with the increase of nickel proportion. In addition, both diffraction peaks of $Co_3(PO_4)_2 \cdot 4H_2O$ to $Ni_3(PO_4)_2 \cdot 8H_2O$ can be found for NCP-0.5 and NCP-1 samples, indicating the coexistence of the two crystalline phases.

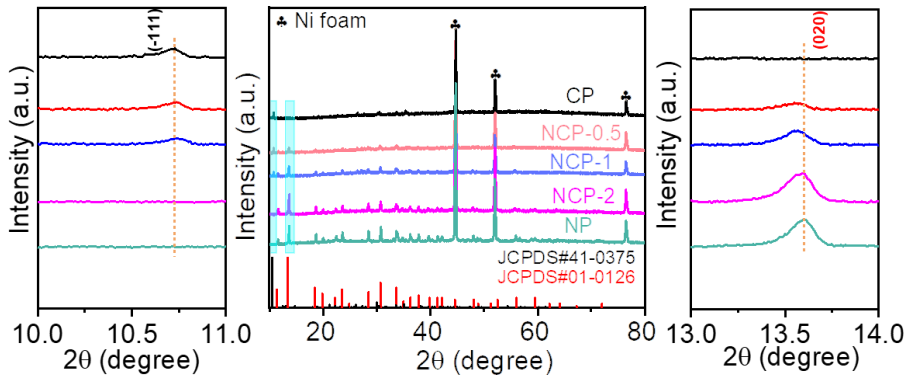

Fig. 5.3 XRD patterns of $Ni_xCo_{3-x}(PO_4)_2$ samples and the enlarged spectra of the (-111) plane (left) and (020) plane.

For NCP-2, only characteristic diffraction peaks of $Ni_3(PO_4)_2 \cdot 8H_2O$ can be observed. The enlarged spectra for the (-111) plane of $Co_3(PO_4)_2 \cdot 4H_2O$ crystalline seem no obvious phase shift, while the (020) plane of $Ni_3(PO_4)_2 \cdot 8H_2O$ (-111) plane of shifts to lower degrees, indicating the insertion of cobalt atoms with larger atomic radius.

Similarly results can also be evidenced by Raman spectra as in Fig. 5.4. The Raman spectra of NP sample mainly composed of three ranges of vibrations, which are in 200 - 300, 350 - 700, and 900 - 1100 cm^{-1}, respectively. Raman shifts at 959.7 and 1046.9 cm^{-1} can be attributed to the respective ν_1 PO_4^{3-} symmetric and ν_3 PO_4^{3-} antisymmetric stretching modes. There also exists a band at 1022.3 cm^{-1} are assigned to the MOH (M = Co, Ni) deformation modes. The band at 907.3 cm^{-1} can be attributed to the water liberation mode, as reported by Breitinger et al[174]. Within the range of 350 - 700 cm^{-1}, there is a peak at 682.2 cm^{-1} corresponding to the ν_4 bending modes of PO_4^{3-} unit. Other peaks at 384.1 and 579.9 cm^{-1} are due to the deformation modes of PO_4 and P-O-P, respectively. The peak observed at 450 cm^{-1} indicates the corresponding O-P-O bending modes. In the low-wavenumber region between 200 - 300 cm^{-1}, two obvious Raman bands at 216.0 and 287.1 cm^{-1} can be attributed to the P-O-P (bridge) bending and M-O stretching (i.e., Ni-O, Co-O) vibrations, respectively.[175] As the metal oxygen stretching occurs in the P-O-P bending region, it is difficult to assign this vibration unambiguously. After the introduction of Co atoms, typical Raman band at 287.1 cm^{-1} in the low-wavenumber region for $Ni_3(PO_4)_2 \cdot 8H_2O$ redshifts for NCP-2 sample, suggesting the successful insertion of cobalt atoms into the crystalline lattice

of NP.[176]

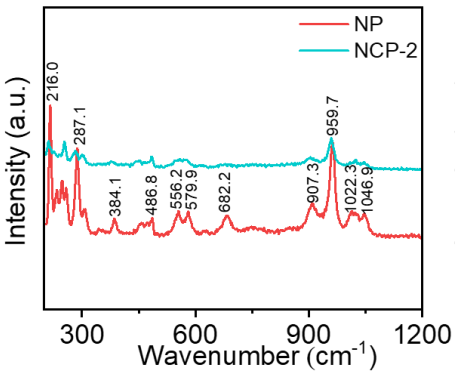

Fig. 5.4 Typical Raman spectra of NP and NCP-2 samples.

TG and DSC measurements for various samples were carried out under the air atmosphere in 50 - 900°C and the results are exhibited in Fig. 5.5. For the CP sample, the mass loss before 100°C is mainly attributed to the loss of adsorbed water and the loss of crystalliferous water mainly occurs at 100 - 550°C. There is still 83.5% residue when the temperature is 900°C, corresponding to the mass contents of cobalt phosphate.

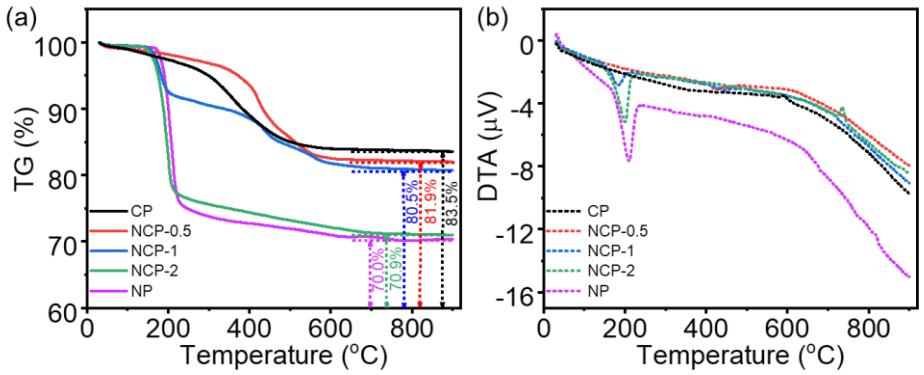

Fig. 5.5 (a) TG curves and (b) DSC plots of $Ni_xCo_{3-x}(PO_4)_2$ samples

For the NP sample, the mass decrease mainly occurs at 135 - 215°C due to the loss of most crystalliferous water. And there is 70.0% residual remained at 900°C due to the much more crystalliferous water existing in nickel phosphate. For NCP-0.5 and NCP-1 samples, there are two stages for the mass loss, indicating the coexistence of nickel

phosphate and cobalt phosphate. For NCP-2 sample, the TG curve is similar with NP and 70.9% retention can be achieved at 900ºC. The DTA curve of CP shows a crystalline transformation peak at 591ºC and for NP, the temperature is 817ºC. Moreover, for NCP-2 sample, there is only a crystalline transformation peak occurs at 735ºC, indicting the insertion of Co into $Ni_3(PO_4)_2 \cdot 8H_2O$.

To further investigated the valance state and chemical composition of the fabricated samples, XPS analysis of NCP-2 was carried out. The survey spectrum (Fig. 5.6a) reveals the existence of Ni, Co, P, and O elements in NCP-2 and the atomic contents ratio of Ni/Co is calculated to be ~1.85 as shown in Fig. 5.6f, which is close to the feeding molar ratio. The detailed elemental contents of Ni and Co for all $Ni_xCo_{3-x}(PO_4)_2$ samples were also evidenced by ICP measurement as exhibited in Table 5.2. For NCP-2, the elemental contents ratio of Ni/Co is 2, indicating that one third of the Ni sites in $Ni_3(PO_4)_2$ are occupied by Co^{2+} ions. The high-resolution spectrum of Ni 2p (Fig. 5.6b) can be fitted with two intense peaks at 873.8 eV and 856.2 eV accompanying with two broad shakeup satellites at higher BE of 880.0 eV and 861.5 eV (designated as "Sat"), which is attribute to the spin-orbit doublets of Ni $2p_{3/2}$ and Ni $2p_{1/2}$, respectively, indicating the oxidation state of Ni^{2+}.[177] Similar fitting results can be found in Co 2p spectrum (Fig.5.6c), where two spin-orbit doublets peaks appear at 797.6 eV and 781.7 eV as well as two shakeup satellites at 802.6 eV and 786.1 eV, implying the presence of Co^{2+}.[178] For high resolution P 2p spectrum in Fig. 5.6d, two deconvoluted peaks observed at 133.2 eV and 134.8 eV represents pentavalent tetra-bonded phosphorous in

PO_4^{3-}.[179]

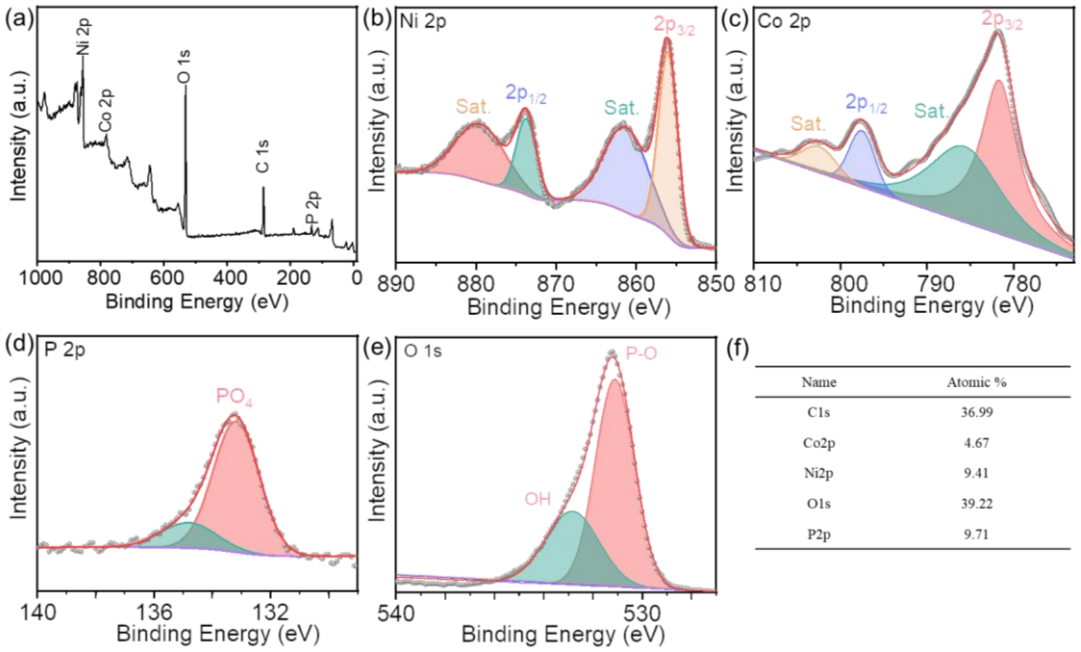

Fig. 5.6 (a) Survey spectrum of NCP-2 electrode; High-resolution XPS spectra of NCP-2: (b) Ni 2p; (c) Co 2p; (d) P 2p; (e) O 1s. (f) Elemental contents.

In addition, the O 1s spectrum is fitted with two peaks as shown in Fig. 5.6e. The peak locates at 531.1 eV related to the P-O bonding and peak at 532.8 eV attribute to the adsorbed water on the surface of nickel cobalt phosphate.[180] Based on the analysis above, the successful fabrication of hydrous nickel cobalt phosphate is confirmed, which is also consistent with the FTIR and XRD results.

Table 5.2 ICP results of $Ni_xCo_{3-x}(PO_4)_2$ with different Ni/Co ratios

Samples	Ni Wt%	Co Wt%	P Wt%	Atom ratio (Ni:Co:P)
CP	--	44.8%	12.3%	3:2(Co:P)
NCP-0.5	13.4%	26.9%	14.1%	1:2:2
NCP-1	20.9%	21.0%	14.7%	1.5:1.5:2
NCP-2	23.9%	12.0%	12.6%	2:1:2
NP	34.9%	--	14.2%	3:2(Ni:P)

SEM was utilized to observe the surface morphological difference of nickel cobalt phosphate with different Ni/Co ratios fabricated through hydrothermal method and hydrothermal stirring method as displayed in Fig. 5.7 and Fig. 5.8. For hydrothermal method, the cobalt phosphate (CP) exhibits microflower structure combined with rectangle microsheets with large aspect ratio (Fig. 5.7a), where the average length is ~100 μm and the average is width is ~5 μm (Fig. 5.7a'). After the addition of nickel with small amount (NCP-0.5), the intact rectangle microsheets change to sisal leaf like structure with sharp edges (Fig. 5.7b) and the average length change to ~30 μm (Fig. 5.7b'). With the increase of nickel content (NCP-1 and NCP-2), microflowers composed of rectangular microplates with smaller size appear on the surface of NF, and the average length of microplates of is ~10 μm (Fig. 5.7d-e'). For nickel phosphate (NP), similar morphology with NCP-1 and NCP-2 can be observed as shown in Fig. 5.6f and f' but seems sparser without too much overlayed microplates.

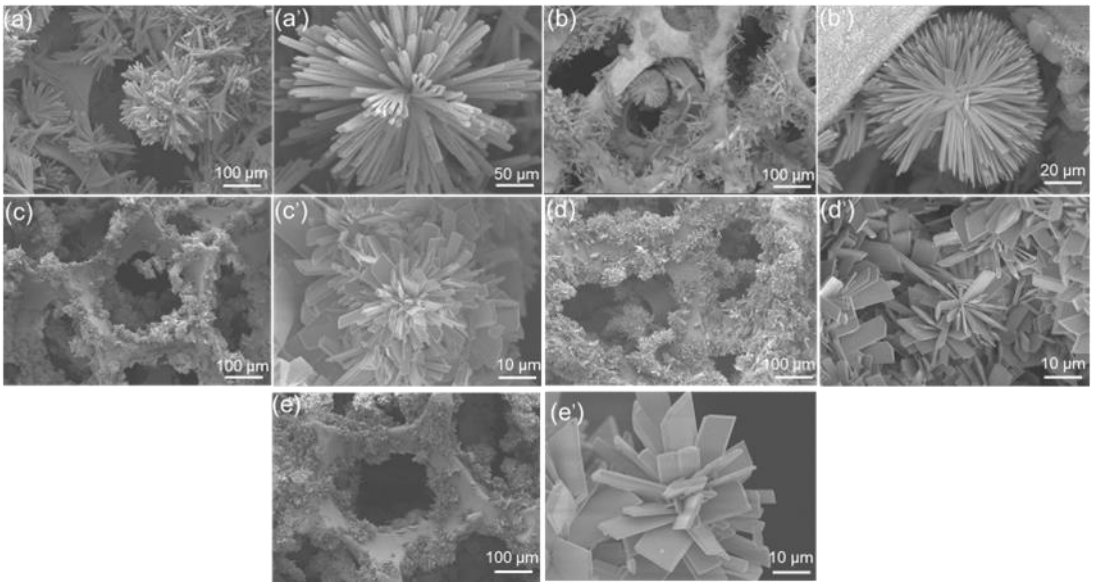

Fig. 5.7 SEM images of $Ni_xCo_{3-x}(PO_4)_2$ with different Ni/Co ratios by hydrothermal method. (a) CP; (b) NCP-0.5; (c) NCP-1; (d) NCP-2; (e) NP.

For the hydrothermal stirring method samples, CP exhibits similar microflower structure compared with hydrothermal prepared CP, while the average length is ~20 μm and the average thickness is ~2 μm. From the enlarged view, the microsheets are composed of numerous interconnected nanosheets with the thickness of ~50 nm. For NCP-0.5, the sisal leaf like structure become disorder with gradual sharp edges and the average length changes to ~15 μm. Moreover, there are numerous small flakes disorderly disperse on the large sisal leaf like sheets.

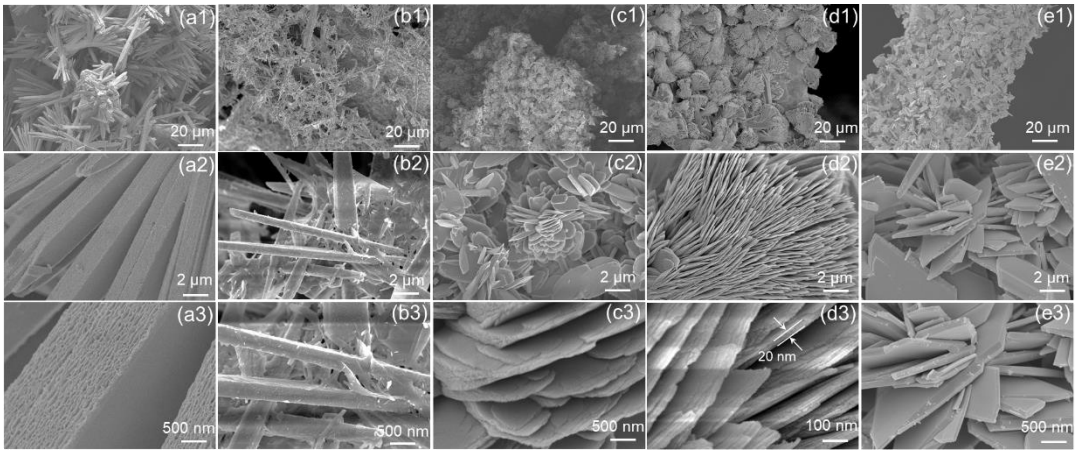

Fig. 5.8 SEM images of $Ni_xCo_{3-x}(PO_4)_2$ with different Ni/Co ratios by hydrothermal stirring method. (a) CP; (b) NCP-0.5; (c) NCP-1; (d) NCP-2; (e) NP.

NCP-1 shows a microflower structure composed of thin nanosheets with the average length of ~2 μm and the thickness of 100 nm. For the NCP-2, tassels-like structure composed of ultrathin nanosheets aligned on the NF skeleton. The average size of the nanosheets is ~2 μm with the thickness of 20 nm. For nickel phosphate (NP), the microflower structure is composed with thin nanosheets of ~200 nm. Noticeably, the micro/nanostructures fabricated through hydrothermal exhibit much thinner and shorter plates/sheets compared with those fabricated by hydrothermal method. That can be

contributed to the mechanical stirring, which not only prevent the stacking of nickel cobalt phosphate plates/sheets, but also guarantee the uniformly grow in vertical and horizontal direction.

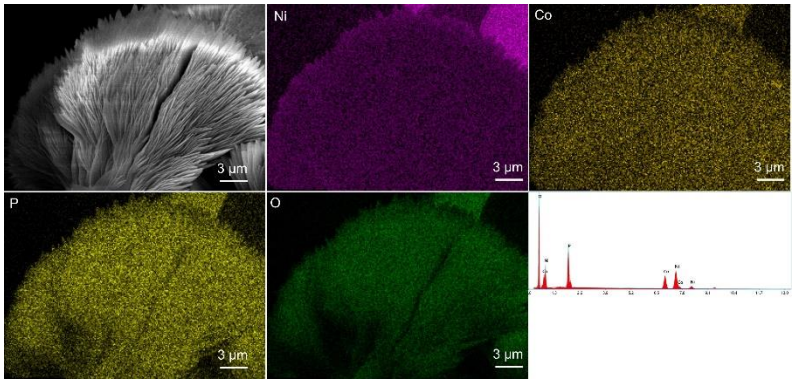

Fig. 5.9 Elements mapping of NCP-2.

The element mapping images of NCP-2 are as shown in Fig. 5.9. It can be obviously seen that the Ni, Co, P, and O elements are uniformly disperse throughout the microplates, confirming the homogeneous growth of nickel cobalt phosphate.

Based on the SEM observation for NCP-2 with different reaction time(Fig. 5.10), we proposed a possible formation mechanism of the tassels-like NCP-2 composed of ultrathin nanosheets. Firstly, NCP nanosheets stack loosely due to the existence of mechanical force (Fig. 5.10a and Fig. 5.10e-I), and large amounts of active sites exposed to the reaction precursor. Then, the precursor tends to adsorb on the edge of NCP nanosheets, thus new crystallization sites formed. A new layer NCP nanosheets gradually grow uniformly due to the fast mass transportation under strong mechanical disturbance. Meanwhile, the growth of the new NCP layer makes the first NCP layer more apart (Fig. 5.10b, c and Fig. 5.10e-II). The growth of new layers repeats for

several times and finally form the tassels-like structure composed of ultrathin NCP nanosheets (Fig. 5.10d and Fig. 5.10e -III).

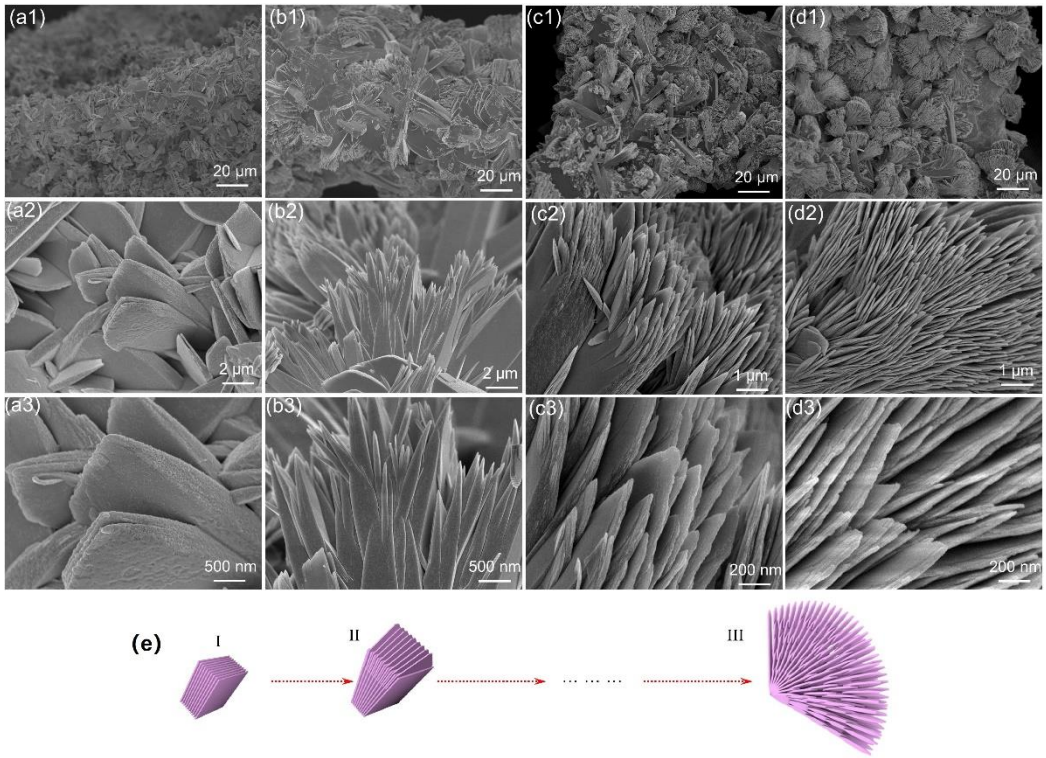

Fig. 5.10 NCP-2 fabricated by hydrothermal stirring method for different time. (a) 3 h; (b) 6 h; (c) 9 h; (d) 12 h. (e) The proposed formation mechanism.

The SEM images of NCP-2 fabricated by under varous stirring speed can be found in Fig. 5.11. When the stirring speed is 200 rpm, there are densely packed tassels-like structure appear on the surface of nickel foam with the average thickness of 100 nm, which is thicker than the NCP-2 fabricated under 500 rpm. That may attribute to the small machinal disturbance cannot fully open the stacked layer. When the stirring speed increases to 800 rpm, there are numerous quasi-sphere microflowers appear, which are composed of tremendous NCP nanosheets with the thickness of 50 nm. When the stirring speed is 1000 rpm, disordered plates formed, because the strong machinal disturbance may destroy the gradually growth of NCP-2.

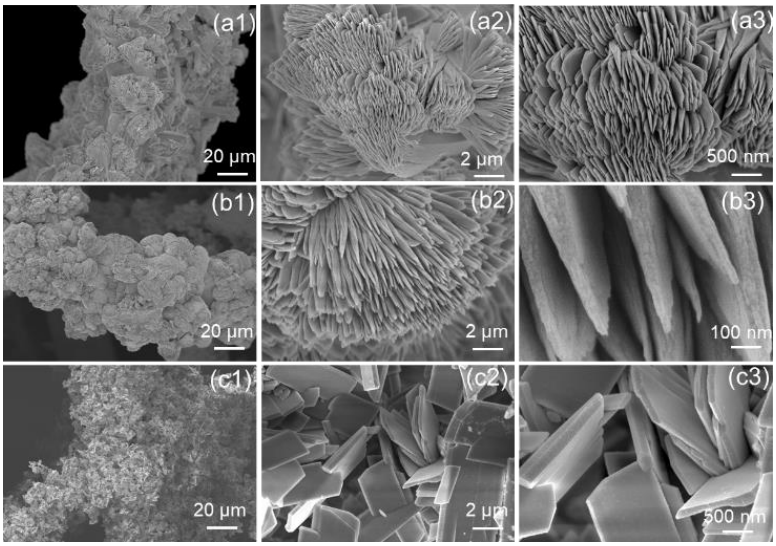

Fig. 5.11 SEM of NCP-2 fabricated with various stirring speed. (a) 200 rpm; (b)800 rpm; (d) 1000 rpm. of NCP-2.

The surface morphologies of the NCP-2 fabricated by hydrothermal stirring method under 500 rpm and hydrothermal method are visualized with TEM measurement as shown in Fig. 5.12. The surface of ultrathin NCP-2 nanosheets reveals a porous structure with numerous pores on the nanosheets (Fig. 5.12a and 12b), which is fairly different from the electrode fabricated with hydrothermal method, which has plane and smooth surface as shown in Fig. 5.12e. The HRTEM image (Fig. 5.12c) shows well-resolved parallel lattice fringes with the distance of 0.48 nm and 0.36 nm, assigning to the (200) and (101) planes of monoclinic nickel cobalt phosphate. Also, the SAED pattern (Fig. 5.12d) reveals the polycrystalline nature, which is also quite different from the single crystal phase of NCP fabricated through hydrothermal method (Fig.5.12f). The numerous pores and defects on the NCP nanosheets can provide tremendous exposed active sites, leading to fast ion transport and charge transfer and further boosting the electrochemical performance.[96, 165]

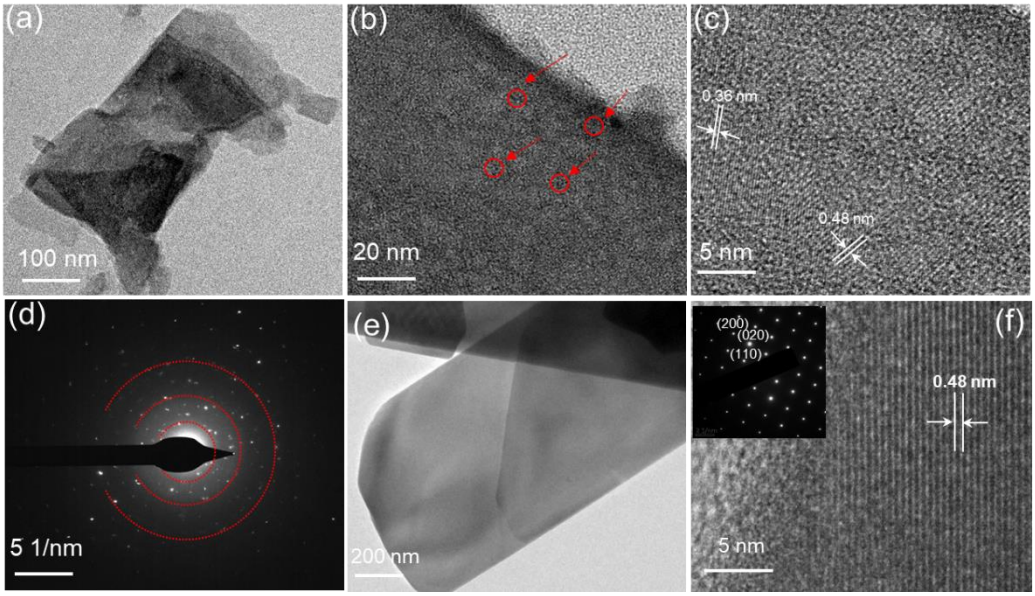

Fig. 5.12 (a, b) TEM and (c) HRTEM images; (e) corresponding SAED pattern for NCP-2 nanosheets fabricated with hydrothermal stirring method; (e) TEM image; and (f) HRTEM images of NCP-2 microplate obtained by hydrothermal method; the inset (f) shows the corresponding SAED pattern.

The element mapping images in Fig. 5.13 reveal the uniform distribution of Ni, Co, P, and O elements throughout the nanosheet, which is also consistent with the element mapping in Fig. 5.9.

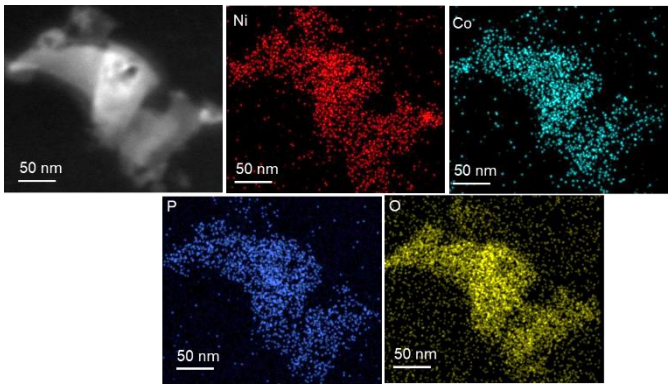

Fig. 5.13 Elements mapping of NCP-2 nanosheet.

The surface area and pore size distribution of nickel cobalt phosphate with different Ni/Co ratios were identified with N_2 adsorption-desorption isotherms as provided in Fig. 5.14. In terms of the IUPAC classification, both isotherms of nickel cobalt

phosphate sample show type III isotherm with mild hysteresis loop (H3 type), indicating the existence of macro/mesoporous with slit-shaped pores produced by platelike structure.

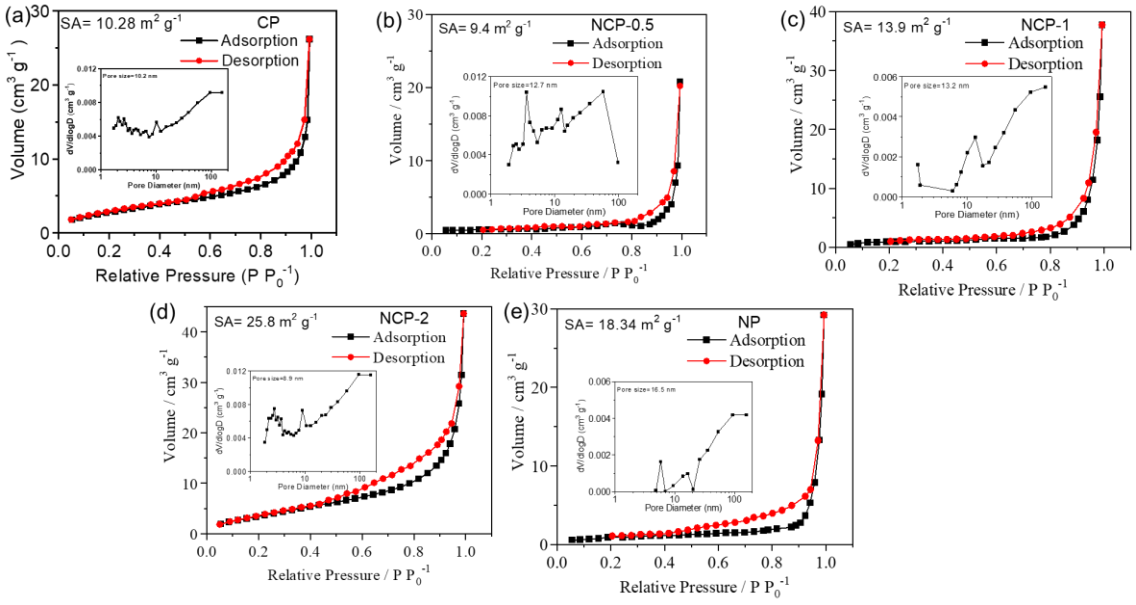

Fig. 5.14 Nitrogen adsorption/desorption isotherm of (a) CP; (b) NCP-0.5; (c) NCP-1; (d) NCP-2; and (e) NP fabricated through hydrothermal stirring method with the stirring speed of 500 rpm (inset: pore size distribution).

The specific surface area calculated with Brunauer-Emmett-Teller (BET) equation were 10.3, 9.4, 13.9 25.8 and 18.3 m^2 g^{-1} for CP, NCP-0.5, NCP-1, NCP-2 and NP samples, respectively. The surface area of samples with microplates structure (NCP-1, NCP-2 and NP) shows obvious increase compared with long microsheets structure (CP and NCP-0.5), and NCP-2 sample possesses a high specific surface area of 25.8 m^2 g^{-1} during these samples, indicating large effective area for ion contact. The pore size distributions of NCP-2 based on Barrett-Joyner-Halenda (BJH) calculation is centered at ~8.9 nm, implying the presence of mesopores, which is also favorable for the transport of ions.[181]

5.5 Electrochemical performance of $Ni_xCo_{3-x}(PO_4)_2$ electrode

The electrochemical comparison of NCP-2 fabricated by hydrothermal stirring method with different stirring speed are displayed in Fig. 5.15. The NCP-2 with 500 the speed of 500 rpm exhibits the largest CV area and the longest discharge time, indicating 500 rpm is the optimal stirring speed. For the following discussion, the stirring speed for all samples is fixed at 500 rpm except for special notification.

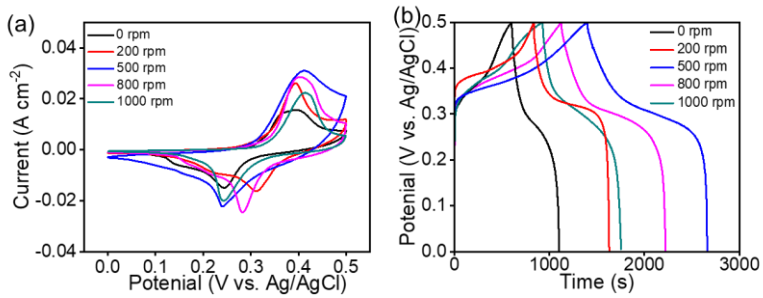

Fig. 5.15 (a) CV and (b) GCD comparison of NCP-2 fabricated by hydrothermal stirring method under various stirring speed.

For nickel cobalt phosphate, morphology show obvious correlation Ni/Co molar ratios, and their supercapattery performance is firstly investigate by CV and GCD measured with three-electrode cell. Fig. 5.16a displays the comparative CV curves of nickel cobalt phosphate electrodes at the scan rate of 5 mV s^{-1} within 0 to 0.5 V. All curves show pseudocapacitive features with distinct redox peaks appears at around 0.25 and 0.35 V, associating with the reversible intercalation/deintercalation of OH^- ions into nickel cobalt phosphate.[164] NCP-2 electrode exhibits the greatest area of CV loop, suggesting the optimized electrochemical capacity. Furthermore, the typical CV curves of NCP-2 electrode at various scan rates are depicted in Fig. 5.16b. With the scan rates increase from 1 mV s^{-1} to 50 mV s^{-1}, the redox peak currents and loop area of CV curves

increase sequentially. Meanwhile, the oxidation peak shifts positively and reduction peaks moves negatively, which may attribute to the increased internal diffusion resistance at relative fast sweep speed. The redox peaks can be observed clearly even at 50 mV s^{-1}, as well as the CV shape is well-maintained without obvious polarized, implying the favorable electrochemical reversibility and satisfactory rate performance of NCP-2 electrode.

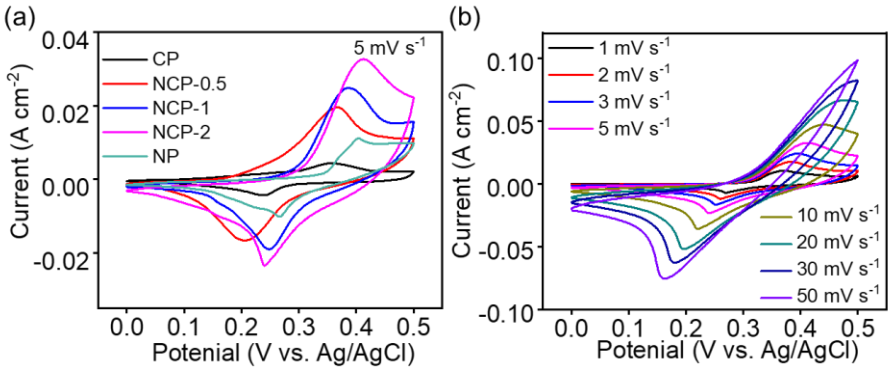

Fig. 5.16 (a) CV curves of nickel cobalt phosphate at 5 mV s^{-1}; (b) CV curves of NCP-2 electrode at various scan rates.

Generally, the electrochemical storage capacity is composed of the diffusion-controlled redox (intercalation) process and the surface-confined capacitive process,[182] which can be determined with the kinetic analysis based on the CV curves at different scan rates. The relationship between the peak currents in CV curves and sweep rate conforms the Power's law, that is $i = av^b$.[96] When the b equals to 0.5, it indicates the complete battery-type diffusion-controlled redox (intercalation) process, whereas the b-value of 1.0 implies the surface-confined characteristic, such as the electric double layer capacitance. The b-value of NCP-2 electrode calculated based on anodic and cathodic peak currents is 0.57 and 0.60 as shown in Fig. 5.17a, indicating the existence of

capacitive and semi-infinite diffusion process in the stored charge. At the scan rate of 1 mV s^{-1}, the capacitive contribution of NCP-2 electrode is 30.7% (Fig. 5.17b), suggesting the stored charges mainly derive from the diffusive intercalation at slow sweep speed.

The contribution percent of the two storage process at different scan rates are quantified as depicted in Fig. 5.17c. The surface capacitive contribution ascends gradually with the increase of scan rates because the relatively slow diffusion-controlled intercalation process cannot keep pace with the increased scan rate, resulting in the diminish of diffusion contribution.

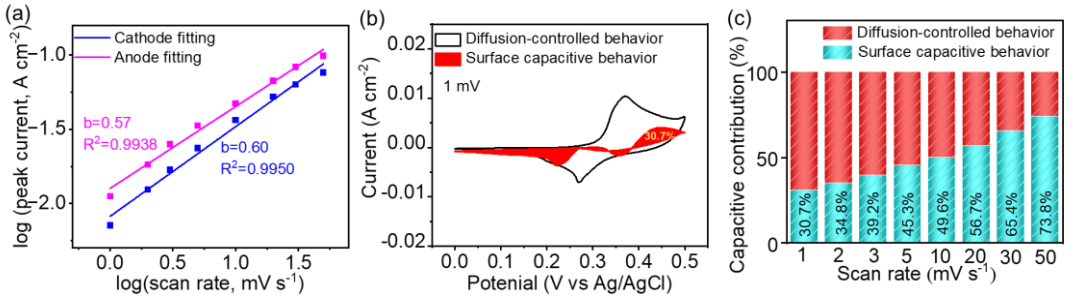

Fig. 5.17 (a) Resolution of the b value from the slope of log (peak current) vs. log (scan rate) plot based on the CV curves of NCP-2; (b) separation of the capacitive contribution (red shadow area) and diffusive contribution (blank area) to the CV currents at 1 mVs-1 for NCP-2; (c) capacitive and diffusive contribution ratios in the total stored charges at different scan rates for NCP-2 electrode.

The GCD curves in Fig. 5.18a-e was obtained at the current density of 2 to 50 mA cm^{-2} for all samples. The non-linear curves with obvious voltage plateau during the charge/discharge process indicate typical supercapattery behavior of $Ni_xCo_{3-x}(PO_4)_2$/NF electrodes, which is attribute to the deep intercalation and slow deintercalation of OH^-[183]. The NCP-2 exhibits the longest discharging duration

compared to other samples, which is also consistent with the CV analysis, demonstrating the superior storing capacity of NCP-2.

The specific capacity calculated based on GCD curves at different current density are exhibited in Fig. 5.18f. For all nickel cobalt binary metal phosphate, the capacities show evident improvement compared with nickel or cobalt phosphate due to the synergetic effect of binary metal.[177] NCP-2 possesses the highest capacity of 2518 mC cm^{-2} (1007 C g^{-1}) at 2 mA cm^{-2}, which is much larger than that of NCP-2 fabricated by hydrothermal method as shown in Fig. 5.19a. The high capacity can be attributed to the full penetration of electrolyte ions, thus active material can exhibit capacity ultimately. On the other hand, the tassels-like structure with ultrathin nanosheets facilitates the transportation of electrolyte ions, contributing to the high capacity as well.

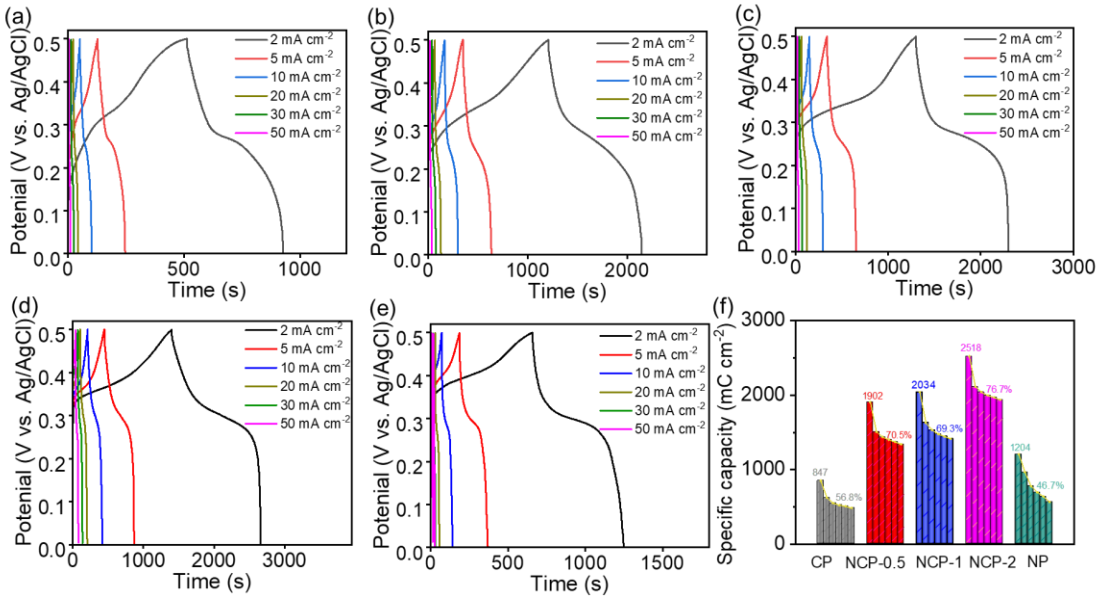

Fig. 5.18 GCD curves of nickel cobalt phosphate with various Ni/Co ratios at different current density. (a) CP; (b) NCP-0.5; (c) NCP-1; (d) NCP-2; and (e) NP electrodes. (f) Specific capacity at different current density for nickel cobalt phosphate with various Ni/Co ratios.

Surprisingly, the capacity of NCP-2 electrode is comparable or superior to those nickel

cobalt phosphate as listed in Table 5.3.

Table 5.3 Comparison of electrochemical performance of nickel-cobalt phosphate related electrode.

Material	Morphology	Fabrication method	Capacity (C g^{-1})	Capacitance retention (C g^{-1})	Ref.
$Co_{0.86}Ni_{2.14}(PO_4)_2$	Honeycomb	Hydrothermal and pyrolysis	705 (0.5 A g^{-1})	514 (10 A g^{-1})	[184]
$NaNi_{0.33}Co_{0.67}PO_4$	Particles	Microwave	414 (1 A g^{-1})	364 (10 A g^{-1})	[185]
$KCo_{0.33}Ni_{0.67}O_4$	Microplates	Hydrothermal	583 (1.5 A g^{-1})	396 (30 A g^{-1})	[186]
$Ni_{1.38}Co_{1.62}(PO_4)_2$	Microflowers	Chemical bath deposition	446 (0.5 A g^{-1})	321 (2 A g^{-1})	[164]
$CoNi_2(PO_4)_2$	Flowers	Precipitation	630 (1 A g^{-1})	560 (10 A g^{-1})	[187]
$Ni_4Co_5(PO_4)_6$	Nanosheets	Co-precipitation	453 (1 A g^{-1})	285 (10 A g^{-1})	[188]
$Ni_3P_2O_8$-$Co_3P_2O_8$	Nanoparticles	Co-precipitation	792 (0.5 A g^{-1})	530 (8 A g^{-1})	[189]
$Ni_{1.5}Mn_{0.5}(PO_4)_2$	Nanoparticles	Co-precipitation	678 (0.8 A g^{-1})	156 (8 A g^{-1})	[190]
$Ni_{0.5}Co_{0.5}WO_4$	Nanoparticles	Hydrothermal	637 (1 A g^{-1})	478 (10 A g^{-1})	[191]
Ni-$Co_3(PO_4)_2$	Flowers	Silicone oil bath	388.8 (0.5 A g^{-1})	216 (10 A g^{-1})	[163]
$Ni_{2.25}Co_{0.75}(PO_4)_2$	Flakes	Sonochemical and calcination	300 (3 A g^{-1})	180 (6 A g^{-1})	[165]
$Ni_{1.5}Co_{1.5}(PO_4)_2$	Clustered nanoparticles	Electrodeposition	891 (1.5 A g^{-1})	700 (3.5 A g^{-1})	[161]
$Ni_2Co(PO_4)_2$	Microflower	Hydrothermal	805 (0.8 A g^{-1})	411 (20 A g^{-1})	This work
$Ni_2Co(PO_4)_2$	Tassels-like	Hydrothermal stirring	1007 (0.8 A g^{-1})	772.4 (20 A g^{-1})	This work

The favorable electrochemical performance of the NCP-2 electrode can be attributed to its unique tassels-like structure composed of ultrathin nanosheets, which is favorable for the penetration of electrolyte, large specific surface area which can efficiently improve the effective contact surface area, and suitable pore size which is suitable for

the transportation of ions. Meanwhile, the specific capacity decreases with the increase of current density. For NCP-2, 76.7% of the capacity retains at 50 mA cm^{-2}, which is much higher than the sample fabricated with hydrothermal method under the same condition as shown in Fig. 5.19c, indicating the favorable rate performance associating with the unique tassels-like structure composed of ultrathin nanosheets.

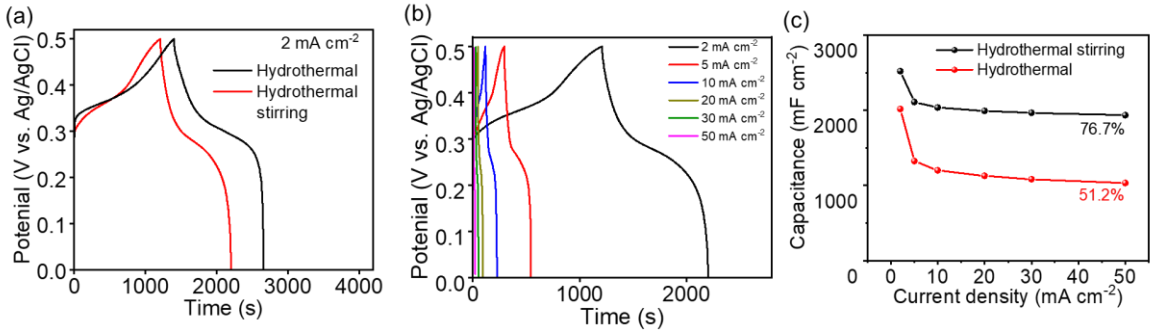

Fig. 5.19 (a) GCD comparison of NCP-2 fabricated with different method. (b) GCD curves of NCP-2 fabricated with hydrothermal method under various current density. (c) Specific capacity comparison at different current density for NCP-2 fabricated by different method.

EIS study was further utilized to analysis the charge transfer behavior and conductivity of nickel cobalt phosphate electrodes. Fig. 5.20a exhibits the Nyquist plots of the as-prepared electrodes in the range of 10^5 - 0.01 Hz with an open amplitude of 5 mV. The intersects of the Nyquist plots with the real component at high frequency region correspond to the equivalent series resistance (R_s), which is the aggregation of the resistance of electrode, active materials, electrolyte, and their interfacial resistance. As observed in the inset of Fig.5.20a, nickel cobalt binary phosphate of NCP-0.5 (1.46 Ω), NCP-1 (1.65 Ω) and NCP-2 (1.54 Ω) show improved conductivity compared with bare CP (1.85 Ω) and NP (1.79 Ω) electrodes, implying more feasible penetration of electrolyte with active materials.

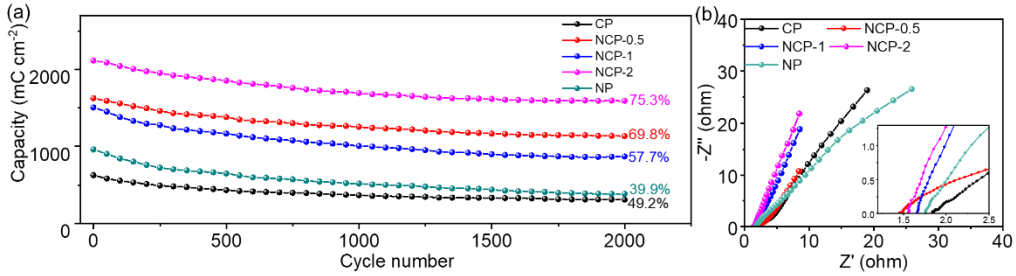

Fig. 5.20 (a) Nyquist plots of nickel cobalt phosphate within the frequency of 10^5-0.01 Hz with an open amplitude of 5 mV. (b) Cycling stability of nickel cobalt phosphate at 5 mA cm^{-2}.

The semi-circle region in the middle frequency region indicates the resistance (R_{ct}) of charge transfer during faradic process, and all samples show small R_{ct}, implying the fast charge transfer kinetics. The above-mentioned EIS analysis indicates the introduction of Co atoms can improve the conductivity of the electrodes. However, excessive Co atoms cannot induce the further improved capacity. The cycling stability was also investigated for all samples at 5 mA cm^{-2} for 2000 cycles as shown in Fig. 5.20 b. For NCP-0.5, NCP-1 and NCP-2, there are 69.8%, 57.7% and 75.3% of its initial capacity is remained after 2000 cycles, respectively. The nickel cobalt bimetal phosphate composites also show improved cycling stability compared with bare NP (39.9%) and CP (49.2%) electrodes.

The cycling stability and Coulombic efficiency comparison of NCP-2 fabricated with hydrothermal stirring and hydrothermal method are displayed in Fig. 5.21a. The NCP-2 obtained by hydrothermal stirring method show obviously enhanced cycling stability and improved Columbic compared with NCP-2 obtained by hydrothermal method. This can be attributed to the unique tassels-like structure composed of ultrathin nanosheets. The closely interacted NCP-2 nanosheets can support each other, reducing the collapse

of the structure, thus high cycling stability can be achieved. Moreover, the ultrathin nanosheets ensure the effortless ion penetration and facilitate the fast redox reaction, thus can realize the high Coulombic efficiency. The small reaction resistance and fast capacitive behavior can also be found in EIS as shown in Fig. 5.21b.

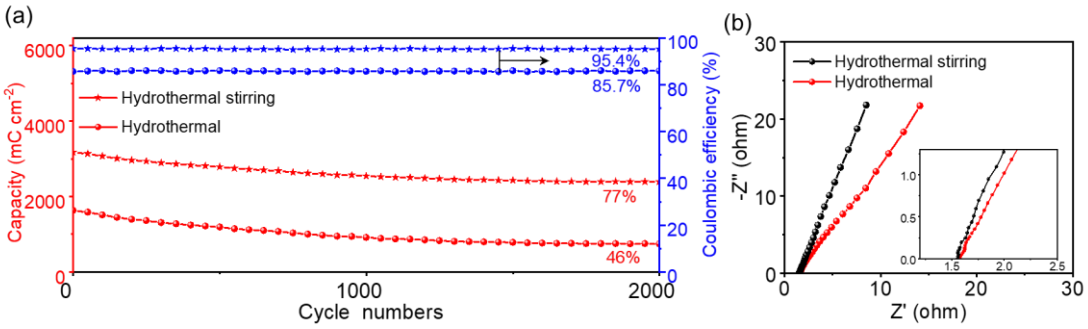

Fig. 5.21 (a) Cycling stability and Coulombic efficiency comparison and (b) EIS comparison of NCP-2 obtained by hydrothermal stirring method and hydrothermal method.

5.6 DFT calculation for $Ni_2Co(PO_4)_2$

To further understand the structural and electronic properties of $Ni_2Co(PO_4)_2$, density functional theory (DFT) calculations were implemented to elucidate the influence of Co doping through generalized gradient approximation (GGA) method. The detailed computation was described in SI. The crystal structures of $Ni_3(PO_4)_2$ and $Ni_2Co(PO_4)_2$ are exhibited in Fig.5.22a and 22b, respectively. The structure of $Ni_2Co(PO_4)_2$ is composed of hexagonally close packed layers of oxygen. Co and Ni atoms are in octahedral CoO_6 (blue) and NiO_6 (green) sites. The distorted octahedra share edges with tetrahedra PO_4 (purple).[192] The model system used for computation is based on the $Ni_3(PO_4)_2$ with 26 atoms and the optimized vectors of *a*, *b*, *c* is 5.897, 4.632, 9.877 Å, respectively. The bond length of Ni-O and P-O were determined as 2.10, and 1.54 Å, respectively. Then, the third of Ni sites were substituted by Co atoms based on the

complete structural optimization. The bond length of Ni-O, Co-O and P-O were found as 2.20, 2.06, and 1.54 Å, respectively. The bond length of Co-O is longer than Ni-O, suggesting fast reaction kinetics.[193]

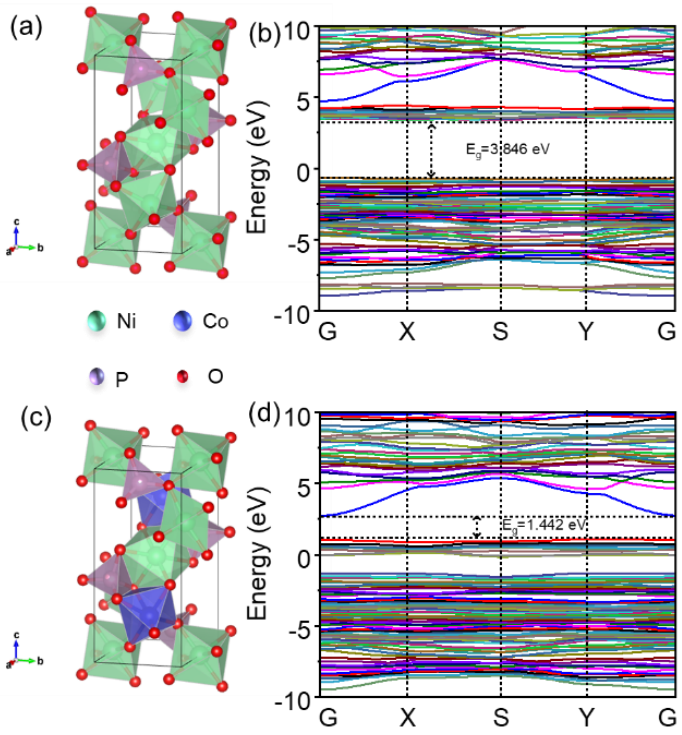

Fig. 5.22 Properties of $Ni_3(PO_4)_2$. (a) crystal structure; (b) calculated band structure; Properties of $Ni_2Co(PO_4)_2$. (c) crystal structure; (d) calculated band structure.

The partially density of state (PDOS) in Fig. 5.23a and b demonstrate that valance band and conduction band all shift toward Femi level after the introduction of Co atoms, leading to enhanced conductivity and higher carrier density, which is also consistent with the EIS results. The band structures in Fig.5.23c and d illustrate that $Ni_2Co(PO_4)_2$ possesses lower band gap of 1.442 eV compared with that of Ni_3 $(PO_4)_2$ (3.846 eV), indicating the improved conductivity, which can boost the transport rate of electrons and result in fast redox reaction kinetics.

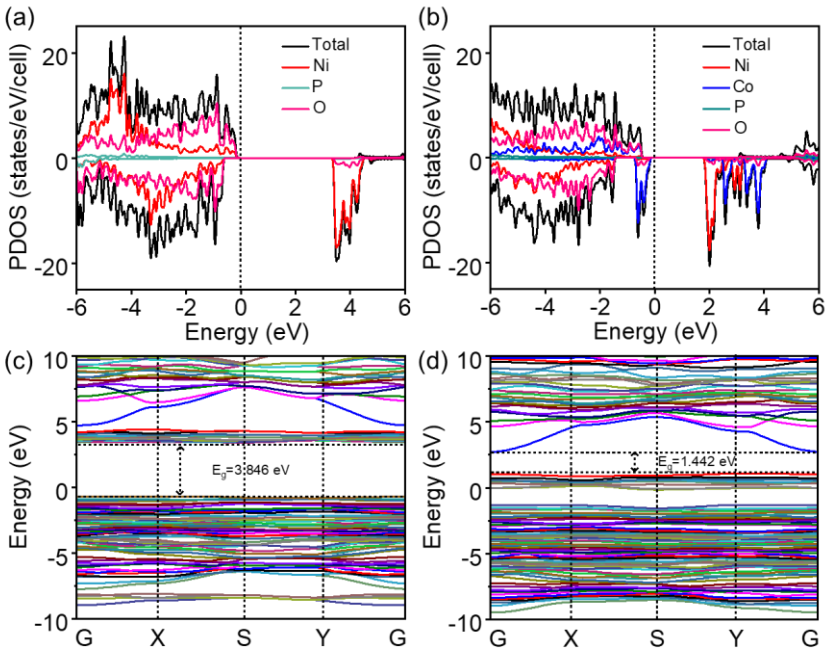

Fig. 5.23 Densities of states of (a) $Ni_3(PO_4)_2$ and (b) $Ni_2Co(PO_4)_2$. Calculated band structure of (c) $Ni_3(PO_4)_2$ and (d) $Ni_2Co(PO_4)_2$.

To evaluate the absorption ability of OH^- for $Ni_3(PO_4)_2$ and $Ni_2Co(PO_4)_2$, the adsorption energies of OH^- for the (200) crystalline plane were calculated as shown in Fig. 5.24. The adsorption energy of $Ni_2Co(PO_4)_2$ is -1.98 eV, which is lower than pure $Ni_3(PO_4)_2$ (-0.96 eV), implying improved adsorption capacity of OH^- after introduction of Co atoms. Above all, DFT results indicate the Co doping can significantly enhance the electrochemical performance.

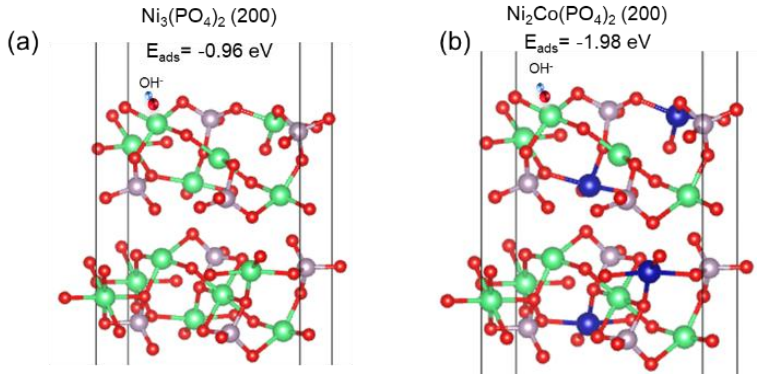

Fig. 5.24 The adsorption energies of OH^- for the (200) plane of (a) $Ni_3(PO_4)_2$ and (b) $Ni_2Co(PO_4)_2$.

Based on the analysis above, the remarkable electrochemical performance of NCP-2 electrode can be ascribed to its morphology, high conductivity, and strong adsorption capacity of OH^-. First, flower-like structure composed of open microplates with small size provides more exposed sites for ion penetration, which is conducive for the contact of electrolyte and electroactive materials. Second, DFT computation confirms the introduction of Co atoms can regulate the band structure, and the smaller band gap after Co doping indicates high conductivity. Third, stronger adsorption capacity of OH^- for NCP-2 is favorable for the redox reactions.

5.7 Conclusion

In summary, we have developed a facile hydrothermal stirring approach to nickel directly grow cobalt phosphate on nickel foam. $Ni_2Co(PO_4)_3$ electrode forms tassels-like structure composed with ultrathin nanosheets, which can attribute to the boosted ion diffusion and chemical reaction under mechanical stirring condition. The ultrathin nanosheets with numerous pores and defects are favorable for the ion penetration and electron transportation. The optimized $Ni_2Co(PO_4)_3$ electrode with one third of the Ni sites replaced by Co demonstrates the maximum specific capacity of 2518 mC cm^{-2} (1007 C g^{-1}) at 2 mA cm^{-2} and remains 76.7% of the initial capacity at 50 mA cm^{-2}. The storge mechanism analysis indicated the combination of the surface-capacitive controlled process and the diffusion-intercalated controlled process. First principles calculations based on DFT were utilized to analyze the structural and electronic

properties. $Ni_2Co(PO_4)_3$ possesses higher conductivity and stronger adsorption capacity of OH^- by introducing Co atoms.

Chapter 6 Application of asymmetric supercapacitors based on $Ni_2Co(PO_4)_3$ electrode

6.1 Introduction

In this chapter, we will first assemble asymmetric supercapacitor (ASSC) using NCP-2 as the positive electrode and graphene hydrogel (GH) as the negative electrode. The electrochemical performance of the ASSC device is measured. Furthermore, the application of ASSC device in powering piezoresistive sensor, fan, calculator and LED lights are explored. Finally, the SCPS composed of ASSC device and 3D-printed TENG device is fabricated and evaluated.

6.2 Materials

Graphene oxide suspension (GO, 10 mg mL^{-1}) was purchased of XFNano, Nanjing, and graphene powder (1 - 6 layers, thickness: 4 - 7 nm; size: 6 μm × 6 μm; purity: 99.7%), PVA (1788, 87% - 89%), n-Octanal (AR, 99.0%) and Carboxymethyl cellulose (CMC, DS = 0.7, 200 - 500 mPa s^{-1}) were purchased from Aladdin-Sigma. PDMS matrix (Sylgard 184) and curing agent were bought from Dow Corning Co., Ltd. 1,1,1,3,3,3-Hexafluoro-2-propanol (99.5%) was purchased from Aladdin Co., Ltd. TPU pellets were purchased from Bayer Material Science.

6.3 Methodology

6.3.1 Fabrication of graphene hydrogel

10 mL GO suspension (3 mg/mL) was transferred to a 25 mL Teflon-lined autoclave and then maintained at 180°C for 12 h. After cooling down, the electrode was washed with DI water and the porous graphene hydrogel (GH) electrode was obtained. The electrochemical performance of GH was measured using a three-electrode system with

KOH as electrolyte.

6.3.2 Assemble of asymmetric supercapacitor

The asymmetrical supercapacitor (ASSC) was assembled using NCP-2/NF as cathode and GH as anode, with PVA-KOH gel as separator. The mass ratio of cathode to anode was 4.4 based on the charge balance equation ($q^+ = q^-$). The PVA-KOH gel was fabricated as follows: 3.0 g PVA was added into 30 mL DI water and stirred at 90°C until PVA dissolve completely. Then, 5 mL KOH (2 g) solution was added into PVA solution dropwise under continuous stirring. After cooling down, cathode and anode electrodes were soaked into PVA-KOH sol for 30 min and then put into the vacuum oven for 1 h under ambident temperature to ensure complete penetration of electrolyte. After dried, the ASSC was obtained by wrapping with a tape.

6.3.3 Fabrication of porous PDMS/graphene composite

CMC (0.5 g) was firstly dissolved in 10 mL DI water under continuous magnetic stirring for about 15 min to form a clear and viscous solution. Then 0.8 g graphene powder was added into the CMC solution. After the full mixing by the mixing and defoaming machine under 2000 rpm for 15 min, graphene powders were dispersed in CMC uniformly. Then, the mixture was transferred to the high-shear dispersing machine (FS400-S, LICHEN Co., Ltd) under the stirring speed of 2000 rpm. Then 0.2 mL n-Octanol was dipped into the mixture dropwise under stirring. After the addition of n-Octanol, continue stirring for 15 min under 2000 rpm. The PDMS matrix Sylgard 184 (9 g) and curing agent (0.9 g) with a ratio of 10:1 was fully mixed by the mixing

and defoaming machine under 1000 rpm for 5 min. Then the prepared PDMS solution was added into the CMC/graphene composite slowly with a stirring speed of 200 rpm. After addition of PDMS, the mixture was further stirred for 15 min under 2000 rpm. Then the mixture was deformed by the mixing and defoaming machine under 1000 rpm for 5 min. Then the mixture was poured into a PTFE mold with the dimension of 20 mm × 20 mm × 2 mm. After curing at 60ºC for 12 h, PDMS/graphene with isolated pores was obtained. Then, after soaking the PDMS/graphene in concentrated KOH solution for 2 h under 60ºC, PDMS/graphene with connected pores was obtained and it can be used for piezoresistive sensors.

Electrospinning TPU films are as protective layers to assemble the sensor. It is prepared by dissolving 4 wt% TPU in 1,1,1,3,3,3-Hexafluoro-2-propanol with a positive voltage of 10 kV and a negative voltage of 2 kV. The TPU film was cut into 2 × 2 cm^2 for further use. The pattern of the electrode (interdigital shape) was design using CorelDRAW software. A laser cutting machine (4060, FST) was used to engrave the conductive fabric tape to the predesigned pattern.

6.4 Characterization of GH electrode

Graphene hydrogel is the most common negative electrode for supercapacitor because it can exhibit stable electrochemical performance under various aqueous electrolyte such as acid (H_2SO_4), alkaline (KOH) and neutral electrolyte (Na_2SO_4). It can work well in the voltage windows of 0 - -1 V. Furthermore, the porous structure, large specific surface area, and suitable pore size make it an ideal choice for SC materials.

GH can be effortlessly fabricated through the one-step hydrothermal reduction process

of GO aqueous dispersion. The inset of Fig. 6.1a shows the optical images of GH from side view. The GH exhibits perfect cylinder shape due to the self-assembling of graphene sheets during the reduction process. The repaired conjugated structure of GO sheets during the hydrothermal reduction process can induce the partial overlapping or coalescing of graphene sheets with flexibility through the strong π-π stacking interactions, leading to the strong crosslinks of the 3D graphene network.

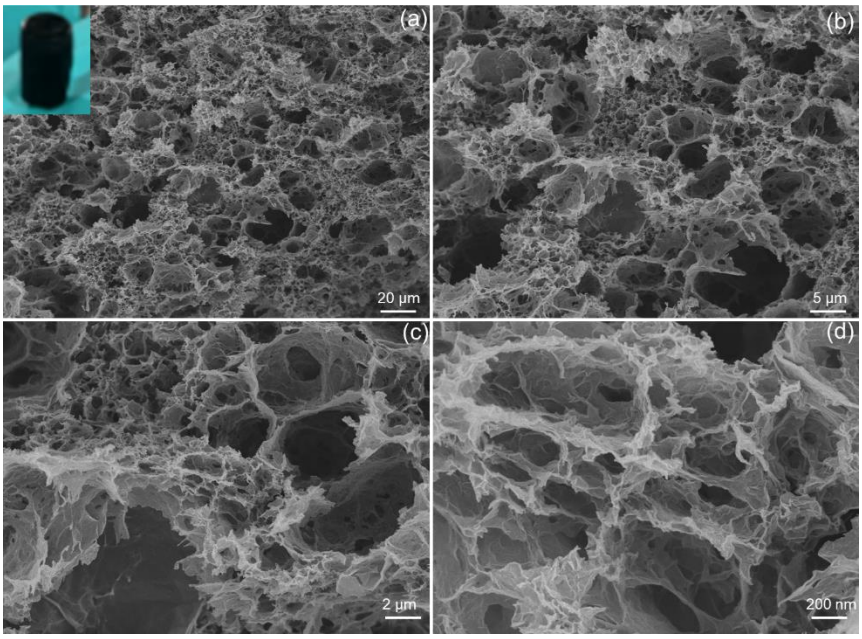

Fig. 6.1 SEM images of GH at low (a) and (b) high magnification. Inset of (a) is the optical image of the prepared GH sample. SEM images of (c) micropores and (d) submicropores.

The crosslinked porous structure of freeze-dried GH was further observed by SEM as shown in Fig. 6.1a and 1b and the pore sizes ranged from submicrometer (Fig. 6.1d) to several micrometers (Fig. 6.1c). This unique porous and crosslinked structure can effectively alleviate the restack of graphene nanosheets and provide large surface area for the adsorption of charged ions, thus leading to large capacity.

Then, Raman measurements was employed to identify the degree of reduction of GH.

The Raman spectra of GO and GH collected in the range of 800 – 2000 cm^{-1} with a laser operating at 532 nm are shown in Fig. 6.2. There are two obvious peaks at 1350 and 1580 cm^{-1}, corresponding to the D band and G band of graphene. G bond is the characteristic peak of C with sp^2 hybridization, which reflects the symmetry and crystallization degree of graphite. D bond is related to the structural defects or disorder of graphitized region.[194] The I_D/I_G value of GO is 1.03, and the value is 1.64 for GH, indicating the repair or reduction of the oxidation region in GO lamina, which can form some small conjugate region.[195]

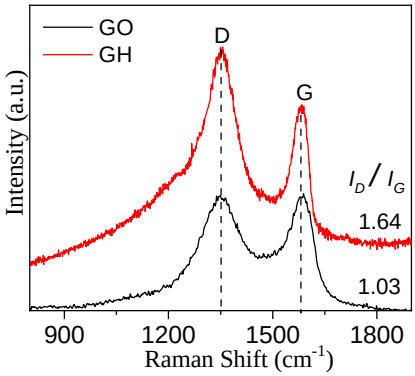

Fig. 6.2 Raman spectra of GO and GH.

The reduction of GO can also be confirmed by the XPS spectra. The survey spectra of GO and GH can be found in Fig. 6.3a and 3b. For both two samples, there only exist C and O elements. And the C and O contents for GO are 68.24% and 31.76%, respectively. After hydrothermal reduction, the C and O contents changes to 84.01% and 15.99%, respectively. The increase of the relative contents of C indicates the reduction of GO during the hydrothermal process. To further analysis the groups of GO and GH, the high-resolution C 1s spectra of GO and GH are measured as shown in Fig. 6.3c and 3d. They all consist of three deconvoluted component peaks, which can be attributed to C-

C/C=C (284.6 eV), C-O (287.2 eV), and C=O (289.4 eV) species, respectively.[196] The relatively low peak intensities of oxygen-containing groups for GH suggest that GO is effectively reduced during hydrothermal process.

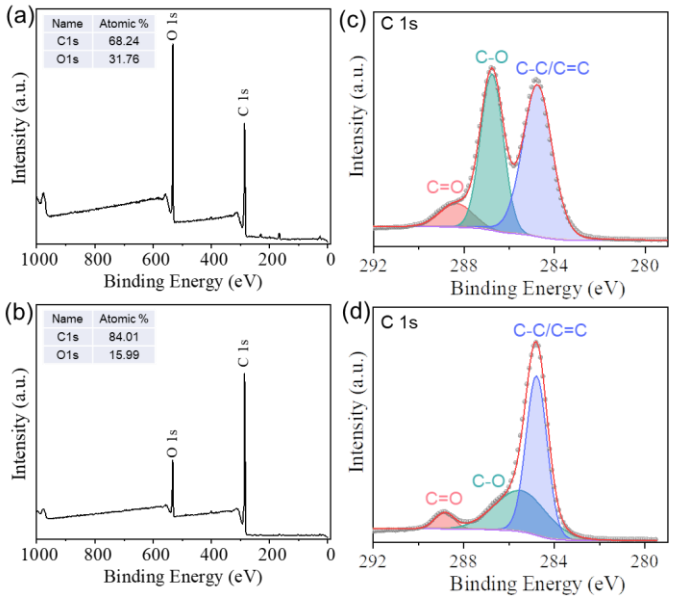

Fig. 6.3 XPS spectra of GO and GH. Survey spectrum of (a) GO and (b) GH. High resolution C 1s spectra of (c) GO and (d) GH.

It is anticipated that the as-prepared GH has favorable electrochemical performance acting as supercapacitors electrode materials. The capacitance of GH was firstly measured in a conventional three-electrode system with 1 M KOH aqueous electrolytes. The CV curves of GH show wide reversible small humps as shown in Fig. 6.4a, which may be attributed to the faradic reaction arising from the oxygen-containing groups on the surface of graphene. The CV curves of GH under various scan rates can keep the similar shapes only with a slightly distortion, suggesting GH possesses a high degree of reversibility, prominent charge propagation and favorable rate performance. To assess the capacitance performance of GH further accurately, GCD measurement was carried out under different current densities with the same conditions as in Fig. 6.4b.

The GCD curves of GH are in a slightly distorted asymmetric triangular shape due to its surface hydrophobic performance. The specific capacitance of GH calculated based on the discharge curves under various current densities is displayed in Fig. 6.4c. GH exhibits a high galvanostatic specific capacitance up to 227 F g^{-1} at a current density of 1.67 A g^{-1} due to its large specific surface area. Moreover, GH also exhibits remarkable rate performance, with high specific capacitance of 160 F g^{-1} maintained at high current densities of 41.67 A g^{-1}.

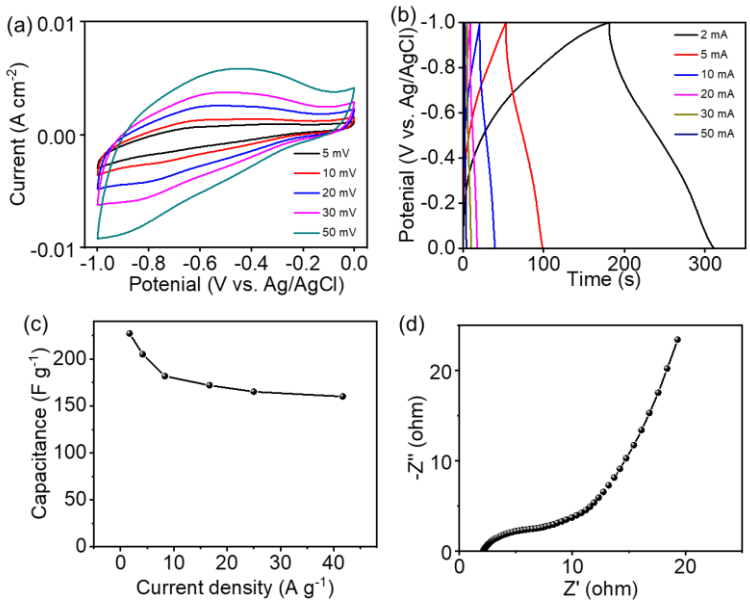

Fig. 6.4 Electrochemical performance of GH. (a) CV curves under various scan rates; (b) GCD curves at different current density; (c) specific capacitance at different current density; (d) EIS within the frequency of 10^5 – 0.01 Hz with the amplitude of 5 mV.

Fig. 6.4d displays the Nyquist plot of GH measured in the frequency of 10^5 - 0.01 Hz with the amplitude of 5 mV. The slope at low frequency seems nearly vertical, indicating its good ion diffusion behavior and the easy formation of electric double layers. In high-frequency range, the GH electrode exhibits small semicircle and low equivalent series resistance, indicting its low charge transfer resistance and exceptional

electronic conductivity.

6.5 Electrochemical performance of asymmetric supercapacitor

The asymmetric all solid-state supercapacitor (ASSC) devices have attracted enormous attention for their application in the field of portable electronic devices due to their lightweight, miniature, wide operation windows and shape diversity. To further investigate the capacitive performance of NCP-2 electrode in the practical supercapacitor cell, ASSC device was fabricated with NCP-2/NF electrode as positive electrode and GH/carbon cloth as negative electrode as shown in Fig. 6.5a.

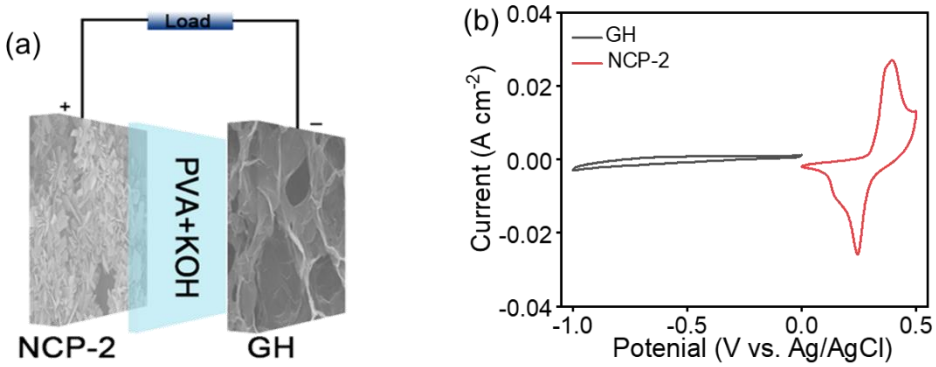

Fig. 6.5 (a) Illustration of assembled NCP-2//GH ASSC; (b) CVs of the GH and NCP-2 electrodes measured at 5 mV s^{-1} in a three-electrode system.

To achieve superior electrochemical performance with high capacity, the mass ratios of NCP-2 and GH was determined by charge balance as displayed in equitation (2.5). According to the three electrode measurements, NCP-2 and GH electrodes work in separated potential window with different polarity, which is beneficial for enlarging the potential window of the ASSC device. The NCP-2 electrode exhibits prominent electrochemical performance in positive potential window within 0 - 0.5 V (vs Ag/AgCl) and GH electrode works in negative potential window within -1 - 0 V (vs Ag/AgCl), as

shown in Fig. 6.5b.

The working window of NCP-2//GH ASSC device was optimized within the range of 0 to 1.0 - 1.6 V as displayed in Fig. 6.6 a. The quasi-rectangular shaped CV curves with negligible redox peaks are obtained even at the voltage window of 0 - 1.5 V. When the working window expands to 1.6 V, the current increases suddenly owing to the oxygen reaction of water at 1.6 V, resulting in the irreversible destroy of electrode. Therefore, 0 to 1.5 V voltage window is suitable for electrochemical measurement. The GCD curves of NCP-2//GH ASSC device in various potential windows at the same current density of 0.5 A g^{-1} are provided in Fig. 6.6b. Similar to the CV analysis above, the GCD curves show stable charge-discharge curves within the potential range of 0 - 1.5 V by displaying nearly symmetric shapes. It is obvious that the CV curves of ASSC device displays stable capacitive performance without noticeable distortion at the voltage window of 1.5 V and the large operation window is essential for the improvement of energy density.

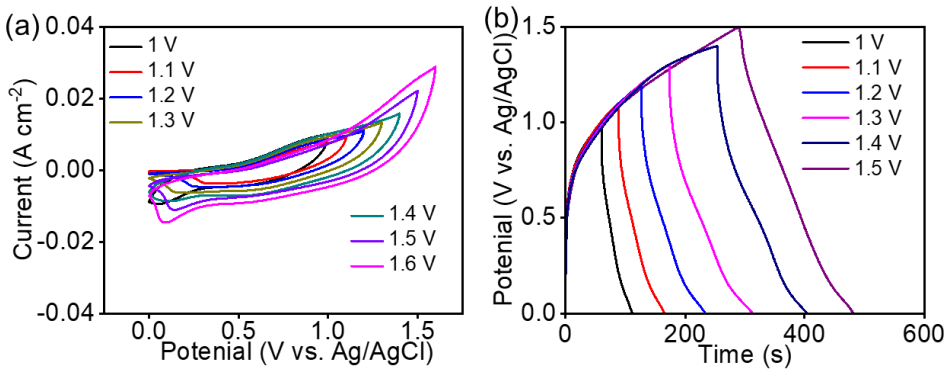

Fig. 6.6 (a) The CV curves and (b) GCD curves of NCP-2//GH ASSC device under various potential windows.

CV curves of NCP-2//GH ASSC within 0 - 1.5 V under various scan rates were collected as shown in Fig. 6.7a. All CV curves exhibit wide and small reduction peaks

without obvious redox peaks because of the two-electrode construction. The curve shape presents invisible distortion even under the scan rate of 50 mV s^{-1}, indicating its rapid current response with the change of voltage and favorable capacitive performance. Similarly, the GCD curves in Fig. 6.7b of the ASSC device tend toward quasi-triangular shape without visible voltage plateau along with the increase of charge-discharge current density, suggesting its reversible electrochemical behavior. The IR drop of NCP-2//GH ASSC device seems negligible in GCD curves, implying the low internal resistance of the assembled device.

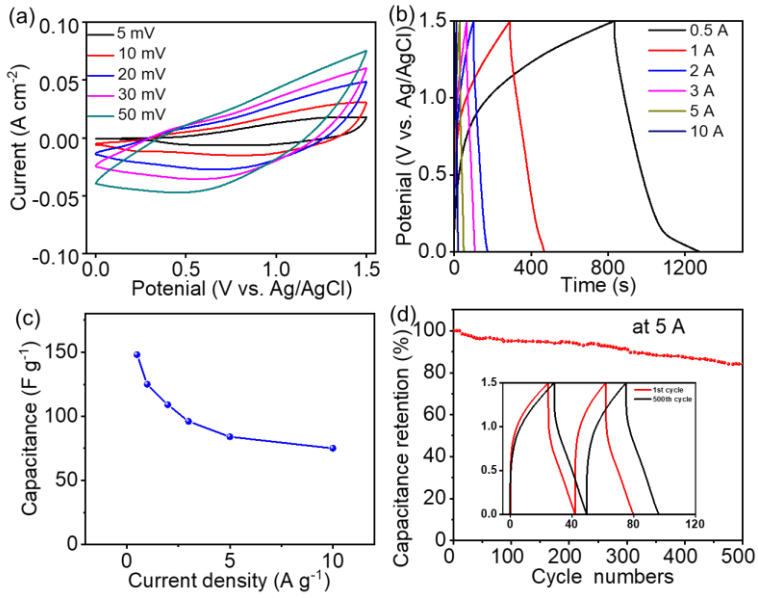

Fig. 6.7 Electrochemical measurement of NCP-2//GH ASSC device. (a) CV curves at different scan rates within 0 - 1.5 V; (b) the GCD curves at various current densities; (c) specific capacitance under various current density; (d) long-term cycling stability of the NCP-2//GH ASSC device at 5 A g^{-1}, and the inset shows the GCD curves of the first two and last two cycles.

The C_s (F g^{-1}) calculated based on GCD curves under various current density is plotted in Fig. 6.7c. The NCP-2//GH ASSC device can achieve a C_s of 148 F g^{-1} at the current density of 0.5 A g^{-1}, and 50.1% of its initial capacitance retained at the current density

of 10 A g^{-1}, revealing the commendable rate performance and decent power density. The long-term stability of the NCP-2//GH ASSC device was evaluated by GCD measurement under 5 A g^{-1}. The shapes of the charge-discharge curves are well maintained without obvious distortion through assessing the GCD curves of the first two cycles and the last two cycles as shown in the inset of Fig. 6.7d. After 500 charge-discharge cycles, 80.2% of the initial capacitance can be retained, suggesting its excellent cycling stability.

To further understand the electrochemical kinetics of the NCP-2//GH ASSC device, EIS measurement was carried in the frequency of 10^5 to 0.01 Hz with an open amplitude of 5 mV as shown in Fig. 6.8a. At initial state, the R_s of ASSC device is 2.3 Ω and the R_{ct} is 0.3 Ω, reflecting the low internal resistance and fast charge transfer kinetics of the ASSC device. After 500 cycles, the R_s increase to 3 Ω and the R_{ct} change to 0.7 Ω. The increase of the internal resistance and charge transfer resistance may be responsible for the capacity decay of the ASSC device. Energy density and power density are two pivotal factors to estimate the energy storage property of ASSC devices for practical application. The Ragon plots of the ASSC devices depicted in Fig. 6.8b calculated based on the GCD results. The NCP-2//GH ASSC device can achieve a maximum energy density of 46.25 Wh kg^{-1} at a relatively low power density of 105 W kg^{-1}, and still maintain the energy density of 23.44 Wh kg^{-1} even at the high power density of 2905 W kg^{-1}.

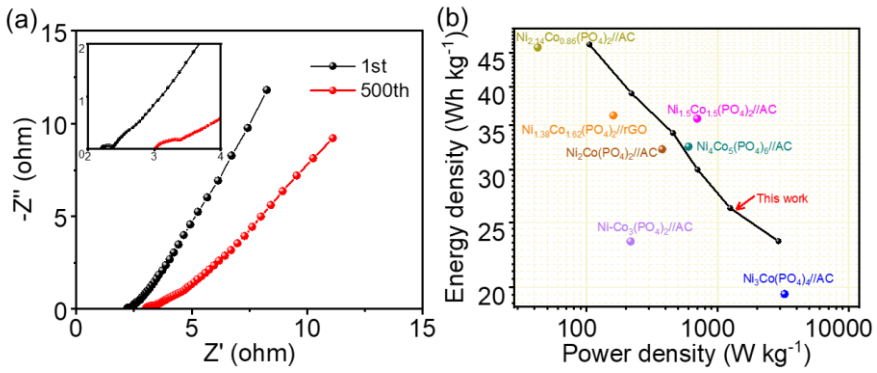

Fig. 6.8 (a) Nyquist plots in the frequency of 10^5-0.01 HZ; (b) Ragone plots of the ASSC device compared with other related studies.

The energy density and power density are competitive to those of previously reported nickel cobalt phosphate based asymmetric supercapacitor as plotted in Fig. 6.8b [159-161, 163-165, 184]. The enhanced energy performance may arise from the high capacity of NCP-2 electrode and the open flower-like structure ensure the high power density.

The flexibility of the ASSC device is also evaluated by measuring the CV and CGD curves of the device under various bending states. The results can be found in Fig. 6.9. The optical photos of the ASSC device under various bending states are displayed in the inset of Fig. 6.9a.

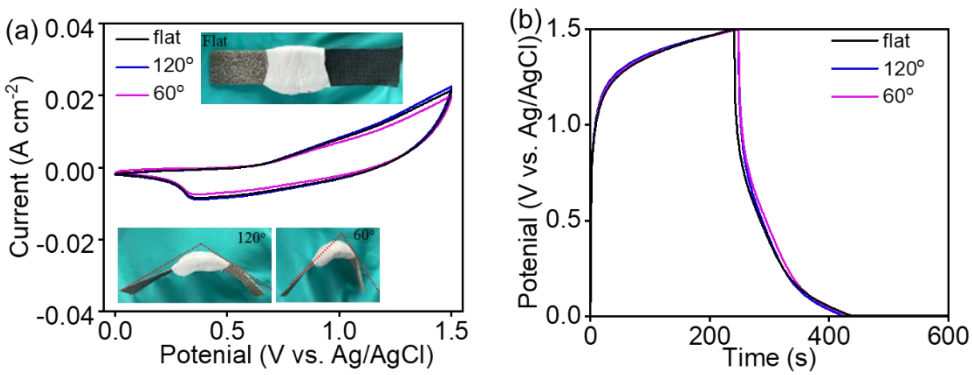

Fig.6.9 Electrochemical performance of ASSC device under bending state. (a) CV curves at 5 mV s^{-1}; (b) GCD curves under 1 A g^{-1}.

It is clear that the CV curves can maintain the similar shapes without obvious distortion under various bending angels, indicating its potential application for flexible electronic devices. The GCD curves of the ASSC device of different bending angels are exhibited similar quasi-triangle shapes without any distortion, suggesting it can charge-discharge under bending state.

6.6 Application of the asymmetric supercapacitor

6.6.1 Electric supply for powering small electronics

To confirm the practical application of the NCP-2//GH ASSC device further visually, four ASSC devices are connected in series and connect with the energy-converting station. The schematic of the integrated energy-converting station is demonstrated in Fig. 6.10a. It is manufactured by assembling miniature DC generator (nominal voltage of 1.5 -3 V, no-load current of 130 mA, no-load speed of 3000 rpm) and motor (nominal voltage of 3 V, no-load current of 150 mA, no-load speed of 9000 rpm) with a fan, four ASSC devices connected in series, an automatic switch, and a red LED light (3.0 V, 20 mA). Generally, the integrated station can convert chemical energy from the ASSC device into mechanical energy to drive the rotation of the fan, then mechanical energy arising from the rotation of fan can finally transfer into electrical energy to light up the red LED light as shown in Fig. 6.10b. This energy conversion process further confirms the potential application of NCP-2//AC ASSC device.

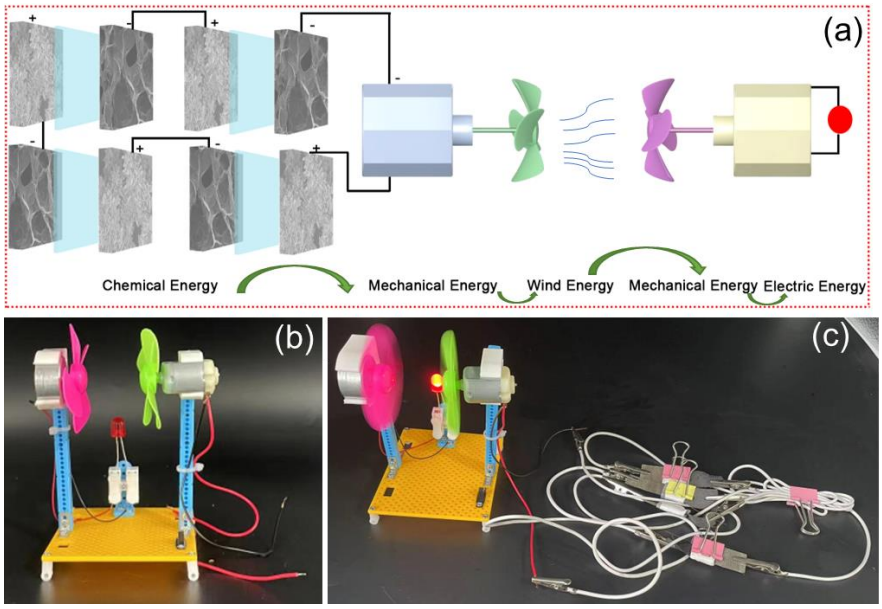

Fig. 6.10 (a) Schematic demonstration of the energy conversion station composed of a generator, a motor, a LED, and four ASSC devices connected in series, which provide chemical energy. (b) Digital photo of the energy conversion station. (c) Digital photo of the red LED lighted up by the energy conversion station.

To explore the practical application of the ASSC device, "UNNC (University of Nottingham, Ningbo, China)" composed of 33 blue LED lights (3.0 V, 20 mA) in series with the nominal voltage of 3 V was lit by four ASSC devices in series. The ASSC devices are fully-charged firstly with the current density of 1 A g^{-1}. The LED lights in series can be lit easily and continuously illuminated for over 5 min, as exhibited in Fig. 6.11, suggesting the extraordinarily high energy density of the device and revealing its promising application prospects.

Fig. 6.11 Digital photos of the character of "UNNC" composed of 33 blue LED light driven by four ASSC devices connected in series.

6.6.2 Electric supply for piezoresistive sensor

Flexible piezoresistive sensors can transduce tactile information into electric signals. It is widely applied in various applications such as health monitoring, human-machine interfaces and robotics owing to its low energy consumption, easy fabrication, and simple signal acquisition.[197] The main strategy to improve the sensitivity and linearity of piezoresistive sensors is to introduce micro/nano structure. For the measurement of electrical signals, external voltage source is usually needed. Supercapacitor can discharge for a long time with voltage plateau, so it is suitable to provide voltage supply for piezoresistive sensors.

We fabricated a porous PDMS/graphene composite as described in experimental section. The SEM images are shown in Fig. 6.12. Fig. 6.12a-c show the morphology of cured PDMS/graphene without the remove of CMC. There exist numerous pores with similar size of ~50 μm and these pores are arising from the evaporation of water during the curing process. The pores are insulated with each other, and graphene nanosheets disperse on the PDMS matrix uniformly.

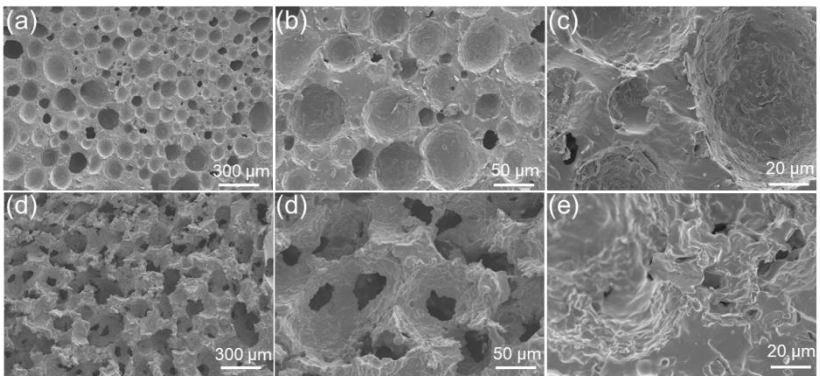

Fig. 6.12 SEM images of porous PDMS/graphene composite. (a-c) Cured PDMS/graphene composite. (d-e) PDMS/graphene composite after KOH soaking.

After soaking the cured PDMS/graphene composites into hot KOH solution, CMC in

the composite was removed completely. There exists hierarchical porous structure in the composite, including pores arising from water evaporation and pores attributed to the remove of CMC. The pores connect with each other to form continuous conductive pathway, which is favorable for piezoresistive measurement.

The piezoresistive device was assembled by combining electrospinning TPU film as protective layers, porous PDMS/graphene as piezoresistive layer and conductive fabric tapes with interdigital shape as electrodes. With a fully charged NCP-2//AC ASSC device as the voltage supply, the piezoresistive performance of porous PDMS/graphene are measured under various pressure as shown in Fig. 6.13.

It can be found that with NCP-2//AC ASSC device as electric supply, the sensor can generate steady responses under various pressure from 10 kPa to 300 kPa. The electric signals seem similar during the measurement cycles. Also, with fixed pressure of 50 kPa, the sensor can maintain stable electric signal for a while, suggesting the practical application of the ASSC device in powering piezoresistive sensors.

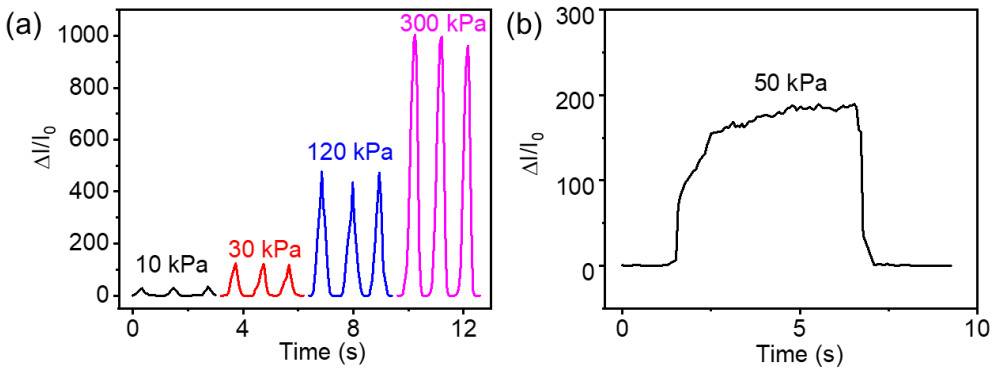

Fig. 6.13 Electrical measurement of sensor with ASSC as electric supply. (a) Dynamic response of sensor under various pressure; (b) Current-voltage curves of sensor under certain pressure with a long time.

6.6.3 Self-charging system

Considering the wearability of the fabricated TENG device in chapter 4 and the flexibility of ASSC device in this chapter, they can be integrated into one individual device as shown in Fig. 6.14a. It demonstrates the viability of the self-charging power insole by combining a supercapacitor device into the hell of the insole shaped TENG device with a rectifier as the bridge. Though the rectifier is not flexible, it is conceivable to design it into either a logo or a button of the shoes owing to its small size (~0.5 × 0.5 cm^2).

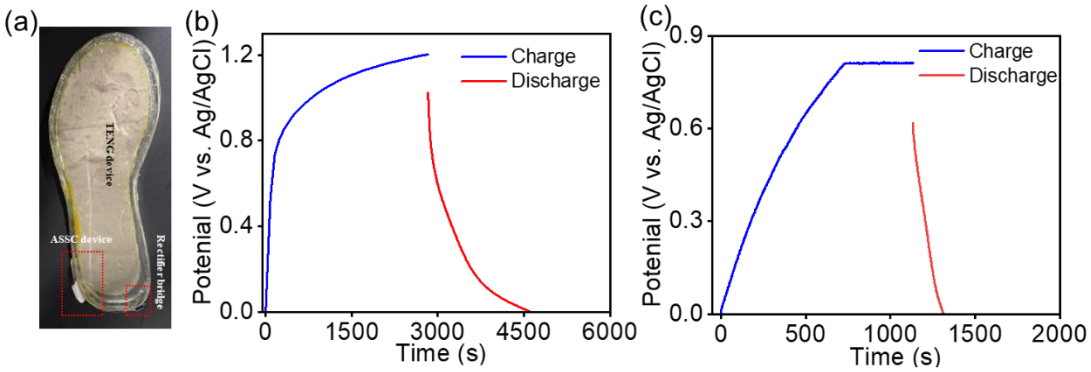

Fig. 6.14 (a) The optical photograph of the self-charging system. The voltage profile of ASSC device charged (b) by the TENG with the dimension of 5 × 5 cm^2 at the frequencies of 5 Hz and discharged at 1 μA; (c) by insole shaped TENG under walking and discharged at 1 μA.

The supercapacitor was charged by the TENG device under contact-separation mode with the frequency of 5 Hz firstly. The flexible NCP-2//AC ASSC device can be charged by the TENG device (5 × 5 cm^2) to 1.2 V in 3000 s as shown in Fig. 6.14b. The charged supercapacitor later can be galvanostatically discharged at 1 μA for 1500 s, further confirming the validity of our self-charging power insoles. When using the insole shaped TENG device with the working frequency of ~1 Hz, the ASSC device can be charged to 0.8 V in 750 s, and the following discharge at 1 μA is ~200 s. It should be

noted that further improvement in the charging efficiencies can be achieved by obtaining impedance matching between the TENG and supercapacitors, since the internal impedance of the TENG is generally several orders higher than that of energy-storing devices.

6.7 Conclusion

In conclusion, the fabricated ASSC device with NCP-2 as the positive electrode and the GH as the negative electrode can achieve a high energy density of 46.25 W h kg^{-1} and a high power density of 2905 W kg^{-1}. The ASSC device also show comparable cycling stability. For the practical application, four ASSC devices in series can drive the energy conversion station and lit up 33 LED lights for over 5 min, reflecting the high energy density and excellent endurance, confirming the practicality of nickel cobalt phosphate applied in energy storage devices. Also, the ASSC device can be used as the power supply for piezoresistive sensor. By combining the ASSC device with the insole shaped TENG device, the self-charging system can be achieved. It can convert machinal energy into electricity and the electricity can be stored in the ASSC device, indicating its potential application in wearable electronics.

Chapter 7 Conclusion and future work

This chapter summarizes the main conclusion of this thesis and proposes the direction for further improvement.

7.1 Conclusion

In this thesis, the self-charging system consists of TENG as energy harvest part and SC as energy storage part is fabricated, which can harvest mechanical energy from human motions and stored the generated electrical energy. To avoid the frequent charging of SC, TENG with high electric outputs and SC with high capacity are fabricated. Details are as follow:

(1) PU friction layer with microstructures is fabricated by the maskless DIL method. To further enlarge the electron affinity of friction layers, F-PU layer is obtained through chemical modification with FOTS vapor. Meanwhile, the contact area further increases owing to roughened morphology in micro-nanoscale on the F-PU surface. The TENG device composed of PU and F-PU layer with microstructure can achieve the high current output of 22 μA and a maximum output power density of 1.5 W/m^2 with excellent cycling stability.

(2) The origin of the high-performance TENG is studied by surface morphology observation and chemical composition analysis. The improved electric outputs originate from the synergistic effect of microcones, fluorination and roughened surface.

(3) Due to the programmability and customizability of the DIL technology, TENG devices with different shapes can be fabricated rapidly. The fabricated TENG can

harvest mechanical energy from various human motion. Also, with the TENG device as energy supply, Cu_2O nanowire as the sterilization electrode, the enhanced self-powered sterilization efficiency can be achieved.

(4) Hydrothermal stirring approach was firstly used to directly grow nickel cobalt phosphate on nickel foam. The optimized $Ni_2Co(PO_4)_3$ electrode with one third of the Ni sites replaced by Co reveals the morphography of tassels-like structure composed with ultrathin nanosheets, which are beneficial for the ion penetration and electron transportation. The electrode demonstrates the maximum specific capacity of 2518 mC cm^{-2} (1007 C g^{-1}) at 2 mA cm^{-2} and remains 76.7% of the initial capacity at 50 mA cm^{-2}. The DFT calculation results indicate improved electrochemical property by the insertion of Co atoms.

(5) Asymmetrical supercapacitor device with $Ni_2Co(PO_4)_2$ as positive electrode and graphene hydrogel as negative electrode delivers a high energy density of 46.25 W h kg-1 and a high power density of 7745 W kg^{-1}. The ASSC device shows excellent flexibility, which is suitable for wearable electronics. The ASSC device can be applied as energy supply for piezoresistive sensor, LED lights and energy conversion station. Also, the self-charging system is constructed by integrating the ASSC with insole shaped TENG. By continuous walking, the SC can be charged to 1.2 V in a short time.

7.2 Future work

In this thesis, we constructed the self-charging system consists of high-performance TENG and ASSC device with high capacity. Despite these achievements, the self-

charging system in this thesis is still a proof-of-concept prototype. Further studies are urgently needed to make it applicable for scaled-up fabrication and are feasible for practical applications.

(1) The piezoresistive sensor has a special porous structure and shows favorable piezoresistive property. The sizes of the pores can be tuned by changing the ratios and amounts of water and CMC. In the future, PDMS/graphene with different porous structure can be fabricated and their piezoresistive performance can be investigated.

(2) The improvement of the system efficiency is of great importance. The impedance mismatch between TENG devices and ASSC devices may cause the low energy transfer efficiency. Design power management circuits to lower the impedance of the TENG and choose appropriate supercapacitor systems should be studied further.

(3) Harvesting multiple kinds of energy such as machinal energy, thermal and solar energy simultaneously is another research direction. Future work can focus on the multiple energy harvester by utilizing the mechanisms of piezoelectric, thermoelectric, and solar cells.

(4) The efficient suppression the self-charging of supercapacitors needs further investigated. The output power of TENG devices is always low, self-charging of supercapacitors can dramatically reduce the performance of the self-charging system. The leakage of electrolyte in supercapacitors also requires large efforts to avoid in the future.

(5) Developing self-charging systems with more superior flexibility is also a

meaningful and promising research direction for next-generation portable, wearable smart electronics.

References

[1] O. Schmidt, A. Hawkes, A. Gambhir, I. Staffell, The future cost of electrical energy storage based on experience rates, Nat. Energy, 2 (2017) 1-8.

[2] J. Huang, K. Yuan, Y.W. Chen, Wide voltage aqueous asymmetric supercapacitors: advances, strategies, and challenges, Adv. Funct. Mater., 32 (2022) 2108107.

[3] M. Gao, C. Peh, H. Phan, L. Zhu, G. Ho, Solar Absorber Gel: Localized Macro-Nano Heat Channeling for Efficient Plasmonic Au Nanoflowers Photothermic Vaporization and Triboelectric Generation, Adv. Energy Mater., 8 (2018) 1800711.

[4] T. Ackermann, L. Soder, Wind energy technology and current status: a review, Renew. Sust. Energ. Rev., 4 (2000) 315-374.

[5] G. Xue, Y. Xu, T. Ding, J. Li, J. Yin, W. Fei, Y. Cao, J. Yu, L. Yuan, L. Gong, J. Chen, S. Deng, J. Zhou, W. Guo, Water-evaporation-induced electricity with nanostructured carbon materials, Nat. Nanotechnol., 12 (2017) 317-321.

[6] A. Yu, Y. Zhu, W. Wang, J. Zhai, Progress in Triboelectric Materials: Toward High Performance and Widespread Applications, Adv. Funct. Mater., 29 (2019) 1900098.

[7] C. Wu, A. Wang, W. Ding, H.Guo, Z. Wang, Triboelectric Nanogenerator: A Foundation of the Energy for the New Era, Adv. Energy Mater., 9 (2019) 1802906.

[8] L. Zhang, B. Zhang, J. Chen, L. Jin, W. Deng, J. Tang, H. Zhang, H. Pan, M. Zhu, W. Yang, Z.L. Wang, Lawn Structured Triboelectric Nanogenerators for Scavenging Sweeping Wind Energy on Rooftops, Adv. Mater., 28 (2016) 1650-1656.

[9] P. Cui, J. Wang, J. Xiong, S. Li, W. Zhang, X. Liu, G. Gu, J. Guo, B. Zhang, G. Cheng, Z. Du, Meter-scale fabrication of water-driven triboelectric nanogenerator based on in-situ grown layered double hydroxides through a bottom-up approach, Nano Energy, 71 (2020) 104646.

[10] B. Chen, W. Tang, C. He, C. Deng, L. Yang, L. Zhu, J. Chen, J. Shao, L. Liu, Z.L. Wang, Water wave energy harvesting and self-powered liquid-surface fluctuation sensing based on bionic-jellyfish triboelectric nanogenerator, Mater. Today, 21

(2018) 88-97.

[11] Z. Lin, Z. Wu, B. Zhang, Y. Wang, H. Guo, G. Liu, C. Chen, Y. Chen, J. Yang, Z.L. Wang, A Triboelectric Nanogenerator-Based Smart Insole for Multifunctional Gait Monitoring, Adv. Mater. Technol., 4 (2019) 1800360.

[12] Z. Lin, J. Chen, X. Li, Z. Zhou, K. Meng, W. Wei, J. Yang, Z.L. Wang, Triboelectric Nanogenerator Enabled Body Sensor Network for Self-Powered Human Heart-Rate Monitoring, ACS Nano, 11 (2017) 8830-8837.

[13] W. Qiu, Y. Feng, N. Luo, S. Chen, D. Wang, Sandwich-like sound-driven triboelectric nanogenerator for energy harvesting and electrochromic based on Cu foam, Nano Energy, 70 (2020) 104543.

[14] X. Shi, S. Chen, H. Zhang, J. Jiang, Z. Ma, S. Gong, Portable Self-Charging Power System via Integration of a Flexible Paper-Based Triboelectric Nanogenerator and Supercapacitor, ACS Sustain. Chem. Eng., 7 (2019) 18657-18666.

[15] Q. Zhang, Q. Liang, Q. Liao, M. Ma, F. Gao, X. Zhao, Y. Song, L. Song, X. Xun, Y. Zhang, An Amphiphobic Hydraulic Triboelectric Nanogenerator for a Self-Cleaning and Self-Charging Power System, Adv. Funct. Mater., 28 (2018) 1803117.

[16] B. Frfa, B. Zqt, L. Zhong, Flexible triboelectric generator, Nano Energy, 1 (2012) 328-334.

[17] Z.L. Wang, T. Jiang, L. Xu, Toward the blue energy dream by triboelectric nanogenerator networks, Nano Energy, 39 (2017) 9-23.

[18] Z. Wang, On Maxwell's displacement current for energy and sensors: the origin of nanogenerators, Mater. Today, 20 (2017) 74-82.

[19] S. Niu, S. Wang, L. Lin, Y. Liu, Y. Zhou, Y. Hu, Z.L. Wang, Theoretical study of contact-mode triboelectric nanogenerators as an effective power source, Energy. Environ. Sci., 6 (2013) 3576-3583.

[20] T. Jiang, X. Chen, C. Han, W. Tang, Z.L. Wang, Theoretical Study of Rotary Freestanding Triboelectric Nanogenerators, Adv. Funct. Mater., 25 (2015) 2928-

2938.

[21] S. Niu, Y. Liu, S. Wang, L. Lin, Y. Zhou, Y. Hu, Z.L. Wang, Theory of sliding-mode triboelectric nanogenerators, Adv. Mater., 25 (2013) 6184-6193.

[22] X. Cheng, Y. Zi, A. Wang, H. Zou, Y. Dai, H. Xu, P. Wang, Y. Wang, P. Feng, D. Li, On the Electron-Transfer Mechanism in the Contact-Electrification Effect, Adv. Mater., 30 (2018) 1706790.

[23] Z.L. Wang, J. Chen, L. Lin, Progress in triboelectric nanogenerators as a new energy technology and self-powered sensors, Energy Environ. Sci., 8 (2015) 2250-2282.

[24] S. Wang, L. Lin, Z.L. Wang, Nanoscale triboelectric-effect-enabled energy conversion for sustainably powering portable electronics, Nano Lett., 12 (2012) 6339-46.

[25] P. Ba I, G. Zhu, Y. Liu, J. Chen, Q. Jing, W. Yang, J. Ma, G. Zhang, Z.L. Wang, Cylindrical Rotating Triboelectric Nanogenerator, ACS Nano, 7 (2013) 6361-6366.

[26] F. Fan, L. Lin, G. Zhu, W. Wu, R. Zhang, Z.L. Wang, Transparent triboelectric nanogenerators and self-powered pressure sensors based on micropatterned plastic films, Nano Lett., 12 (2012) 3109-3114.

[27] J. Chen, G. Zhu, W. Yang, Q. Jing, P. Bai, Y. Yang, T.C. Hou, Z.L. Wang, Harmonic-resonator-based triboelectric nanogenerator as a sustainable power source and a self-powered active vibration sensor, Adv. Mater., 25 (2013) 6094-6099.

[28] G. Zhu, P. Bai, J. Chen, Z.L. Wang, Power-generating shoe insole based on triboelectric nanogenerators for self-powered consumer electronics, Nano Energy, 2 (2013) 688-692.

[29] W. Yang, J. Chen, G. Zhu, J. Yang, P. Bai, Y. Su, Q. Jing, X. Cao, Z.L. Wang, Harvesting energy from the natural vibration of human walking, ACS Nano, 7 (2013) 11317-11324.

[30] J. Zhong, Q. Zhong, F. Fan, Y. Zhang, S. Wang, B. Hu, Z. Wang, J. Zhou, Finger

typing driven triboelectric nanogenerator and its use for instantaneously lighting up LEDs, Nano Energy, 2 (2013) 491-497.

[31] X. Zhang, M. Han, R. Wang, F. Zhu, Z. Li, W. Wang, H. Zhang, Frequency-multiplication high-output triboelectric nanogenerator for sustainably powering biomedical microsystems, Nano Lett., 13 (2013) 1168-1172.

[32] L. Lin, Y. Xie, S. Wang, W. Wu, S. Niu, X. Wen, Z.L. Wang, Triboelectric active sensor array for self-powered static and dynamic pressure detection and tactile imaging, ACS Nano, 7 (2013) 8266-8274.

[33] X. Fan, J. Chen, J. Yang, P. Bai, Z. Li, Z.L. Wang, Ultrathin, rollable, paper-based triboelectric nanogenerator for acoustic energy harvesting and self-powered sound recording, ACS Nano, 9 (2015) 4236-4243.

[34] L. Lin, S. Wang, Y. Xie, Q. Jing, S. Niu, Y. Hu, Z. Wang, Segmentally structured disk triboelectric nanogenerator for harvesting rotational mechanical energy, Nano Lett., 13 (2013) 2916-2923.

[35] G. Zhu, S.Z. Yu, B. Peng, S.M. Xian, Q. Jing, J. Chen, L.W. Zhong, A Shape-Adaptive Thin-Film-Based Approach for 50% High-Efficiency Energy Generation Through Micro-Grating Sliding Electrification, Adv. Mater., 26 (2014) 3788-3796.

[36] G. Zhu, J. Chen, Y. Liu, P. Bai, Y.S. Zhou, Q. Jing, C. Pan, Z. Wang, Linear-grating triboelectric generator based on sliding electrification, Nano Lett., 13 (2013) 2282-2289.

[37] G. Zhu, J. Chen, T. Zhang, Q. Jing, Z.L. Wang, Radial-arrayed rotary electrification for high performance triboelectric generator, Nat. Commun., 5 (2014) 3426.

[38] Y. Xie, S. Wang, L. Lin, Q. Jing, Z.H. Lin, Rotary Triboelectric Nanogenerator Based on a Hybridized Mechanism for Harvesting Wind Energy, ACS Nano, 7 (2013) 7119-7125.

[39] Y. Xie, S. Wang, S. Niu, L. Lin, Q. Jing, Y. Su, Z. Wu, Z.L. Wang, Multi-layered disk triboelectric nanogenerator for harvesting hydropower, Nano Energy, 6 (2014) 129-136.

[40] Y. Yang, H. Zhang, J. Chen, Q. Jing, Y. Zhou, X. Wen, Z.L. Wang, Single-electrode-based sliding triboelectric nanogenerator for self-powered displacement vector sensor system, ACS Nano, 7 (2013) 7342-7351.

[41] S. Niu, Y. Liu, S. Wang, L. Lin, Y. Zhou, Y. Hu, Z.L. Wang, Theoretical Investigation and Structural Optimization of Single-Electrode Triboelectric Nanogenerators, Adv. Funct. Mater., 24 (2014) 3332-3340.

[42] Q. Zhong, J. Zhong, B. Hu, Q. Hu, J. Zhou, Z.L. Wang, A paper-based nanogenerator as a power source and active sensor, Energy Environ. Sci., 6 (2013) 1779-1784.

[43] Q. Liang, X. Yan, Y. Gu, K. Zhang, M. Liang, S. Lu, X. Zheng, Y. Zhang, Highly transparent triboelectric nanogenerator for harvesting water-related energy reinforced by antireflection coating, Sci. Rep., 5 (2015) 9080.

[44] H. Zhang, Y. Yang, X. Zhong, Y. Su, Y. Zhou, C. Hu, Z.L. Wang, Single-electrode-based rotating triboelectric nanogenerator for harvesting energy from tires, ACS Nano, 8 (2014) 680-689.

[45] Y. Yang, G. Zhu, H. Zhang, J. Chen, X. Zhong, Z. Lin, Y. Su, P. Bai, X. Wen, Z.L. Wang, Triboelectric Nanogenerator for Harvesting Wind Energy and as Self-Powered Wind Vector Sensor System, ACS Nano, 7 (2013) 9461-9468.

[46] Y. Wu, Q. Jing, J. Chen, P. Bai, J. Bai, G. Zhu, Y. Su, Z.L. Wang, A Self-Powered Angle Measurement Sensor Based on Triboelectric Nanogenerator, Adv. Funct. Mater., 25 (2015) 2166-2174.

[47] T. Quan, X. Wang, Z.L. Wang, Y. Yang, Hybridized Electromagnetic–Triboelectric Nanogenerator for a Self-Powered Electronic Watch, ACS Nano, 9 (2015) 12301-12310.

[48] L. Lin, Y. Xie, S. Niu, S. Wang, Z.L. Wang, Robust Triboelectric Nanogenerator Based on Rolling Electrification and Electrostatic Induction at an Instantaneous Energy Conversion Efficiency of ~55%, ACS Nano, 9 (2015) 922-930.

[49] H. Guo, Q. Leng, X. He, M. Wang, J. Chen, C. Hu, Y. Xi, A Triboelectric Generator

Based on Checker-Like Interdigital Electrodes with a Sandwiched PET Thin Film for Harvesting Sliding Energy in All Directions, Adv. Energy Mater., 5 (2015) 1400790.

[50] S. Wang, S. Niu, J. Yang, L. Lin, Z.L. Wang, Quantitative Measurements of Vibration Amplitude Using a Contact-Mode Freestanding Triboelectric Nanogenerator, ACS Nano, 8 (2014) 12004-12013.

[51] Q. Leng, L. Chen, H. Guo, J. Liu, G. Liu, C. Hu, Y. Xi, Harvesting heat energy from hot/cold water with a pyroelectric generator, J. Mater. Chem. A, 2 (2014) 11940-11947.

[52] S. Wang, Y. Xie, S. Niu, L. Lin, Z.L. Wang, Freestanding triboelectric-layer-based nanogenerators for harvesting energy from a moving object or human motion in contact and non-contact modes, Adv. Mater., 26 (2014) 2818-2824.

[53] Y. Hu, J. Yang, Q. Jing, S. Niu, W. Wu, Z.L. Wang, Triboelectric Nanogenerator Built on Suspended 3D Spiral Structure as Vibration and Positioning Sensor and Wave Energy Harvester, ACS Nano, 7 (2013) 10424-10432.

[54] C. Zhang, W. Tang, Y. Pang, C. Han, Z.L. Wang, Active micro-actuators for optical modulation based on a planar sliding triboelectric nanogenerator, Adv. Mater., 27 (2015) 719-726.

[55] H.J. Yoon, H. Ryu, S.W. Kim, Sustainable powering triboelectric nanogenerators: Approaches and the path towards efficient use, Nano Energy, 51 (2018) 270-285.

[56] H. Guo, M. Yeh, Y. Zi, Z. Wen, J. Chen, G. Liu, C. Hu, Z.L. Wang, Ultralight Cut-Paper-Based Self-Charging Power Unit for Self-Powered Portable Electronic and Medical Systems, ACS Nano, 11 (2017) 4475-4482.

[57] D. Kim, J. Viventi, J. Amsden, J. Xiao, L. Vigeland, S.K. Yun, J. Blanco, B. Panilaitis, E. Frechette, D. Contreras, Dissolvable films of silk fibroin for ultrathin conformal bio-integrated electronics, Nat. Mater. 9(2010) 511-517.

[58] G. Zhu, C. Pan, W. Guo, C. Chen, Y. Zhou, R. Yu, Z.L. Wang, Triboelectric-generator-driven pulse electrodeposition for micropatterning, Nano Lett., 12 (2012)

4960-4965.

[59] K. Kim, Y. Jung, J. Chun, B. Ye, M. Gu, E. Seo, S. Kim, S. Kim, B. Kim, J. Baik, Surface dipole enhanced instantaneous charge pair generation in triboelectric nanogenerator, Nano Energy, 26 (2016) 360-370.

[60] C. Park, G. Song, S. Cho, J. Chung, Y. Lee, E. Kim, M. Kim, S. Lee, J. Huh, C. Park, Nanogenerators: Supramolecular-Assembled Nanoporous Film with Switchable Metal Salts for a Triboelectric Nanogenerator Adv. Funct. Mater., 27 (2017) 1701367.

[61] S. Wang, Y. Xie, S. Niu, L. Lin, C. Liu, Y. Zhou, Z.L. Wang, Maximum surface charge density for triboelectric nanogenerators achieved by ionized-air injection: methodology and theoretical understanding, Adv. Mater., 26 (2014) 6720-6728.

[62] X. Zhang, M. Han, R. Wang, B. Meng, F. Zhu, X. Sun, W. Hu, W. Wang, Z.H. Li, H. Zhang, High-performance triboelectric nanogenerator with enhanced energy density based on single-step fluorocarbon plasma treatment, Nano Energy, 4 (2014) 123-131.

[63] S. Shin, Y. Kwon, Y. Kim, J. Jung, M. Lee, J. Nah, Triboelectric Charging Sequence Induced by Surface Functionalization as a Method To Fabricate High Performance Triboelectric Generators, ACS Nano, 9 (2015) 4621-4627.

[64] S. Wang, Y. Zi, Y. Zhou, S. Li, F. Fan, L. Lin, Z.L. Wang, Molecular surface functionalization to enhance the power output of triboelectric nanogenerators, J. Mater. Chem. A, 4 (2016) 3728-3734.

[65] C. Wu, T. Kim, J. Park, H. An, J. Shao, X. Chen, Z.L. Wang, Enhanced Triboelectric Nanogenerators Based on MoS_2 Monolayer Nanocomposites Acting as Electron-Acceptor Layers, ACS Nano, 11 (2017) 8356-8363.

[66] R. Wen, J. Guo, A. Yu, K. Zhang, J. Kou, Y. Zhu, Y. Zhang, B. Li, J. Zhai, Remarkably enhanced triboelectric nanogenerator based on flexible and transparent monolayer titania nanocomposite, Nano Energy, 50 (2018) 140-147.

[67] C. Wu, T. Kim, H. Choi, Reduced graphene-oxide acting as electron-trapping sites

in the friction layer for giant triboelectric enhancement, Nano Energy, 32 (2017) 542-550.

[68] C. Yang, C. Ko, S. Chang, M. Huang, Study on fabric-based triboelectric nanogenerator using graphene oxide/porous PDMS as a compound friction layer, Nano Energy, 92 (2022) 106791.

[69] Y. Zhang, Z. Zhou, L. Sun, Z. Liu, X. Xia, T. Tao, "Genetically Engineered" Biofunctional Triboelectric Nanogenerators Using Recombinant Spider Silk, Adv. Mater., 30 (2018) 1805722.

[70] C. Jeong, K. Baek, S. Niu, T. Nam, Y. Hur, D. Park, G. Hwang, M. Byun, Z. Wang, Y. Jung, K. Lee, Topographically-designed triboelectric nanogenerator via block copolymer self-assembly, Nano Lett., 14 (2014) 7031-7038.

[71] K. Lee, J. Chun, J. Lee, K. Kim, N. Kang, J. Kim, M. Kim, K. Shin, M. Gupta, J. Baik, S. Kim, Hydrophobic sponge structure-based triboelectric nanogenerator, Adv. Mater., 26 (2014) 5037-5042.

[72] J. Chun, J. Kim, W. Jung, C. Kang, S. Kim, Z.L. Wang, J. Baik, Mesoporous pores impregnated with Au nanoparticles as effective dielectrics for enhancing triboelectric nanogenerator performance in harsh environments, Energy Environ. Sci., 8 (2015) 3006-3012.

[73] W. Song, B. Gan, T. Jiang, Y. Zhang, A. Yu, H. Yuan, N. Chen, C. Sun, Z.L. Wang, Nanopillar Arrayed Triboelectric Nanogenerator as a Self-Powered Sensitive Sensor for a Sleep Monitoring System, ACS Nano, 10 (2016) 8097-8103.

[74] W. Seung, M. Gupta, K. Lee, K. Shin, J. Lee, T. Kim, S. Kim, J. Lin, J. Kim, S. Kim, Nanopatterned Textile-Based Wearable Triboelectric Nanogenerator, ACS Nano, 9 (2015) 3501-3509.

[75] J. Sun, T. Yang, I. Kuo, J. Wu, C. Wang, L. Chen, A leaf-molded transparent triboelectric nanogenerator for smart multifunctional applications, Nano Energy, 32 (2017) 180-186.

[76] G. Zhu, Z. Lin, Q. Jing, P. Bai, C. Pan, Y. Yang, Y. Zhou, Z.L. Wang, Toward large-

scale energy harvesting by a nanoparticle-enhanced triboelectric nanogenerator, Nano Lett., 13 (2013) 847-853.

[77] S. Park, M. Seol, D. Kim, S. Jeon, Y. Choi, Triboelectric nanogenerator with nanostructured metal surface using water-assisted oxidation, Nano Energy, 21 (2016) 258-264.

[78] S. Chen, T. Huang, H. Zuo, S. Qian, Y. Guo, L. Sun, D. Lei, Q. Wu, B. Zhu, C. He, X. Mo, E. Jeffries, H. Yu, Z. You, A Single Integrated 3D-Printing Process Customizes Elastic and Sustainable Triboelectric Nanogenerators for Wearable Electronics, Adv. Funct. Mater., 28 (2018) 1805108.

[79] J. Huang, X. Fu, G. Liu, S. Xu, X. Li, C. Zhang, L. Jiang, Micro/nano-structures-enhanced triboelectric nanogenerators by femtosecond laser direct writing, Nano Energy, 62 (2019) 638-644.

[80] B. Chen, W. Tang, T. Jiang, L. Zhu, X. Chen, C. He, L. Xu, H. Guo, P. Lin, D. Li, J. Shao, Z.L. Wang, Three-dimensional ultraflexible triboelectric nanogenerator made by 3D printing, Nano Energy, 45 (2018) 380-389.

[81] X. Pu, L. Li, H. Song, C. Du, Z. Zhao, C. Jiang, G. Cao, W. Hu, Z.L. Wang, A self-charging power unit by integration of a textile triboelectric nanogenerator and a flexible lithium-ion battery for wearable electronics, Adv. Mater., 27 (2015) 2472-2478.

[82] X. Pu, L. Li, M. Liu, C. Jiang, C. Du, Z. Zhao, W. Hu, Z.L. Wang, Wearable Self-Charging Power Textile Based on Flexible Yarn Supercapacitors and Fabric Nanogenerators, Adv. Mater., 28 (2016) 98-105.

[83] X. Pu, W. Song, M. Liu, C. Sun, C. Du, C. Jiang, X. Huang, D. Zou, W. Hu, Z.L. Wang, Wearable Power-Textiles by Integrating Fabric Triboelectric Nanogenerators and Fiber-Shaped Dye-Sensitized Solar Cells, Adv. Energy Mater., 6 (2016) 1601048.

[84] Y. Wang, L.X. Zhang, H. Hou, W. Xu, G. Duan, S. He, K. Liu, S. Jiang, Recent progress in carbon-based materials for supercapacitor electrodes: a review, J.

Mater. Sci., 56 (2021) 173-200.

[85] F. Wang, X. Wu, X. Yuan, Z. Liu, Y. Zhang, L. Fu, Y. Zhu, Q. Zhou, Y. Wu, W. Huang, Latest advances in supercapacitors: from new electrode materials to novel device designs, Chem. Soc. Rev., 46 (2017) 6816-6854.

[86] M. Lukatskaya, B. Dunn, Y. Gogotsi, Multidimensional materials and device architectures for future hybrid energy storage, Nat. Commun., 7 (2016) 12647.

[87] Y. Gogotsi, R. Penner, Energy storage in nanomaterials–capacitive, pseudocapacitive, or battery-like?, ACS Nano, 12 (2018) 2081-2083.

[88] J. You, M. Li, B. Ding, X. Wu, C. Li, Crab chitin-based 2D soft nanomaterials for fully biobased electric devices, Adv. Mater., 29 (2017) 1606895.

[89] S. Zhang, M. Wang, Z. Zhou, Y. Tang, Multifunctional Electrode Design Consisting of 3D Porous Separator Modulated with Patterned Anode for High-Performance Dual-Ion Batteries, Adv. Funct. Mater., 27 (2017) 1703035.

[90] M. Salanne, B. Rotenberg, K. Naoi, K. Kaneko, P. Taberna, C. Grey, B. Dunn, P. Simon, Efficient storage mechanisms for building better supercapacitors, Nat. Energy, 1 (2016) 1-10.

[91] Z. Li, L. Zhang, B. Amirkhiz, X. Tan, Z. Xu, H. Wang, B. Olsen, C. Holt, D. Mitlin, Carbonized chicken eggshell membranes with 3D architectures as high-performance electrode materials for supercapacitors, Adv. Energy Mater., 2 (2012) 431-437.

[92] H. Jia, Y. Cai, J. Lin, H. Liang, J. Qi, J. Cao, J. Feng, W. Fei, Heterostructural graphene quantum dot/MnO_2 nanosheets toward high-potential window electrodes for high-performance supercapacitors, Adv. Sci., 5 (2018) 1700887.

[93] P. Yang, Y. Ding, Z. Lin, Z. Chen, Y. Li, P. Qiang, M. Ebrahimi, W. Mai, C. Wong, Z.L. Wang, Low-cost high-performance solid-state asymmetric supercapacitors based on MnO_2 nanowires and Fe_2O_3 nanotubes, Nano Lett., 14 (2014) 731-736.

[94] Y. Xu, J. Wei, L. Tan, J. Yu, Y.W. Chen, A Facile approach to $NiCoO_2$ intimately standing on nitrogen doped graphene sheets by one-step hydrothermal synthesis

for supercapacitors, J. Mater. Chem. A, 3 (2015) 7121-7131.

[95] L. Wang, Z. Dong, Z. Wang, F. Zhang, J. Jin, Layered α-$Co(OH)_2$ nanocones as electrode materials for pseudocapacitors: understanding the effect of interlayer space on electrochemical activity, Adv. Funct. Mater., 23 (2013) 2758-2764.

[96] J. Huang, Y. Xiong, Z. Peng, L. Chen, L. Wang, Y. Xu, L. Tan, K. Yuan, Y. Chen, A General Electrodeposition Strategy for Fabricating Ultrathin Nickel Cobalt Phosphate Nanosheets with Ultrahigh Capacity and Rate Performance, ACS Nano, 14 (2020) 14201-14211.

[97] S. Zhang, N. Pan, Supercapacitors Performance Evaluation, Adv. Energy Mater., 5 (2015) 1401401.

[98] Q. Gou, S. Zhao, J. Wang, M. Li, J. Xue, Recent Advances on Boosting the Cell Voltage of Aqueous Supercapacitors, Nano-Micro Lett., 12 (2020) 98.

[99] J. Yin, W. Zhang, N. Alhebshi, N. Salah, H. Alshareef, Synthesis Strategies of Porous Carbon for Supercapacitor Applications, Small Methods, 4 (2020) 1900853.

[100] R. Zeng, X. Tang, B. Huang, K. Yuan, Y. Chen, Nitrogen-Doped Hierarchically Porous Carbon Materials with Enhanced Performance for Supercapacitor, Chemelectrochem, 5 (2018) 515-522.

[101] H. Fei, W. Li, A. Bhardwaj, S. Nuguri, A. Ribbe, J. Watkins, Ordered Nanoporous Carbons with Broadly Tunable Pore Size Using Bottlebrush Block Copolymer Templates, J. Am. Chem. Soc., 141 (2019) 17006-17014.

[102] D. Kong, W. Ren, C. Cheng, Y. Wang, Z. Huang, H. Yang, Three-Dimensional $NiCo_2O_4$@Polypyrrole Coaxial Nanowire Arrays on Carbon Textiles for High-Performance Flexible Asymmetric Solid-State Supercapacitor, ACS Appl. Mater. Interfaces, 7 (2015) 21334-21346.

[103] T. Ling, P. Da, X. Zheng, B. Ge, Z. Hu, M. Wu, X. Du, W. Hu, M. Jaroniec, S. Qiao, Atomic-level structure engineering of metal oxides for high-rate oxygen intercalation pseudocapacitance, Sci. Adv., 4 (2018) 6261-6268.

[104] J. Luo, W. Tang, F. Fan, C. Liu, Y. Pang, G. Cao, Z.L. Wang, Transparent and Flexible Self-Charging Power Film and Its Application in a Sliding Unlock System in Touchpad Technology, ACS Nano, 10 (2016) 8078-8086.

[105] F. Yi, J. Wang, X. Wang, S. Niu, S. Li, Q. Liao, Y. Xu, Z. You, Y. Zhang, Z.L. Wang, Stretchable and Waterproof Self-Charging Power System for Harvesting Energy from Diverse Deformation and Powering Wearable Electronics, ACS Nano, 10 (2016) 6519-6525.

[106] L. Shi, S. Dong, P. Ding, J. Chen, S. Liu, S. Huang, H. Xu, U. Farooq, S. Zhang, S. Li, J. Luo, Carbon electrodes enable flat surface PDMS and PA6 triboelectric nanogenerators to achieve significantly enhanced triboelectric performance, Nano Energy, 55 (2019) 548-557.

[107] X. He, Y. Zi, H. Guo, H. Zheng, Y. Xi, C. Wu, J. Wang, W. Zhang, C. Lu, Z.L. Wang, A Highly Stretchable Fiber-Based Triboelectric Nanogenerator for Self-Powered Wearable Electronics, Adv. Funct. Mater., 27 (2017) 1604378.

[108] X. Du, Y. Liu, J. Wang, H. Niu, Z. Yuan, S. Zhao, X. Zhang, R. Cao, Y. Yin, N. Li, C. Zhang, Y. Xing, W. Xu, C. Li, Improved Triboelectric Nanogenerator Output Performance through Polymer Nanocomposites Filled with Core-shell-Structured Particles, ACS Appl. Mater. Interfacs, 10 (2018) 25683-25688.

[109] H. Li, L. Su, S. Kuang, C. Pan, G. Zhu, Z.L. Wang, Significant Enhancement of Triboelectric Charge Density by Fluorinated Surface Modification in Nanoscale for Converting Mechanical Energy, Adv. Funct. Mater., 25 (2015) 5691-5697.

[110] X. Chen, A. Yusuf, J. del Rio, D. Wang, A facile and robust route to polyvinyl alcohol-based triboelectric nanogenerator containing flame-retardant polyelectrolyte with improved output performance and fire safety, Nano Energy, 81 (2021) 105656.

[111] N. Cui, L. Gu, Y. Lei, J. Liu, Y. Qin, X. Ma, Y. Hao, Z.L. Wang, Dynamic Behavior of the Triboelectric Charges and Structural Optimization of the Friction Layer for a Triboelectric Nanogenerator, ACS Nano, 10 (2016) 6131-6138.

[112] X. Chen, X. Pu, T. Jiang, A. Yu, L. Xu, Z.L. Wang, Tunable Optical Modulator by Coupling a Triboelectric Nanogenerator and a Dielectric Elastomer, Adv. Funct. Mater., 27 (2017) 1603788.

[113] Y. Feng, Y. Zheng, S. Ma, D. Wang, F. Zhou, W. Liu, High output polypropylene nanowire array triboelectric nanogenerator through surface structural control and chemical modification, Nano Energy, 19 (2016) 48-57.

[114] D. Kim, S. Park, S. Jeon, M. Seol, Y. Choi, A Triboelectric Sponge Fabricated from a Cube Sugar Template by 3D Soft Lithography for Superhydrophobicity and Elasticity, Adv. Electron. Mater., 2 (2016) 1500331.

[115] M. Zhu, Y. Wang, M. Lou, J. Yu, Z. Li, B. Ding, Bioinspired transparent and antibacterial electronic skin for sensitive tactile sensing, Nano Energy, 81 (2021) 105669.

[116] M. Zhu, M. Lou, J. Yu, Z. Li, B. Ding, Energy autonomous hybrid electronic skin with multi-modal sensing capabilities, Nano Energy, 78 (2020) 105208.

[117] Y. Yin, H. Li, J. Xu, C. Zhang, F. Liang, X. Li, Y. Jiang, J. Cao, H. Feng, J. Mao, L. Qin, Y. Kang, G. Zhu, Facile Fabrication of Flexible Pressure Sensor with Programmable Lattice Structure, ACS Appl. Mater. Interfaces, 13 (2021) 10388-10396.

[118] H. Qiao, Y. Zhang, Z. Huang, Y. Wang, D. Li, H. Zhou, 3D printing individualized triboelectric nanogenerator with macro-pattern, Nano Energy, 50 (2018) 126-132.

[119] T. Wallin, J. Pikul, R. Shepherd, 3D printing of soft robotic systems, Nat. Rev. Mater., 3 (2018) 84-100.

[120] J. Xue, L. Gao, X. Hu, K. Cao, W. Zhou, W. Wang, Y. Lu, Stereolithographic 3D Printing-Based Hierarchically Cellular Lattices for High-Performance Quasi-Solid Supercapacitor, Nano-Micro Lett., 11 (2019) 46.

[121] Y. Yin, Y. Wang, H. Li, J. Xu, C. Zhang, X. Li, J. Cao, H. Feng, G. Zhu, A flexible dual parameter sensor with hierarchical porous structure for fully decoupled pressure–temperature sensing, Chem. Eng. J., 430 (2022) 133158.

[122] X. Ji, J. Wang, L. Mei, W. Tao, A. Barrett, Z. Su, S. Wang, G. Ma, J. Shi, S. Zhang, Porphyrin/SiO_2/Cp*Rh (bpy)Cl Hybrid nanoparticles mimicking chloroplast with enhanced electronic energy transfer for biocatalyzed artificial photosynthesis, Adv. Funct. Mater., 28 (2018) 1705083.

[123] P. Aminayi, N. Abidi, Ultra-oleophobic cotton fabric prepared using molecular and nanoparticle vapor deposition methods, Surf. Coat. Technol., 276 (2015) 636-644.

[124] L. Zhang, C. Su, L. Cheng, N. Cui, L. Gu, Y. Qin, R. Yang, F. Zhou, Enhancing the Performance of Textile Triboelectric Nanogenerators with Oblique Microrod Arrays for Wearable Energy Harvesting, ACS Appl. Mater. Interfaces, 11 (2019) 26824-26829.

[125] Y. Shao, C. Feng, B. Deng, B. Yin, M.B. Yang, Facile method to enhance output performance of bacterial cellulose nanofiber based triboelectric nanogenerator by controlling micro-nano structure and dielectric constant, Nano Energy, 62 (2019) 620-627.

[126] H. Li, R. Li, X. Fang, H. Jiang, X. Ding, B. Tang, G. Zhou, R. Zhou, Y. Tang, 3D printed flexible triboelectric nanogenerator with viscoelastic inks for mechanical energy harvesting, Nano Energy, 58 (2019) 447-454.

[127] Z. Peng, J. Song, Y. Gao, J. Liu, C. Lee, G. Chen, Z. Wang, J. Chen, M. Leung, A fluorinated polymer sponge with superhydrophobicity for high-performance biomechanical energy harvesting, Nano Energy, 85 (2021) 106021.

[128] H. Yoon, D. Kim, W. Seung, U. Khan, T. Kim, T. Kim, S. Kim, 3D-printed biomimetic-villus structure with maximized surface area for triboelectric nanogenerator and dust filter, Nano Energy, 63 (2019) 103857.

[129] S. He, Z. Yu, H. Zhou, Z. Huang, Y. Zhang, Y. Li, J. Li, Y. Wang, D. Li, Polymer tubes as carrier boats of thermosetting and powder materials based on 3D printing for triboelectric nanogenerator with microstructure, Nano Energy, 52 (2018) 134-141.

[130] Q. Jin, L. Ma, W. Zhou, R. Chintalapalle, Y. Shen, X. Li, Strong interaction between Au nanoparticles and porous polyurethane sponge enables efficient environmental catalysis with high reusability, Catal. Today, 358 (2020) 246-253.

[131] Q. Jin, Y. Shen, Y. Cai, L. Chu, Y. Zeng, Resource utilization of waste V_2O_5-based deNO_x catalysts for hydrogen production from formaldehyde and water via steam reforming, J. Hazard. Mater., 381 (2020) 120934.

[132] Y. Li, C. Xu, P. Hu, L. Zhen, Carrier control of MoS_2 nanoflakes by functional self-assembled monolayers, ACS Nano, 7 (2013) 7795-804.

[133] W. Chen, S. Lai, C. Yen, X. Jiang, D. Peroulis, L. Stanciu, Surface functionalization of $Ti_3C_2T_x$ MXene with highly reliable superhydrophobic protection for volatile organic compounds sensing, ACS Nano, 14 (2020) 11490-11501.

[134] V. Marconi, R. Kradin, F. Marty, D. Hospenthal, C. Kotton, Disseminated dermatophytosis in a patient with hereditary hemochromatosis and hepatic cirrhosis: case report and review of the literature, Med. Mycol., 48 (2010) 518-527.

[135] G. Wang, H. Feng, L. Hu, W. Jin, Q. Hao, A. Gao, X. Peng, W. Li, K. Wong, H. Wang, Z. Li, P. Chu, An antibacterial platform based on capacitive carbon-doped TiO_2 nanotubes after direct or alternating current charging, Nat. Commun., 9 (2018) 2055.

[136] C. Liu, X. Xie, W. Zhao, J. Yao, D. Kong, A. Boehm, Y. Cui, Static electricity powered copper oxide nanowire microbicidal electroporation for water disinfection, Nano Lett., 14 (2014) 5603-5608.

[137] Z. Zhang, R. Dua, L. Zhang, H. Zhu, H. Zhang, P. Wang, Carbon-layer-protected cuprous oxide nanowire arrays for efficient water reduction, ACS Nano, 7 (2013) 1709-1717.

[138] S. Wang, W. Wang, L. Yue, S. Cui, H. Wang, C. Wang, S. Chen, Hierarchical Cu_2O nanowires covered by silver nanoparticles-doped carbon layer supported on

Cu foam for rapid and efficient water disinfection with lower voltage, Chem. Eng. J., 382 (2020) 122855.

[139] J. Tian, H. Feng, L. Yan, M. Yu, H. Ouyang, H. Li, W. Jiang, Y. Jin, G. Zhu, Z. Li, A self-powered sterilization system with both instant and sustainable anti-bacterial ability, Nano Energy, 36 (2017) 241-249.

[140] J. Jeong, J.Y. Kim, M. Cho, W. Choi, J. Yoon, Inactivation of Escherichia coli in the electrochemical disinfection process using a Pt anode, Chemosphere, 67 (2007) 652-659.

[141] J. Zhou, T. Wang, X. Xie, Rationally designed tubular coaxial-electrode copper ionization cells (CECICs) harnessing non-uniform electric field for efficient water disinfection, Environ. Int., 128 (2019) 30-36.

[142] T. Wang, H. Chen, C. Yu, X. Xie, Rapid determination of the electroporation threshold for bacteria inactivation using a lab-on-a-chip platform, Environ. Int., 132 (2019) 105040.

[143] B. Dunn, H. Kamath, J.M. Tarascon, Electrical energy storage for the grid: a battery of choices, Science, 334 (2011) 928-935.

[144] O. Schmidt, A. Hawkes, A. Gambhir, I. Staffell, The future cost of electrical energy storage based on experience rates, Nat. Energy, 2 (2017) 17110.

[145] S. Chu, A. Majumdar, Opportunities and challenges for a sustainable energy future, Nature, 488 (2012) 294-303.

[146] X. Huang, Z. Zeng, H. Zhang, Metal dichalcogenide nanosheets: preparation, properties and applications, Chem. Soc. Rev., 42 (2013) 1934-1946.

[147] Y. Liu, K. He, G. Chen, W. Leow, X. Chen, Nature-Inspired Structural Materials for Flexible Electronic Devices, Chem. Rev., 117 (2017) 12893-12941.

[148] D. Dubal, O. Ayyad, V. Ruiz, P. Gómez-Romero, Hybrid energy storage: the merging of battery and supercapacitor chemistries, Chem. Soc. Rev., 44 (2015) 1777-1790.

[149] S. Kim, S. Kim, K. Jung, J. Kim, J. Jang, Ideal nanoporous gold based

supercapacitors with theoretical capacitance and high energy/power density, Nano Energy, 24 (2016) 17-24.

[150] S. Fleischmann, J. Mitchell, R. Wang, C. Zhan, D. Jiang, V. Presser, V. Augustyn, Pseudocapacitance: From Fundamental Understanding to High Power Energy Storage Materials, Chem. Rev., 120 (2020) 6738-6782.

[151] J. Miller, P. Simon, Materials science. Electrochemical capacitors for energy management, Science, 321 (2008) 651-652.

[152] Z. Wu, L. Jiang, W. Tian, Y. Wang, Y. Jiang, Q. Gu, L. Hu, Novel Sub-5 nm Layered Niobium Phosphate Nanosheets for High-Voltage, Cation-Intercalation Typed Electrochemical Energy Storage in Wearable Pseudocapacitors, Adv. Energy Mater., 9 (2019) 1900111.

[153] J. Huang, J. Wei, Y. Xiao, Y. Xu, Y. Xiao, Y. Wang, L. Tan, K. Yuan, Y. Chen, When Al-Doped Cobalt Sulfide Nanosheets Meet Nickel Nanotube Arrays: A Highly Efficient and Stable Cathode for Asymmetric Supercapacitors, ACS Nano, 12 (2018) 3030-3041.

[154] I. Hussain, T. Hussain, S. Ahmed, T. Kaewmaraya, M. Ahmad, X. Chen, M. Javed, C. Lamiel, K. Zhang, Binder-free trimetallic phosphate nanosheets as an electrode: Theoretical and experimental investigation, J. Power Sources, 513 (2021) 230556.

[155] Z. Fang, L. Peng, Y. Qian, X. Zhang, Y. Xie, J. Cha, G. Yu, Dual tuning of Ni-Co-A (A=P, Se, O) nanosheets by anion substitution and holey engineering for efficient hydrogen evolution, J. Am. Chem. Soc., 140 (2018) 5241-5247.

[156] L. Song, T. Zheng, L. Zheng, B. Lu, H. Chen, Q. He, W. Zheng, Y. Hou, J. Lian, Y. Wu, Cobalt-doped basic iron phosphate as bifunctional electrocatalyst for long-life and high-power-density rechargeable zinc-air batteries, Appl. Catal. B: Environ., 300 (2022) 120712.

[157] C. Cui, X. Lai, R. Guo, E. Ren, W. Qin, L. Liu, M. Zhou, H. Xiao, Waste paper-based carbon aerogel supported ZIF-67 derived hollow NiCo phosphate nanocages for electrocatalytic oxygen evolution reaction, Electrochim. Acta, 393 (2021)

139076.

[158] X. Li, A. Elshahawy, C. Guan, J. Wang, Metal Phosphides and Phosphates-based Electrodes for Electrochemical Supercapacitors, Small, 13 (2017) 1701530.

[159] L. Tao, J. Li, Q. Zhou, H. Zhu, G. Hu, J. Huang, Composition, microstructure and performance of cobalt nickel phosphate as advanced battery-type capacitive material, J. Alloy. Compd., 767 (2018) 789-796.

[160] B. Li, P. Gu, Y. Feng, G. Zhang, K. Huang, H. Xue, H. Pang, Ultrathin nickel-cobalt phosphate 2D nanosheets for electrochemical energy storage under aqueous/solid-state electrolyte, Adv. Funct. Mater., 27 (2017) 1605784.

[161] S. Marje, S. Pujari, S. Khalate, V. Patil, V. Parale, T. Kim, H. Park, J. Gunjakar, C. Lokhande, U. Patil, Intercalation-type pseudocapacitive clustered nanoparticles of nickel-cobalt phosphate thin films synthesized via electrodeposition as cathode for high-performance hybrid supercapacitor devices, J. Mater. Chem. A, 10 (2022) 11225-11237.

[162] M. Li, Y. Luo, C. Jia, Q. Zhang, G. Luo, L. Zhao, R. Boukherroub, Z. Jiang, Facile Synthesis of Bimetal Nickel Cobalt Phosphate Nanostructures for High-Performance Hybrid Supercapacitors, J. Alloy. Compd., 893 (2022) 162340.

[163] B. Vamsi Krishna, S. Khaja Hussain, J. Yu, Three-dimensional flower-like nickel doped cobalt phosphate hydrate microarchitectures for asymmetric supercapacitors, J. Colloid Interface Sci., 592 (2021) 145-155.

[164] S. Marje, V. Patil, V. Parale, H. Park, P. Shinde, J. Gunjakar, C. Lokhande, U. Patil, Microsheets like nickel cobalt phosphate thin films as cathode for hybrid asymmetric solid-state supercapacitor: Influence of nickel and cobalt ratio variation, Chem. Eng. J., 429 (2022) 132184.

[165] A. Numan, F. Bibi, F. Omar, S. Ullah, O. Al-Hartomy, M. Khalid, Harvesting enhanced electrochemical performance of mixed structured nickel cobalt phosphate for energy storage application, J. Alloy. Compd., 927 (2022) 167031.

[166] M. Iqbal, J. Khan, A. Afzal, S. Aftab, Exploring the synergetic electrochemical

performance of cobalt sulfide/cobalt phosphate composites for supercapattery devices with high-energy and rate capability, Electrochim. Acta, 384 (2021) 138358.

[167] Y. Tang, Y. Zhang, J. Deng, J. Wei, H. Tam, B. Chandran, Z. Dong, Z. Chen, X. Chen, Mechanical Force-Driven Growth of Elongated Bending TiO_2-based Nanotubular Materials for Ultrafast Rechargeable Lithium Ion Batteries, Adv. Mater., 26 (2014) 6111-6118.

[168] Z. Lv, Y. Luo, Y. Tang, J. Wei, Z. Zhu, X. Zhou, W. Li, Y. Zeng, W. Zhang, Y. Zhang, D. Qi, S. Pan, X. Loh, X. Chen, Editable Supercapacitors with Customizable Stretchability Based on Mechanically Strengthened Ultralong MnO_2 Nanowire Composite, Adv. Mater., 30 (2018) 1704531.

[169] X. Rui, Y. Tang, O. Malyi, A. Gusak, Y. Zhang, Z. Niu, H. Tan, C. Persson, X. Chen, Z. Chen, Q. Yan, Ambient dissolution-recrystallization towards large-scale preparation of V_2O_5 nanobelts for high-energy battery applications, Nano Energy, 22 (2016) 583-593.

[170] Y. Li, P. Xu, G. Chen, J. Mou, S. Xue, K. Li, F. Zheng, Q. Dong, J. Hu, C. Yang, M. Liu, Enhancing Li-S redox kinetics by fabrication of a three dimensional Co/CoP@nitrogen-doped carbon electrocatalyst, Chem. Eng. J., 380 (2020) 122595.

[171] S. Navale, V. Mali, S. Pawar, R. Mane, Naushad, F. Stadler, V. Patil, Electrochemical supercapacitor development based on electrodeposited nickel oxide film, RSC Adv., 5 (2015) 51961-51965.

[172] H. Wen, M. Cao, G. Sun, W. Xu, D. Wang, X. Zhang, C. Hu, Hierarchical Three-Dimensional Cobalt Phosphate Microarchitectures: Large-Scale Solvothermal Synthesis, Characterization, and Magnetic and Microwave Absorption Properties, J. Phys. Chem. C, 112 (2008) 15948-15955.

[173] Q. Li, Y. Li, H. Peng, X. Cui, M. Zhou, K. Feng, P. Xiao, Layered $NH_4Co_xNi_{1-x}PO_4.H_2O$ ($0 < x < 1$) nanostructures finely tuned by Co/Ni molar ratios for

asymmetric supercapacitor electrodes, J. Mater. Sci., 51 (2016) 9946-9957.

[174] D. Breitinger, H. Belz, L. Hajba, V. Komlósi, J. Mink, G. Brehm, D. Colognesi, S. Parker, R. Schwab, Combined vibrational spectra of natural wardite, J. Mol. Struct., 706 (2004) 95-99.

[175] N. Padmanathan, H. Shao, K. Razeeb, Multifunctional Nickel Phosphate Nano/Microflakes 3D Electrode for Electrochemical Energy Storage, Nonenzymatic Glucose, and Sweat pH Sensors, ACS Appl. Mater. Interfaces, 10 (2018) 8599-8610.

[176] T. Munawar, M. Rehman, M. Nadeem, F. Mukhtar, S. Manzoor, M. Ashiq, F. Iqbal, Facile synthesis of Cr-Co co-doped CdO nanowires for photocatalytic, antimicrobial, and supercapacitor applications, J. Alloy. Compd., 885 (2021) 160885.

[177] H. Feng, S. Gao, J. Shi, L. Zhang, Z. Peng, S. Cao, Construction of 3D hierarchical porous $NiCo_2O_4$/graphene hydrogel/Ni foam electrode for high-performance supercapacitor, Electrochim. Acta, 299 (2019) 116-124.

[178] H. Shao, N. Padmanathan, D. McNulty, O. Razeeb, Supercapattery Based on Binder-Free $Co_3(PO_4)_2.8H_2O$ Multilayer Nano/Microflakes on Nickel Foam, ACS Appl. Mater. Interfaces, 8 (2016) 28592-28598.

[179] C. Yuan, Y. Jiang, Z. Wang, X. Xie, Z. Yang, A. Bin Yousaf, A. Xu, Cobalt phosphate nanoparticles decorated with nitrogen-doped carbon layers as highly active and stable electrocatalysts for the oxygen evolution reaction, J. Mater. Chem. A, 4 (2016) 8155-8160.

[180] T. Yan, H. Feng, X. Ma, L. Han, L. Zhang, S. Cao, Regulating the electrochemical behaviours of a hierarchically structured $Co_3(PO_4)_2$/Ni-Co-O for a high-performance all-solid-state supercapacitor, Dalt. Trans., 49 (2020) 10621-10630.

[181] Y. Zhu, Z. Wu, M. Jing, H. Hou, Y. Yang, Y. Zhang, X. Yang, W. Song, X. Jia, X. Ji, Porous $NiCo_2O_4$ spheres tuned through carbon quantum dots utilised as advanced materials for an asymmetric supercapacitor, J. Mater. Chem. A, 3 (2015)

866-877.

[182] C. Choi, D. Ashby, D. Butts, R. DeBlock, Q. Wei, J. Lau, B. Dunn, Achieving high energy density and high power density with pseudocapacitive materials, Nat. Rev. Mater., 5 (2020) 5-19.

[183] K. Sankar, Y. Seo, S. Lee, S. Jun, Redox Additive-Improved Electrochemically and Structurally Robust Binder-Free Nickel Pyrophosphate Nanorods as Superior Cathode for Hybrid Supercapacitors, ACS Appl. Mater. Interfaces, 10 (2018) 8045-8056.

[184] Y. Tang, Z. Liu, W. Guo, T. Chen, Y. Qiao, S. Mu, Y. Zhao, F. Gao, Honeycomb-like mesoporous cobalt nickel phosphate nanospheres as novel materials for high performance supercapacitor, Electrochim. Acta, 190 (2016) 118-125.

[185] M. Liu, N. Shang, X. Zhang, S. Gao, C. Wang, Z. Wang, Microwave synthesis of sodium nickel-cobalt phosphates as high-performance electrode materials for supercapacitors, J. Alloy. Compd., 791 (2019) 929-935.

[186] B. Liang, Y. Chen, J. He, C. Chen, W. Liu, Y. He, X. Liu, N. Zhang, V. Roy, Controllable Fabrication and Tuned Electrochemical Performance of Potassium Co-Ni Phosphate Microplates as Electrodes in Supercapacitors, ACS Appl. Mater. Interfaces, 10 (2018) 3506-3514.

[187] L. Tao, J. Li, Q. Zhou, H. Zhu, G. Hu, J. Huang, Composition, microstructure and performance of cobalt nickel phosphate as advanced battery-type capacitive material, J. Alloy. Compd., 767 (2018) 789-796.

[188] B. Li, P. Gu, Y. Feng, G. Zhang, K. Huang, H. Xue, H. Pang, Ultrathin Nickel-Cobalt Phosphate 2D Nanosheets for Electrochemical Energy Storage under Aqueous/Solid-State Electrolyte, Adv. Funct. Mater., 27 (2017) 1605784.

[189] M. Liu, J. Li, Y. Hu, Q. Yang, L. Kang, Design and Fabrication of $Ni_3P_2O_8$-$Co_3P_2O_8 \cdot 8H_2O$ as Advanced Positive Electrodes for Asymmetric Supercapacitors, Electrochim. Acta, (2016) 142-150.

[190] A. Ma, B. Mzi, B. Sa, A. Na, C. Ama, D. Sa, Binary composites of nickel-

manganese phosphates for supercapattery devices, J. Energy Storage, 33 (2020) 102020.

[191] S. Prabhu, C. Balaji, M. Navaneethan, M. Selvaraj, N. Anandhan, D. Sivaganesh, S. Saravanakumar, P. Sivakumar, R. Ramesh, Investigation on mesoporous bimetallic tungstate nanostructure for high-performance solid- state supercapattery, J. Alloy. Compd., 875 (2021) 160066-160076.

[192] B. Senthilkumar, A. Irshad, P. Barpanda, Cobalt and Nickel Phosphates as Multifunctional Air-Cathodes for Rechargeable Hybrid Sodium-Air Battery Applications, ACS Appl. Mater. Interfaces, 11 (2019) 33811-33818.

[193] L. Xu, Y. Xi, W. Li, Z. Hua, J. Peng, J. Hu, J. Zhou, P. Zhang, J. Wang, W. Wang, 3D frame-like architecture of NC-incorporated mixed metal phosphide boosting ultrahigh energy density pouch-type supercapacitors, Nano Energy, 91 (2022) 106630.

[194] J. Chen, K. Sheng, P. Luo, C. Li, G. Shi, Graphene hydrogels deposited in nickel foams for high-rate electrochemical capacitors, Adv. Mater., 24 (2012) 4569-4573.

[195] H. Wang, J. Robinson, X. Li, H. Dai, Solvothermal reduction of chemically exfoliated graphene sheets, J. Am. Chem. Soc., 131 (2009) 9910-9911.

[196] L. Zhang, G. Shi, Preparation of highly conductive graphene hydrogels for fabricating supercapacitors with high rate capability, J. Phys. Chem. C, 115 (2011) 17206-17212.

[197] W. Liu, N. Liu, Y. Yue, J. Rao, F. Cheng, J. Su, Z. Liu, Y. Gao, Piezoresistive pressure sensor based on synergistical innerconnect polyvinyl alcohol nanowires/wrinkled graphene film, Small, 14 (2018) 1704149.